

IN-12856 p-139

C/S ~~4569016~~

4630032

FINAL REPORT
for
NASA Grant Number NAG 3-206
IMPROVEMENT OF ION THRUSTER DESIGN
by
Raymon T. Carpenter
Principle Investigator



(NASA-CR-177223) IMPROVEMENT OF ION
THRUSTER DESIGN Final Report (Iowa Univ.)
139 p HC A07/MF A01 CSCL 21C

N86-27419

Unclas

G3/20 43309

Department of Physics and Astronomy
THE UNIVERSITY OF IOWA

Iowa City, Iowa 52242

FINAL REPORT
for
NASA Grant Number NAG 3-206
IMPROVEMENT OF ION THRUSTER DESIGN
by
Raymon T. Carpenter
Principle Investigator

INTRODUCTION

This report covers work done at the University of Iowa under NASA grant NAG3-206, starting in September, 1981 and continuing until September, 1984. During this time extensive measurements have been made on two physically different ion thrusters. One was supplied by NASA Lewis and is the 17 cm. ion thruster described by Sovey (Sovey, 1981). This thruster was configured with 1"x1"x0.42" SmCo magnets in a line cusp configuration. The second thruster was constructed at the University of Iowa and is identical in inside dimensions to the first. It differs in that the iron walls are somewhat thicker and the conical end section is bolted onto the main chamber rather than being welded so that it could be easily exchanged with a flat end section, such as is used in the ring-cusp configuration. It is equipped with 1"x1"x0.25" SmCo magnets and has been used in both ring cusp and line cusp arrangements. The same hollow cathode was used with both thrusters. Early measurements were performed with the NASA thruster but after establishing that the Iowa thruster had essentially identical plasma properties and equal or slightly superior performance parameters, all later work was done on the new device.

It is assumed that the reader is familiar with the general nature of the ion sources developed at NASA Lewis and no general discussion of these devices will be given. The papers by Sovey (Sovey, 1981; Sovey, 1982) and references therein are an excellent

introduction to this material. Fig. I.1 is taken from Sovey's 1981 reference and shows the essential features of both thrusters used in the work reported here. The hollow cathode assembly originally used in this thruster was slightly altered and is shown in the configuration used in the present work in Fig. I.2. Also it was found that the new magnets used in the Iowa thruster line cusp configuration were more difficult to handle. For this reason, and also to improve the magnet cooling, the magnet rows were encased in brass channels as shown in Fig. I.3. The iron pole-faces were added because previous work at NASA-Lewis had shown a marginal improvement in performance with such an arrangement (Sovey, 1981).

Measurements of two types were performed. Langmuir probes were used to measure plasma potential, electron density and electron temperature in all regions inside the thruster. These data were obtained for several sets of discharge voltages and currents. Investigations of the ring cusp configurations were considerably more extensive than for the line cusp case. This is essentially because our procedures improved markedly during the course of the grant period and the ring cusp measurements followed those on the line cusp configuration. Also both ion and electron currents have been measured to all parts of the walls and to all parts of the cathode assembly using collecting plates of various types. These measurements have also been made for various parameter sets.

The experimental conditions under which the data to be described were taken differ in two respects from those at NASA-Lewis. First, no current regulator was available for the main power supply. Therefore the discharge was stabilized by inserting a one-ohm resistance in series with the power supply. For the runs where plasma parameters inside the thruster were determined as a function of position, the discharge current was kept constant so the series resistance had no effect. However, for runs where data were taken with fixed probes over a wide range of operating parameters, the usual method of operation was to set the power-supply voltage and then vary the discharge current by varying the gas flow in the hollow cathode. The result of course was that the discharge voltage, discharge current and flow rate all varied from point to point, a situation that is not particularly unwanted but which may make comparison with data taken under different circumstances difficult. The second difference is possibly more significant. The vacuum system available was significantly limited compared to those used at NASA-Lewis. Two systems were used. Early data were taken with a system pumped with a 6 inch diffusion pump with an overall pumping speed of about 1000 liters per second. Later data were taken using a system pumped by a 10 inch pump and an overall speed of about 4000 liters per second. The result was that at the higher gas flow rates there was undoubtedly a reflux of gas into the thruster chamber at rates that were difficult to estimate. Operationally this is equivalent in every way to introduction of gas

into the chamber through an inlet separate from the hollow cathode, as was customarily done at Lewis, so there was no difference in the physical situation. However, control of the situation was not possible.

In the following we first discuss some generalities about the data-taking methods used. All of the data are then summarized and discussed as it is presented in section 2. The organization is approximately chronological. Finally, a discussion is given in section 3 of the operation of the thruster based on calculations of ion orbits in the electric and magnetic fields that exist in the thruster. Other analytic considerations and results are discussed in this section also. A short final survey is given at the end.

Much of what will be presented here is contained in the Master's thesis of Mr. Scott Boardsen (Boardsen, 1984) which is appended to this report in a slightly abbreviated form, to facilitate reference to this work. The abridgment consists of the elimination of non-essential introductory comments. Many details concerning this work are covered there and will not be repeated in this report. There is, however, considerable overlap between the two papers so the present report is essentially self-contained.

Section 1

EXPERIMENTAL METHODS

1.1 Langmuir Probe Measurements

The plasmas encountered in the ion thrusters are dense and hot. There is considerable density variation inside the thruster but typical values range from on the order of $10^{13}/\text{cm}^3$ near the hollow cathode exit aperture to a tenth or less of this near the walls. This influences greatly the types and sizes of probes that can be put into these devices and also the manner in which they can be employed. Tungsten wires with diameters of .25 mm or .38 mm were used in most cases with about 2 mm of length exposed to the plasma. Even with such small areas extreme care was required to prevent melting when probing the densest regions. A computer was used to rapidly sweep the probe bias and digitally record the resulting current. The time during which significant electron current was drawn was kept less than .01 seconds followed by a cooling period during which the probe was kept at a negative bias. The computer (an S-100 bus system) and ADC/DAC (Cromemco D+7A-I/O) was capable of sweeping a 50 volt range with 5 points/volt in .03 seconds. The Langmuir characteristics were analyzed in the usual way (Chen, 1965) after completion of the experiment. Even with these precautions it was difficult to obtain data within one cm of the hollow cathode exit aperture without probe damage. In fact, exactly on axis the closest possible approach was approximately 6 cm. In these regions

the electron current had to be kept well below the saturation point and therefore only the temperature was measured. Two general classes of probe measurements were made. First, in some of the earlier work a set of fixed probes was used. For these cases, the plasma parameters were obtained for several sets of thruster operating conditions and the object generally was to determine how the plasma parameters, most importantly the plasma density, were related to the beam current and to the discharge voltage and current. In the second class of measurements a movable probe was used and the object was to determine how the plasma parameters varied throughout the interior of the thruster chamber for various fixed thruster operating conditions. These measurements were much more time consuming and it was usually possible to acquire data for only a single set of thruster operating conditions in a day. The probes were insulated, except for the tips, by alumina ceramic tubing. The main axial shaft passed through a sliding vacuum seal which permitted axial motion (variations in z) and rotation (variations in θ). In turn the seal was on a sliding plate which permitted variations in r . The probe shaft entered the thruster through a slit in the end plate, which was a 120 wires per inch screen grid for some of the runs and a solid sheet for others. For some of the runs the data were digitized and stored in a computer for off-line analysis while in others probe saturation current (proportional to plasma density) was read from an oscilloscope display of the probe characteristic using a transistor curve tracer.

1.2 Loss measurements

In principle the measurement of the flux of electrons or of ions to a given surface involves only the measurement of the current to an insulated plate placed on the surface and biased at the original surface potential. In practice both electrons and ions flow to all surfaces and it is necessary to separate the contributions from each species. This can be done by obtaining an I-V characteristic of the plate. The usual situation is that the original surface is negative relative to the plasma. This is because the anode is usually the most positive conducting surface in the plasma and, in a surface confinement discharge plasma, the plasma is positive relative to the anode by a few electron temperatures. If the surface were positive, the current to it would be completely dominated by electrons and the ion current, because of the low ion temperature and the large ion mass, would be completely negligible. In this case the actual current measured to the plate when it is biased at the wall potential is the desired electron current. The loss plate characteristic, needed when the wall is negative with respect to the plasma, is identical in form to a usual Langmuir characteristic. The contribution from the ions is a straight line region when the plate bias is negative enough to repel all electrons in the plasma. When extrapolated to the wall potential this gives the ion current and any residual is the electron current. Note that in the case of ion losses to the

cathode, this procedure is unnecessary since the cathode is the most negative surface in the chamber. Nevertheless, a few characteristics were taken in this case also to check on any unforeseen source of high energy electrons.

Several different sorts of probes were used to measure loss currents to different surfaces in the thruster. These probes differed from the small-area probes used to map the interior of the plasma in that they were planar and had much larger areas, on the order of a few square centimeters since the ion currents were generally quite small. In the case of the sides of the cathode assembly, they took the form of tantalum foils, insulated from and attached to the assembly with Kapton tape. Lead in wires were spot-welded to the foils. The foils were usually 1 cm wide and a few cm long, the long dimension being wrapped around the assembly. Losses to the front of the cathode assembly, excluding the heat fin attached to the cathode itself, were measured to a disk, with a concentric hole large enough to allow the actual cathode to protrude, which covered the entire front of the magnet and magnet holder outside of the heat fin and again held in place with Kapton tape. Some loss measurements were made using only a segment of such a disk. Measurements of ion loss currents to the heat fin were not made with plane probes, although the region near the heat fin was extensively investigated with the wire probes described previously. Measurements of loss currents to the walls were made with foils

taped to the walls and to the magnets, and also with discs embedded in the iron pole-faces (which were used when the Iowa thruster was in the line-cusp configuration) and with a plane probe attached to the same movable arm used with the wire probes and described above. Each of these arrangements has its conceptual problems and advantages. The foils seem in principle to be the best but there is the problem of lack of mobility and of getting the lead in wires out of the chamber without altering the plasma. Embedding discs in the pole-faces certainly provided the least disturbance of the plasma and the wires were taken out via a slit in the back of the pole-faces so they were completely isolated from the plasma region. However, the method unfortunately cannot be used in regions where such embedding is impractical, such as on the cathode assembly or between the magnets or in the cusp regions if pole-faces are not used. The movable probe has the advantage of complete mobility but probably produces the most severe perturbation of the plasma. Fortunately, results from all three types of probes were consistent in cases where they could be compared.

1.3 Scope of the Measurements

The various operating conditions under which the plasma parameters were measured for the line cusp configuration are shown in Fig. 1.1. In this figure the dots indicate parameter sets where

single measurements were made. The open circles are cases where extensive measurements were made at most points within the chamber.

The sets of thruster parameters for which loss measurements were made in the line cusp configuration are also shown in Fig. 1.1. The open squares indicate points where relatively extensive measurements were performed while at the points indicated by open triangles limited data were acquired. While not identical to the parameters for which the plasma parameters were mapped, there is enough overlap that results of the two types of measurements can be compared without unwarranted extrapolation.

Figure 1.2 illustrates the scope of the measurements for the ring cusp configuration. The significance of the various shapes for the points is the same as discussed above for Fig. 1.1. The fact that the ring cusp case was studied more more intensively than the line cusp case is not apparent from these figures because the difference is primarily in the number of interior points that were investigated in the two cases.

Section 2

EXPERIMENTAL RESULTS

The optimization of thruster design can be considered as the maximization of beam current for a given power input, or as the minimization of power input for a given beam current. It is some advantage to be able to consider plasma density instead of beam current in these considerations and this would of course be strictly possible if these two parameters were in direct proportion. The relation between beam current and plasma density determined by Langmuir probe measurements in the line cusp case is shown in Fig. 2.1. The approximate proportionality is obvious. For a given plasma density, the lower values of beam current correspond to higher values of discharge current. This effect is believed to be due to the increased gas flow rate which was used in order to produce the higher discharge current, which in turn increased the neutral pressure in the thruster thereby decreasing the beam current by collisional effects. It is not clear whether this effect would be as large in an experimental setup with more pumping capacity, but regardless of the experimental pumping speed, some beam reduction at high enough gas flow rates must occur since pumping of the chamber itself will be impeded by the extraction grids and acceleration electrodes. As a crude approximation, one can imagine the neutral gas to form a uniform cloud through which the ion beam must penetrate. In this case the beam current should vary with neutral

pressure p as $\exp(-bp)$, where b is some constant. Fig. 2.2 shows a semi-logarithmic plot of the ratio of beam current to plasma density versus neutral pressure, as indicated by the fore-pressure in the system diffusion pump, for the same data set used in Fig. 2.1. Assuming constant pumping speed the fore-pressure is proportional to the neutral pressure in the chamber. The data tend to support a pressure dependence of the type suggested, but the scatter clearly indicates the limitations of the model. It is clear that the beam current depends on the plasma density in the vicinity of the extraction grid. This density will depend on the rate of diffusion of ions into the region and the diffusion rate will depend on gradients in the plasma density and in plasma potential (the electric field). These gradients should be taken into account in a complete theory, although their effect seems to be relatively weak.

Some measurements of the spatial variations in plasma density are shown in Fig. 2.3 for the line cusp case. The gradients mentioned above are evident. Some measurements of the radial variation of the density are shown in Fig. 2.4. Clearly the plasma is approximately one-dimensional except for regions very near the walls. Various authors have given the results of calculations of plasma density for both planar and cylindrical geometries and with various assumptions about the ion production (Tonks and Langmuir, 1929; Kino and Shaw, 1966; Self, 1967). In all cases ion losses could occur only in one direction along the axis. The density was a

maximum over some plane and then decreased in the loss direction. In the thruster, losses occur at the extraction grid but also in the other end of the chamber on the cathode, which presents a surface with a total area comparable to the extraction port and which is biased at about the same negative potential as the extraction grid. The density is therefore a maximum near the center of the chamber and falls off in both directions. The solid lines shown in Fig. 2.3 are the calculations of Self (Self, 1967) normalized at the point of maximum density. In these calculations the ion production is assumed to occur throughout the chamber with a rate proportional to the electron density, a situation which is probably close to the situation in the thruster chamber. The agreement would seem satisfactory. These same calculations show little difference between the planar case and two dimensional results with cylindrical geometry. This is not surprising in view of the limited radial variation predicted in the two dimensional calculations and observed in the thruster as shown in Fig. 2.4.

Some examples of loss currents observed in the line cusp case are shown in Fig. 2.5. These are losses in the cusps and were obtained by measuring currents to disks imbedded in the iron pole-faces. The ion losses fall off in the half of the chamber near the grid at about the same rate as the axial decrease in density in this region. The increased loss to the cusps near the cathode is not understood however. The variation in electron losses along the

cusps also is not understood. The fact that the enhancements, relative to the interior plasma density, in the ion and electron losses are in opposite directions could possibly be explained by a force such as that due to an axial electric field very near the pole-faces (which, it should be remembered, are also the anodes for the discharge) or due to $E \times B$. However, the necessary fields have not been observed. The losses between the cusps are very small. Figure 2.6 shows the azimuthal and radial variation in density, electron temperature and plasma potential at a fixed axial position near the center of the chamber. The plasma density approaches zero at regions near the wall and between the cusps. These and other potential measurements were undertaken with the expectation of finding potential islands between the cusps such as have been observed in other surface cusp-confinement plasmas (Hershkowitz, et al, 1979). The results show, however, that the islands are not as well developed in the present case. This is consistent with the view that the islands form because of the need to equalize electron and ion losses when the electrons, but not the ions, are confined by the magnetic fields. The ion gyroradius is expected to be larger than the electron gyroradius by a factor of 86 for Argon, assuming the electron temperature is ten times the ion temperature. However, for the very strong magnets used in the thruster, the field between the cusps was about 1200 gauss so the ion gyroradius was about 3.5 mm. Thus ions were well confined by the magnetic fields and no additional electrostatic confinement was needed.

The ring cusp configuration presents a considerably different plasma situation. This is because the bulk of the plasma is no longer in a nearly magnetic field free region, as with the line cusp case. The radial variation of the magnitude of B measured in the line cusp case is shown in Fig. 2.7 as the solid lines. The upper solid line was measured along a radius connecting opposite pole-faces and the lower solid curve was measured along a radius between the cusps. The dashed curves show the same thing for the ring cusp case. The upper dashed curve is for an axial position corresponding to one of the rings and the lower dashed curve is at an axial position between rings. The magnetic field in the central region is larger and less homogeneous in the ring cusp case. One of the results of this difference is a considerable increase in the radial density gradients and potential gradients. Enough data were taken for the ring cusp configuration to allow the construction of contour plots to display the plasma parameters throughout the device. Examples are shown in Figs. 2.8, 2.9 and 2.10. The axial variation in the plasma density is shown in Fig. 2.11. This result differs from that shown in Fig. 2.3 in two ways. The most obvious is the large increase in density in the vicinity of the cathode. Some considerations of the plasma production process will be given in the next section. For now we note only that this increase in density is consistent with the visual observation of a very bright tapered column near the cathode orifice which was not noticed in the line cusp case. It is clear from this observation and from Fig. 2.11

that much more plasma production occurs along the central column near the cathode in the ring cusp case. The second difference is that the agreement with the calculations of Self, shown by the dashed line in Fig. 2.11, is not as satisfactory. It is clear from Fig. 2.10 that the situation is very two dimensional now. A comparison of the radial variation of plasma density would show even greater disagreement between theory and experiment. This is perhaps not surprising in view of the reduced homogeneity of plasma production. The density variations in both the radial and axial directions could possibly be fit by Self's results, which assume a sort of volume production of plasma, superimposed on a large peak which is centered a few centimeters in front of the cathode and falls off in all directions, perhaps as a Gaussian, which would result from relatively localized plasma production near the cathode orifice. Self's calculations, in which plasma production is proportional to electron density would be appropriate if such a Gaussian peak in electron density could be introduced self consistently.

Two different arrangements of the ring cusps were investigated in addition to the one discussed above. One of these, which had four rings instead of five, was found to have extremely poor efficiency and so no very extensive measurements were made. The other arrangement was identical to the first except the magnet ring on the base plate was inverted. This change was suggested by

calculations of the magnetic field which were performed on various geometries with the object of increasing the flux which directly linked the cathode with the extraction grid. Figures 2.12 and 2.13 are of the magnetic field directions in the two cases and show the increase in flux linkage in the second design. Figures 2.14, 2.15 and 2.16 show the plasma density, plasma potential and the electron temperature for this case. The axial variation in plasma density was shown in Fig. 2.12. The increase in density near the cathode is not as steep as for the first case and the agreement with Self's calculations is not better. The plasma extends further away from the center but the radial gradients are still high and the plasma is still not planar over any appreciable area.

Loss currents in the cusps and to the cathode for the ring cusp in the first configuration are shown in Figs. 2.17 and 2.18. These data were obtained with foils fixed to the various surfaces. Figure 2.19 shows a continuous distribution of ion currents over part of the axial range for the second ring cusp configuration. These data were obtained with a thin rectangular plate (3.2 mm X 12.8 mm) swept axially at a radial position 2 mm from the magnet pole-faces. Figure 2.21 shows representative loss distributions for the second ring cusp case for several sets of operating parameters. Of the sets that were investigated, the one indicated by dashed lines had the lowest beam cost factor (148 watts/amp) and for this case the losses are significantly lower to rings C, D and E. However, the

beam-cost factors for the other cases shown vary greatly and there is no significant difference between the relative losses to the various rings. These data, and those shown in Fig. 2.18, show axial variations in ion loss flux quite similar to what was seen in the line cusp case. In this case, there is a close parallel to the axial variation in plasma density. The electron losses shown in Fig. 2.17 also show a correspondence to the local plasma density in contrast to the observation in the line cusp case. However, the magnitude and inhomogeneity of the magnetic field in the interior of the chamber makes the correlation between losses and density different in this case. Even in regions where the magnetic field is weakest the electron gyroradii are less than a millimeter and in most regions they are less than 0.1 mm. Almost all plasma electrons are trapped in this case and losses depend on scattering of electrons into loss cones. Of course the rate of such scattering depends on the electron density and so the loss fluxes should depend on density as is observed. The data shown in Fig. 2.19 show that there are significant ion losses between the cusps. In fact there is more total ion flux between rings A and B than there is in either ring A or B. Overall the ion loss between cusps is between 50% and 100% of the loss in the cusps. The elimination of these between-cusp losses would seem to be an attainable objective if further improvements in thruster performance is desired.

Of the three geometries that were extensively investigated, the second ring cusp arrangement gave the lowest beam cost factor. The lowest actual ratio of input power to beam current was 205 watts/amp. The beam current was collected on a screen with a geometric transmission of 0.36 so if 100% of the beam were extracted the beam cost factor would be 131 watts/amp. The corresponding best value with the ring cusps in the first arrangement was 165 watts/amp. In the line cusp arrangement beam cost factors of 180 watts/amp were achieved and in this case the beam was collected on a solid sheet so no correction was needed. It is likely that further improvements in the beam cost factor could be achieved by variations in the positioning of the rings but this has not been attempted.

Some insight into the nature of the problem of optimizing thruster design can be obtained by studying the orbits of ions in the thruster. To this end a program was written to calculate exactly the orbits in the multi-dipole magnetic field which exists in the thruster and in an electric field which is obtained from the experimentally determined potential. The magnetic fields were calculated analytically by replacing the magnet rings with two current loops nearly coincident with radii equal to the radius of the magnet rings and with oppositely flowing currents. The electric fields were approximated by analytic functions. The experimental potential for a particular set of plasma parameters was shown in Fig. 2.15. The analytic potential used in the orbit calculations is shown in Fig. 3.1. The magnetic field used in the orbit calculations is shown in Fig. 3.2. This field can be easily changed by changing the current-loop parameters. The ions were assumed to be born at various points throughout the thruster although most of the calculations were performed at points on axis or just off axis. Various initial energies were assumed for the ions. In all cases calculations were done for all initial directions between 0 and 180 degrees in two degree intervals. The orbits were followed until the ions contacted some surface.

Some examples of orbits calculated for ions born with very low energy near the exit orifice are shown in Figs. 3.3 and 3.4. In plot 3.3a) the source was at an axial position of 17.0 cm and 0.1 cm off axis. Almost all of the ions are lost to the back plate. They are forced there by the electrostatic field and are not well confined by the back-plate magnet ring. The reflections that seem to occur on the horizontal axis would be simply continuations into the lower quadrant, but are plotted as shown to conserve space in the figure. Plot 3.3b shows orbits for a source on axis at a radial position of 16.9 cm and plot 3.3d has the source at the same radial position but displaced 0.1 cm from the axis. Considerably more of the ions get to the extraction grid (10% in plot 3.3b and 13% in plot 3.3d)). Two conclusions are to be drawn from this: First, a very slight change in the position the ions are born makes a large change in the likelihood that the ion will reach the extraction grid. Second, since very little loss flux is observed to the back-plate magnet ring (see Figs. 2.18 and 2.21) not many of the ions are born on the cathode side of the potential maximum near the cathode (shown in Figs. 2.9 and 2.15). The source in plot c) is at an axial position of 16.0 cm and .1 cm off axis. There are 46 orbits that hit the extraction grid, 36 that hit the cusp at 5.2 cm and are not mirrored, and 8 that hit the back plate. Figure 3.4 shows orbits for ions born at 16.0 cm, 0.1 cm off axis, and at 14.0, 12.0 and 9.0 cm, all on axis. The increase in the probability of being extracted as the point of origin moves toward the grid is

obvious. Figure 3.5 shows orbits for ions born with energies of 0.4 eV at a) 16.9 cm, b) 16.0 cm, c) 14.0 cm and d) 12.0 cm. Figure 3.6 shows the same thing for ions born with 1.0 eV at the same points. Ions with 1.0 eV, and even higher energies, can arise from charge exchange with fast neutrals. The fast neutrals arise from neutralization at the walls of ions which fall from the central region where the potential is on the order of 4 volts positive relative to the walls. These neutrals then travel back into the central region without further change in energy, except by collisions, until they either charge exchange with a low energy ion, creating a fast ion, or drift out of the extraction port. However, an examination of the various orbits indicates that the dependence on energy is very slight. The dependence on the position of origin, relative to the potential, is significant. Although there is not a monotonic relationship it seems that the nearer to the grid that ions originate, the better chance they have of being extracted, a not surprising conclusion. This dependence on the potential points out what is probably the most important deficiency in this treatment. In a complete theory the potential would be determined self-consistently as the structure required to keep charge densities and fluxes balanced. To impose a potential and then look at particle orbits can provide the basis for a few generalities, but can probably not be used as the basis for a quantitative treatment of the device.

It is also clear that the magnets are sufficiently strong to confine the ions, which is consistent with the fact that potential islands do not occur between the cusps. In almost no cases do any of the orbits terminate on the side walls between the cusps. This is contrary to the observation, illustrated in Fig. 2.19, that total between-cusp losses are comparable to losses in the cusps. The conclusion is that diffusion plays an extremely important roll in determining the performance of the thruster. This of course is a second reason that orbit calculations have limited quantitative use. These calculations do, however, show the extreme importance of the position at which the ions are born.

In view of this, it is clear that considerations of ion production are at least as important as considerations of ion loss in calculations of thruster performance. There are two aspects to this part of thruster operation. First, as the orbit calculations show, for a given ion production rate, lower beam cost factors will result if the average ion production position can be moved toward the extraction grid. Second, it is desirable to optimize the ion production rate for a given discharge current. In his thesis, Boardsen shows that bulk ion production due to thermal plasma electrons can account for only from 10% to 30% of the ion production (Table 5 in the thesis). He finds a very hot dense region near the cathode where apparently most of the ionization occurs. The temperatures of electrons in this region have been remeasured and we

find that the extremely high values reported by Boardsen were probably in error, due to overloading of the electron current measuring circuit. The temperatures are very high in this region, however, reaching 7.9 eV at a point on axis and 6 cm from the exit orifice. It was not possible to make reliable measurements on axis at points closer to the orifice than this because of probe damage, even using extreme care. At points just 1 cm off axis, however, the electron temperature drops to 2 to 3 eV, even 1 cm from the orifice, and the density is low enough that measurements can be performed. This implies a jet-like beam of electrons from the cathode which is well confined by the axial magnetic field in this region. If this beam were to continue without interaction it would be reflected by the extraction screen, return to the cathode where it would be reflected again and possibly make several such loops before being deflected or making ionizing collisions. However, visual observations as well as density and temperature measurements make it clear that the beam is rapidly thermalized within 5 to 10 cm from the cathode. It is believed that as much as 70% of the ion production occurs within this region. This extremely efficient conversion of the energy deposited in the chamber by the discharge current electrons into ionization may be the principal reason for the high performance observed in the ring cusp case. The mechanism for this conversion is not known but is probably connected with an instability, perhaps associated with the production of electron cyclotron waves, which could be excited by a beam-plasma interaction

with electrons accelerated at the cathode exit orifice. Stable double layers, needed for the strong electric fields required for such acceleration, are known to exist at points where the plasma column changes diameter (Andrews and Allen, 1971) and in diverging magnetic fields (Alport et al, 1986). Both of these conditions exist at the cathode orifice so the existence of a stable strong double layer is almost guaranteed. Intense UHF noise has been observed in the high potential side of similar double layers in cases where rapid thermalization of the beam electrons is also observed (Lindberg, 1982a and 1982b). It might be the case that various changes in thruster performance observed here and elsewhere are due, not so much to changes in losses of ions to the walls, but to changes in ion production rates due to modification of the environment near the cathode orifice. At any rate, this is an area that should be thoroughly investigated in future thruster studies.

FINAL SUMMARY STATEMENT

In spite of the dense hot plasmas that exist in ion thrusters, it is possible to investigate their plasma properties with simple modifications of standard techniques. It is found that in the line cusp configuration the plasma density is essentially as predicted by existing calculations (e.g. Self, 1967). In particular the calculations of Kino and Shaw (1966), which were motivated by the thruster program, give ion currents which should be directly comparable to the results obtained at NASA-Lewis. In the ring cusp arrangement the interior of the plasma contains an inhomogeneous and relatively large magnetic field so the geometry is decidedly two-dimensional and it is observed that the models of Self (1967) and of Kino and Shaw (1966) do not agree with experiment. It is observed in the ring cusp case that ion losses between the cusps are rather larger than in the line cusp case. It should be possible to eliminate these losses by electrostatic means and this would permit a modest increase in the performance with a slight increase in complexity. These between-cusp losses are not predicted by exact ion orbit calculations and this indicates that ion-ion and ion-neutral collisions play a very significant role in actual thruster performance. A difference between the ring cusp and line cusp operation is that relatively more of the ion production occurs in a region near the cathode exit orifice in the ring cusp case. It

is suggested that changes in ion production characteristics may be largely responsible for changes in performance figures as various configurations are tested. Also, this effect cannot be ignored as a contributor to changes in the beam cost factor when discharge voltage and current are varied with a given configuration. Further attempts to understand thruster operation with a view toward improving performance should undertake the clarification of the role of ion production processes in this system.

REFERENCES

- Alport, M. J., S. L. Cartier and R. L. Merlino, Jour. Geophys. Res. 91, 1599 (1986)
- Andrews, J. G., and J. E. Allen, Proc. Roy. Soc. Lond. A.320, 459 (1971)
- Boardsen, Scott, Master's Thesis, University of Iowa, Unpublished, 1984
- Chen, Francis F., in Plasma Diagnostic Techniques, ed. Richard H. Huddlestone, Academic Press, 1965
- Hershkowitz, Noah, John R. Smith and Hideo Kozima, Phys. Fluids 22, 122 (1979)
- Kino, G. S. and E. K. Shaw, Phys. Fluids 9, 587 (1966)
- Lindberg, L., Proc. Int. Conf on Plasma Physics, Gothenberg (1982a)
- Lindberg, L., Proc. Symposium on Plasma Double Layers, Riso, (1982b)
- Self, S. A., Phys. Fluids 10, 1569 (1967)
- Sovey, J. S., Proc. Int. Electrical Propulsion Conference, Las Vegas, paper number AIAA-81-0745, 1981
- Sovey, J. S., Proc. Int. Electrical Propulsion Conference, New Orleans, 1982
- Tonks, L. and I. Langmuir, Phys Rev. 34, 876 (1929)

FIGURE CAPTIONS

- Fig. 1.1 The "17 cm" NASA-Lewis ion thruster used in the current work with the following changes: The ground screen and the shell for ion optics mounting were not used. The anodes were removed. There were 9 magnet rows of each polarity.
- Fig. 1.2 Hollow cathode assembly used in all phases of this work. The heater which surrounds the front of the cathode was covered with four or five layers of tantalum foil, tightly wound and spot-welded in place. This and the entire tube was then covered with two or three layers of loosely wound tantalum foil. Three tantalum foil discs heat-protected the magnet in the front. The magnet was tightly fit into a stainless steel sleeve and held in place with set screws. The back plate which holds the cathode was held in place with screws and an adjustable telescoping sleeve.
- Fig. 1.3 Magnet holders used in the line cusp configuration. The tabs cut in the ends of the iron pole faces overlap the brass holders and retain the magnets.
- Fig. 1.1 Sets of discharge voltages and currents where measurements were performed in the thruster in the line cusp configuration. See text for the significance of the various symbols.
- Fig. 1.2 Sets of discharge voltages and currents where measurements were performed in the thruster in the ring cusp configuration. See text for the significance of the various symbols.
- Fig. 2.1 Beam current versus plasma density for the line cusp case.
- Fig. 2.2 The ratio of beam current to plasma density versus neutral pressure for the line cusp case.
- Fig. 2.3 Plasma density versus position for the line cusp case. The upper graph is for a discharge voltage of 38.0 V and a discharge current of 19.6 A. The corresponding values for the lower graph are 43.6 V and 15.1 A.
- Fig. 2.4 Radial variation of plasma density for the line cusp case for three different sets of operating parameters.
- Fig. 2.5 Losses along the cusps in the line cusp configuration. Ion losses are shown in the upper graph and electron losses in the lower graph.
- Fig. 2.6 Contour plots showing the variation in (a) electron temperature (b) plasma potential and (c) plasma density as they depend on the azimuthal position y and distance from the wall x (which is at 150 mm) at a point near the middle of the thruster in the line cusp configuration.
- Fig. 2.7 Radial variation of the magnitude of the magnetic field in the line cusp case (solid curves) and the ring cusp case (dashed curves). In both cases the upper curves are along radii through the cusps and the lower curves are along radii between the cusps.

- Fig. 2.8 Contour plot of the electron temperature for the ring cusp case.
- Fig. 2.9 Contour plot of the plasma potential in the ring cusp case.
- Fig. 2.10 Contour plot of the plasma density in the ring cusp case.
- Fig. 2.11 Axial variation of the plasma density in the ring cusp case.
- Fig. 2.12 Magnetic field near the axis of the thruster for the ring cusp case in arrangement number 1. The lines show the calculated directions of the magnetic field. The density of lines has absolutely no meaning. Note that only two of the lines which pass through the extraction grid connect to the cathode.
- Fig. 2.13 Same as Fig. 2.12 except for arrangement number 2. Note the increase in the number of magnetic field lines that connect the cathode and the extraction grid.
- Fig. 2.14 Contour plot of the electron temperature for the ring cusp case in arrangement number 2.
- Fig. 2.15 Contour plot of the plasma potential for the ring cusp case in arrangement number 2.
- Fig. 2.16 Contour plot of the plasma density for the ring cusp case in arrangement number 2.
- Fig. 2.17 Electron loss currents to the cusps in the ring cusp case, arrangement number 1. There were no electron currents to the cathode or to the extraction grid. The letters defining the cusps refer to the same locations as shown in Fig. 3.2.
- Fig. 2.18 Ion loss currents to the cusps and cathode in the ring cusp case, arrangement number 1. The letters defining the cusps refer to the same locations as shown in Fig. 3.2.
- Fig. 2.19 Ion loss currents to a thin movable strip in the ring cusp case, arrangement number 2. The letters defining the cusps refer to the same locations as shown in Fig. 3.2.
- Fig. 2.20 Representative ion currents in the ring cusp case, arrangement number 2, for several operating conditions. The letters defining the cusps refer to the same locations as shown in Fig. 3.2.
- Fig. 3.1 Analytic function used to approximate the potential in order to calculate ion orbits.
- Fig. 3.2 Calculated magnetic field used in the orbit calculations.
- Fig. 3.3 Ion orbits for ions born with an energy of 0.1 eV. In each figure there are 91 orbits corresponding to initial directions from 0 to 180 degrees in 2 degree steps. The four figures correspond to four different starting points. See text for details.
- Fig. 3.4 Same as Fig. 3.3 for four other starting points.

Fig. 3.5 Same as Fig. 3.3 except the initial ion energy is 0.4 eV.

Fig. 3.6 Same as Fig. 3.3 except the initial ion energy is 1.0 eV.

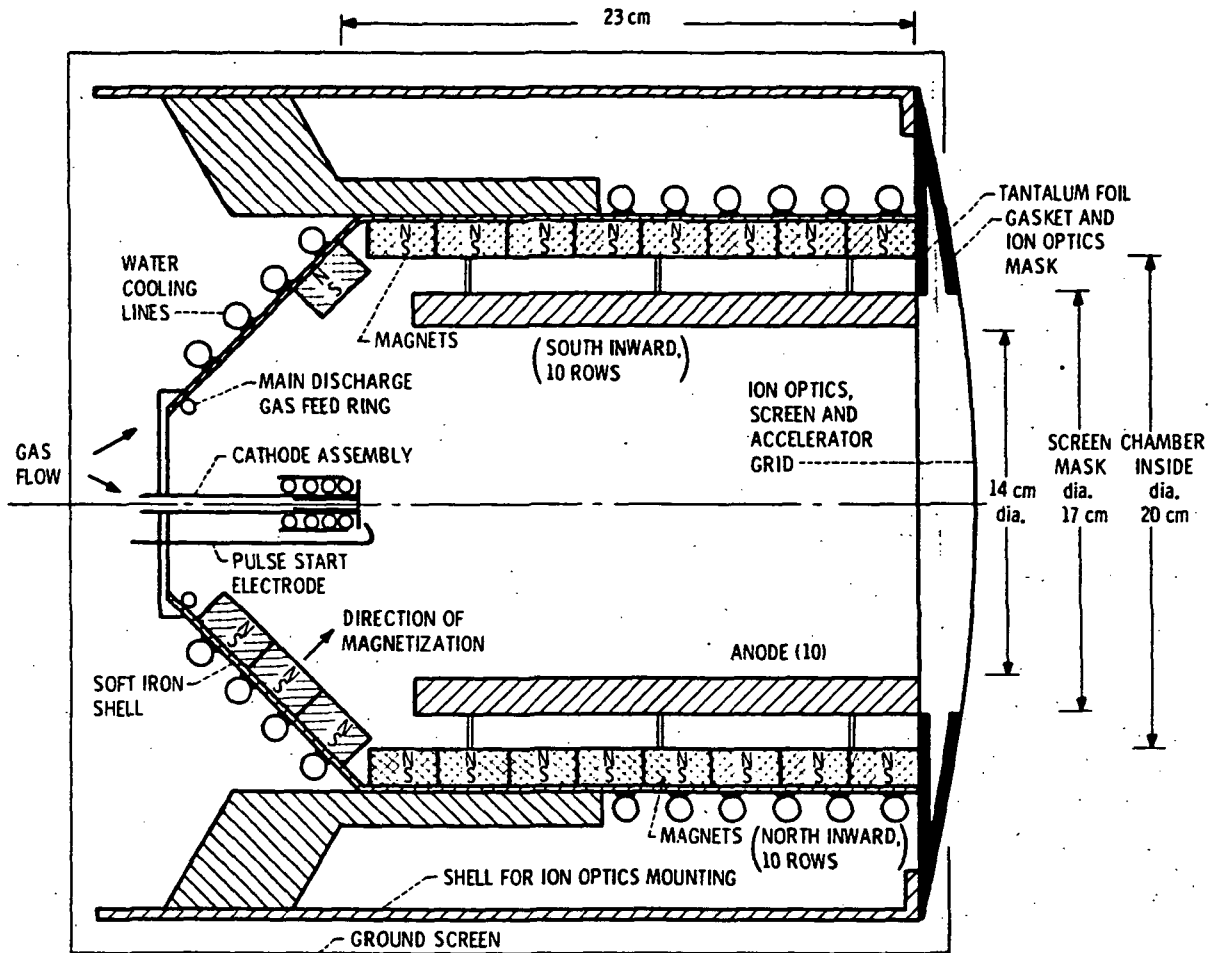


Fig. I.1 The "17 cm" NASA-Lewis ion thruster used in the current work with the following changes: The ground screen and the shell for ion optics mounting were not used. The anodes were removed. There were 9 magnet rows of each polarity.

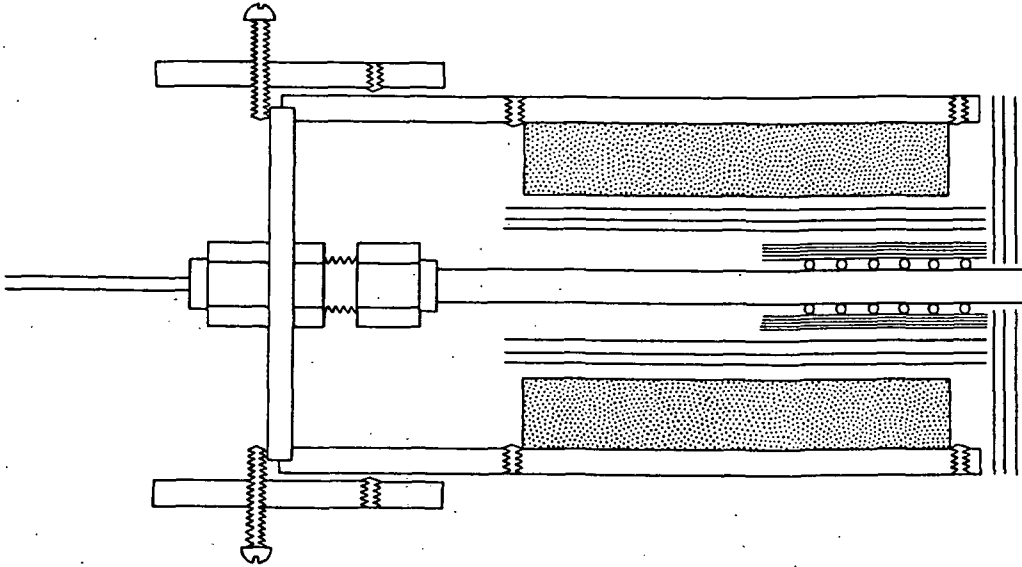


Fig. I.2 Hollow cathode assembly used in all phases of this work. The heater which surrounds the front of the cathode was covered with four or five layers of tantalum foil, tightly wound and spot-welded in place. This and the entire tube was then covered with two or three layers of loosely wound tantalum foil. Three tantalum foil discs heat-protected the magnet in the front. The magnet was tightly fit into a stainless steel sleeve and held in place with set screws. The back plate which holds the cathode was held in place with screws and an adjustable telescoping sleeve.

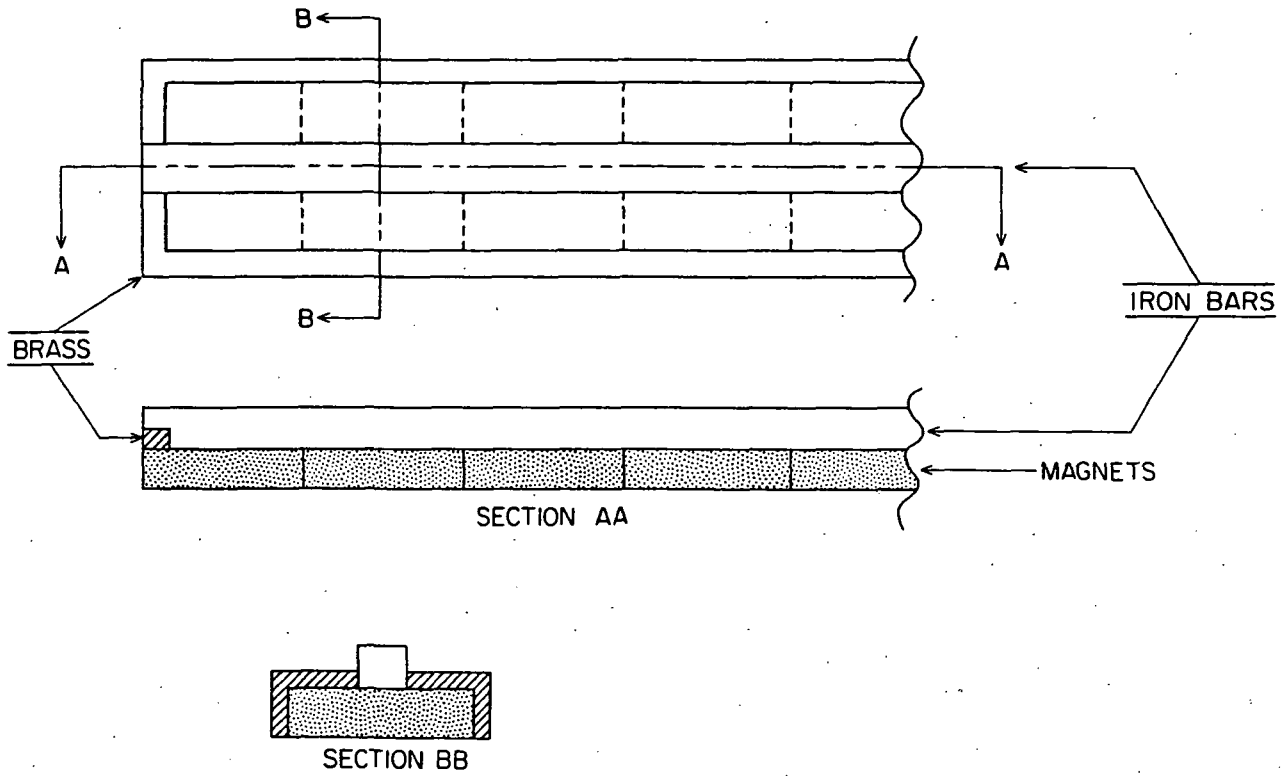


Fig. I.3 Magnet holders used in the line cusp configuration. The tabs cut in the ends of the iron pole faces overlap the brass holders and retain the magnets.

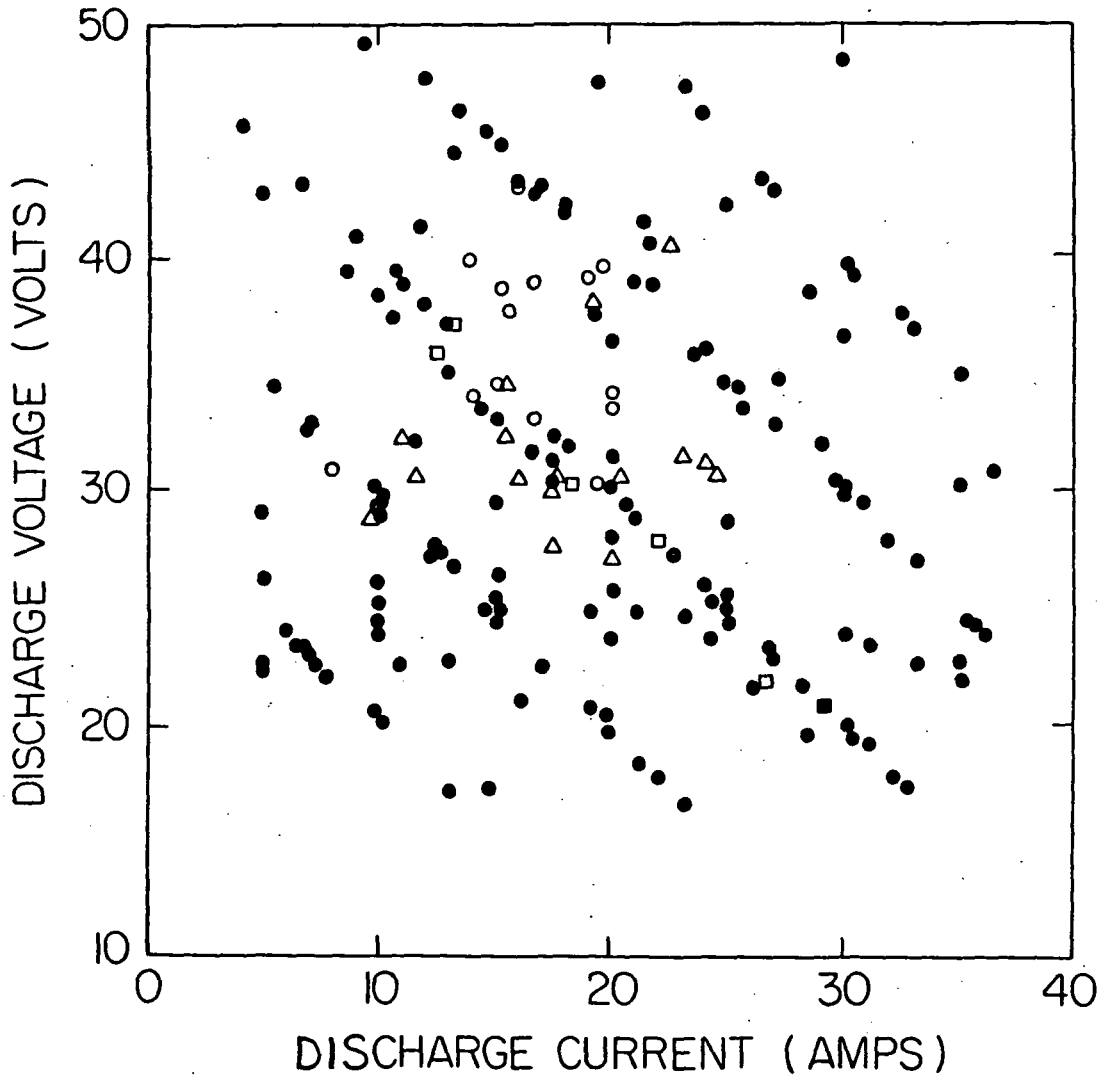


Fig. 1.1 Sets of discharge voltages and currents where measurements were performed in the thruster in the line cusp configuration. See text for the significance of the various symbols.

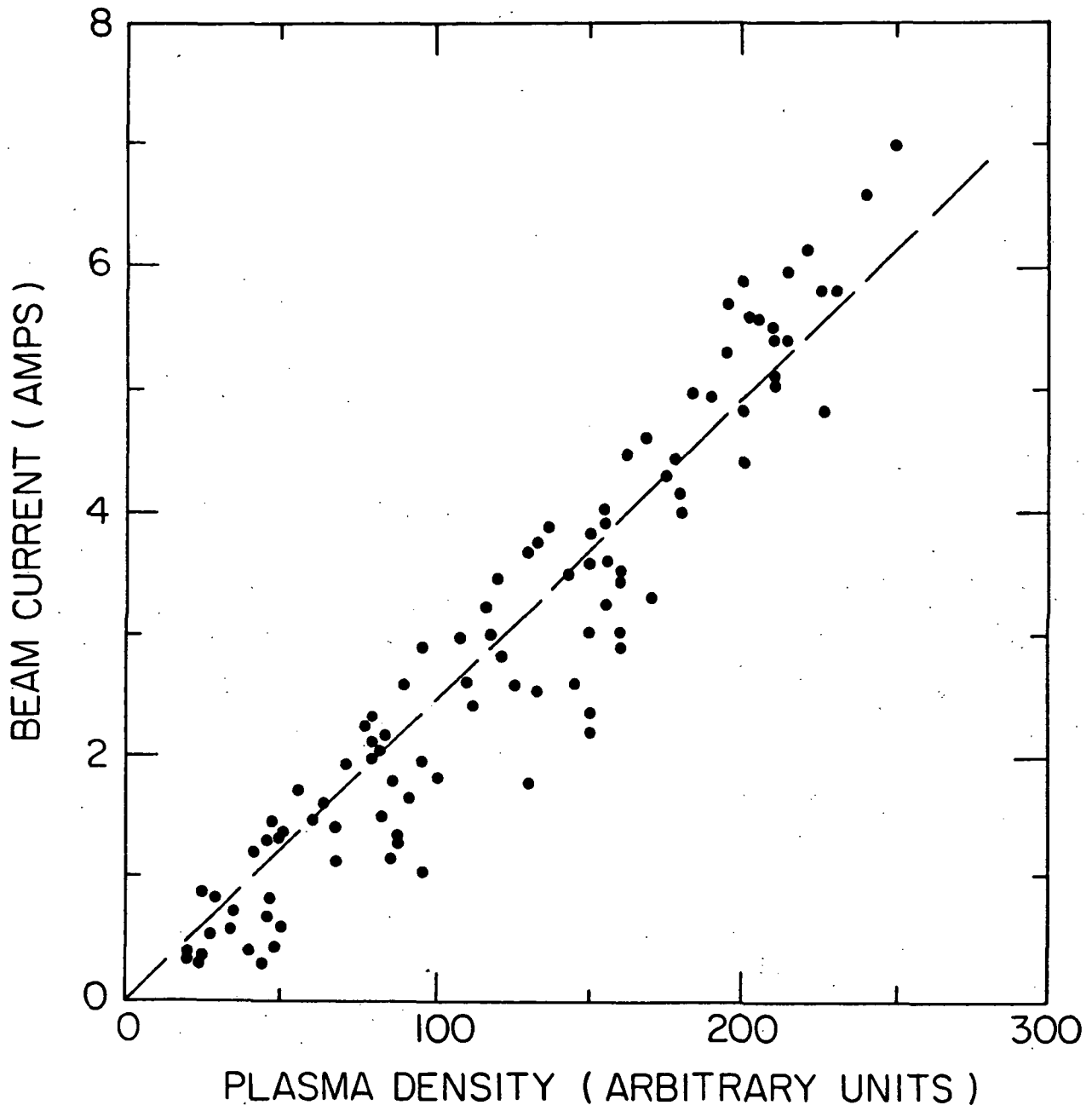


Fig. 2.1 Beam current versus plasma density for the line cusp case.

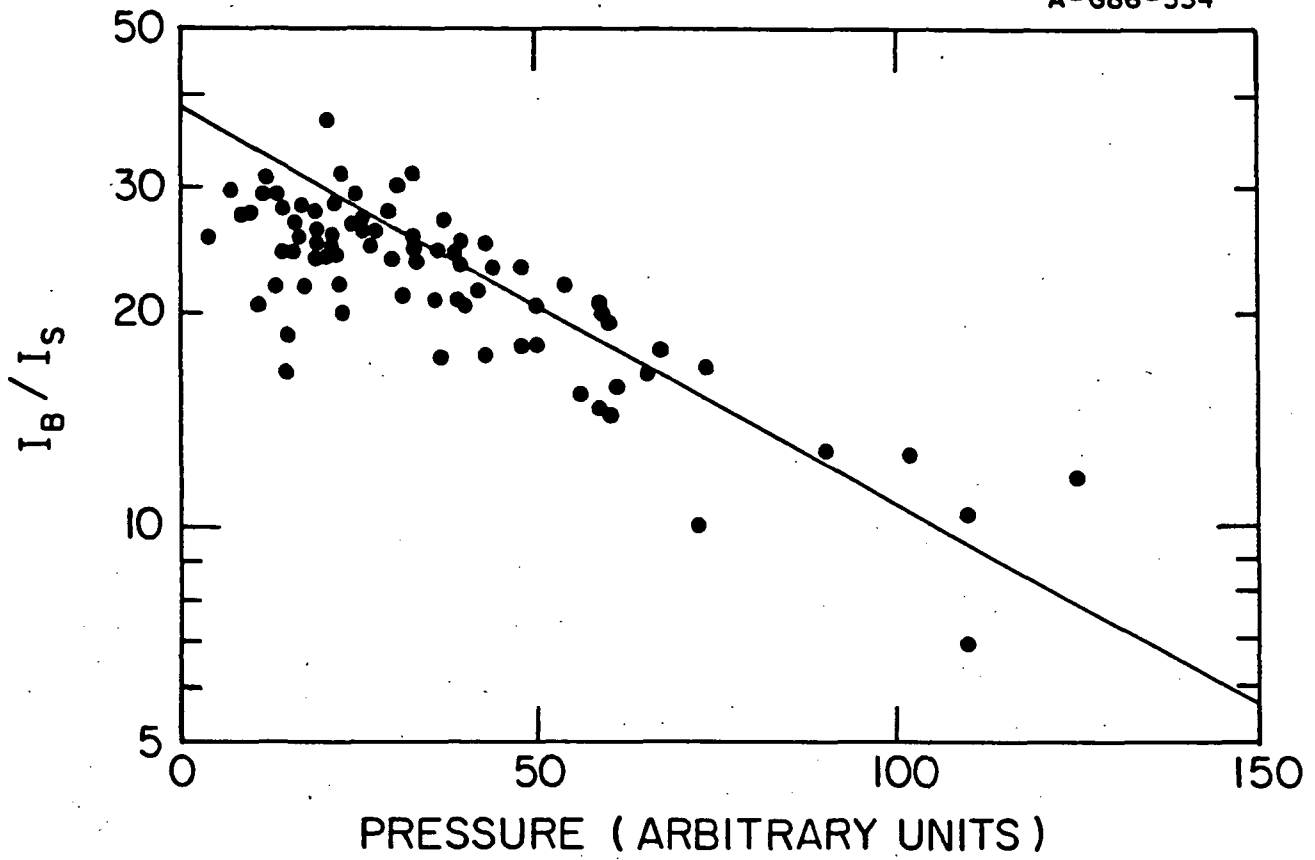


Fig. 2.2 The ratio of beam current to plasma density versus neutral pressure for the line cusp case.

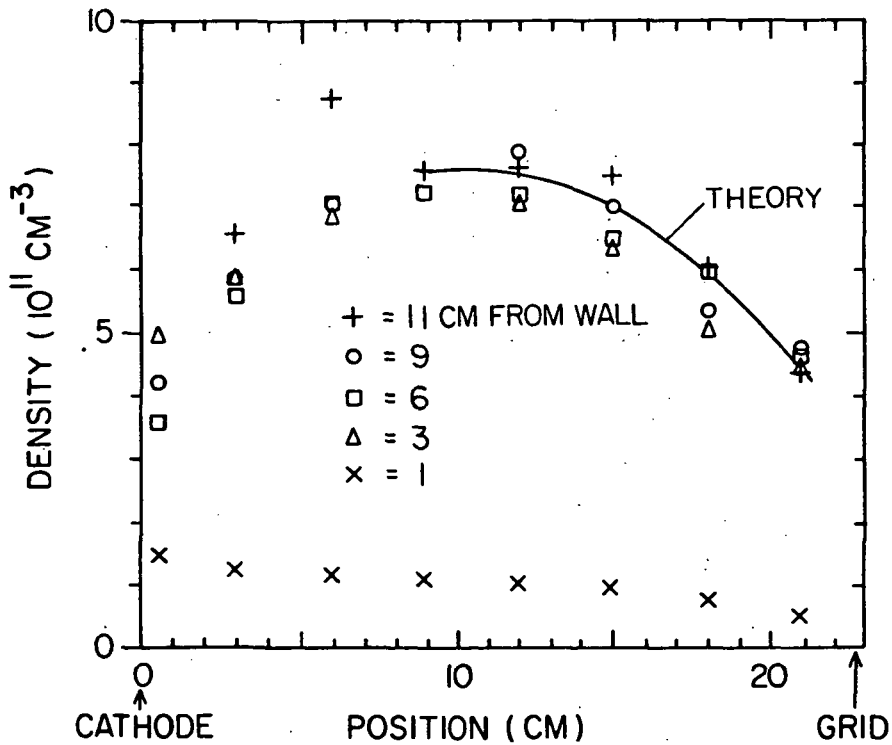
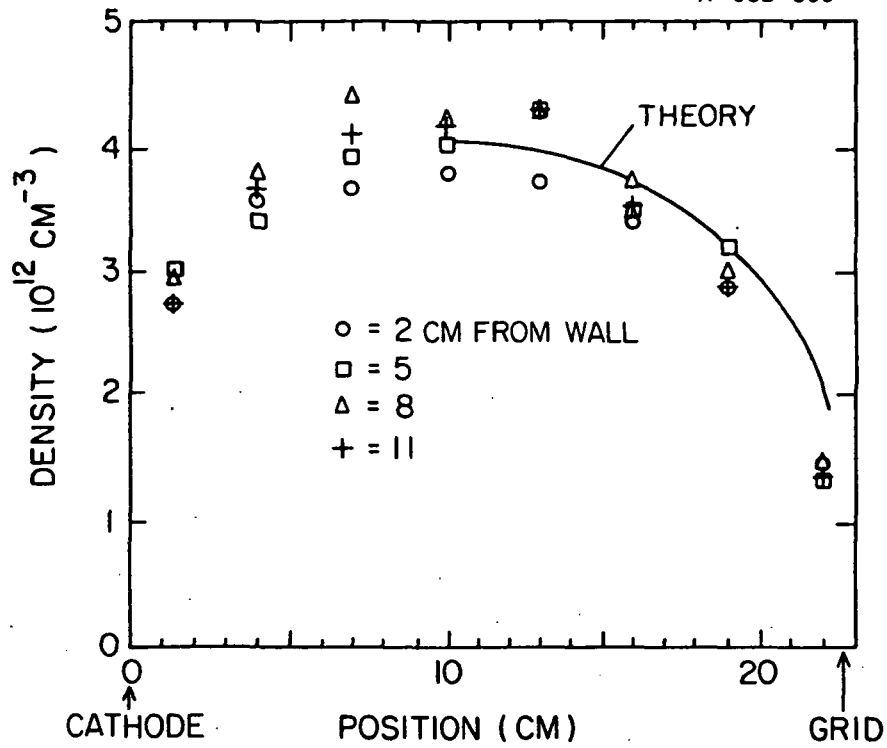


Fig. 2.3 Plasma density versus position for the line cusp case. The upper graph is for a discharge voltage of 38.0 V and a discharge current of 19.6 A. The corresponding values for the lower graph are 43.6 V and 15.1 A.

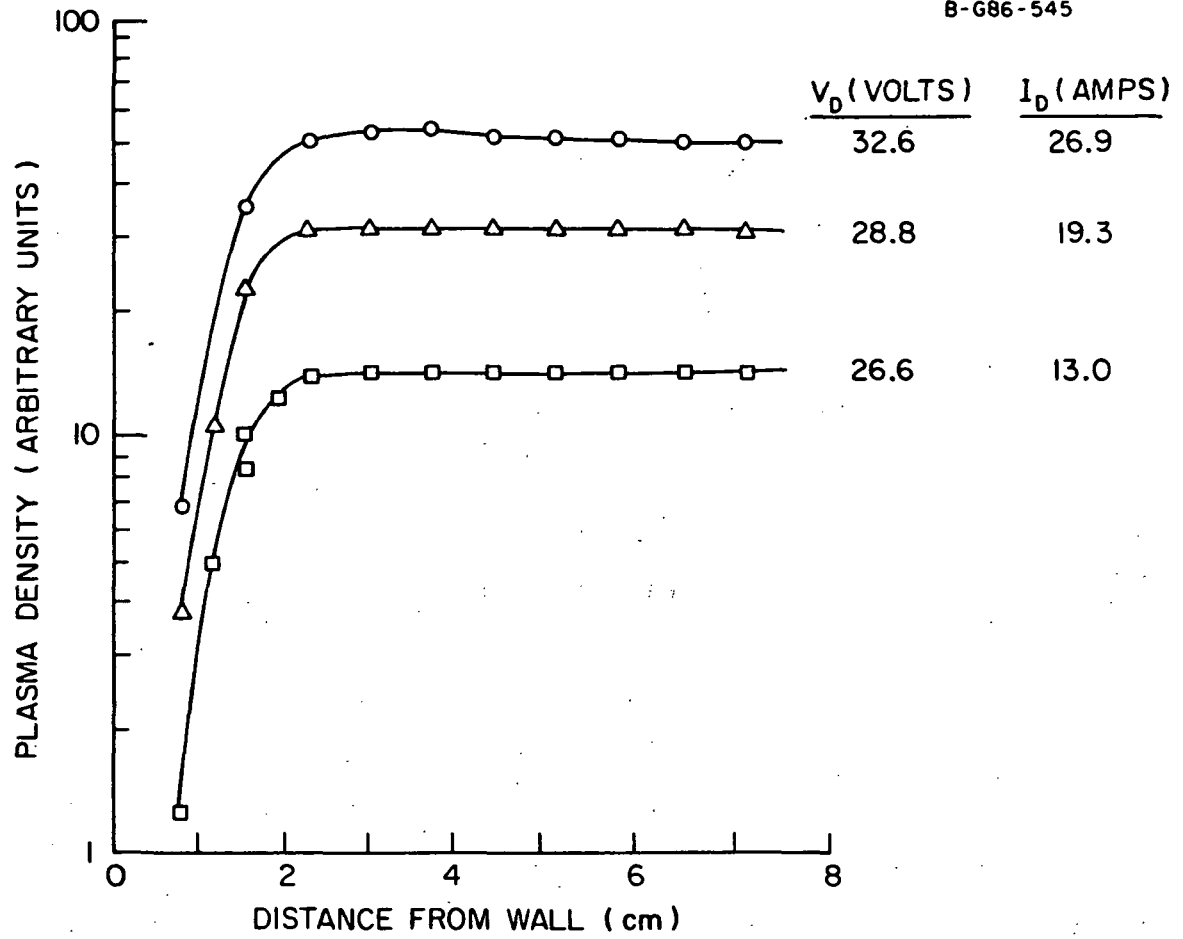


Fig. 2.4 Radial variation of plasma density for the line cusp case for three different sets of operating parameters.

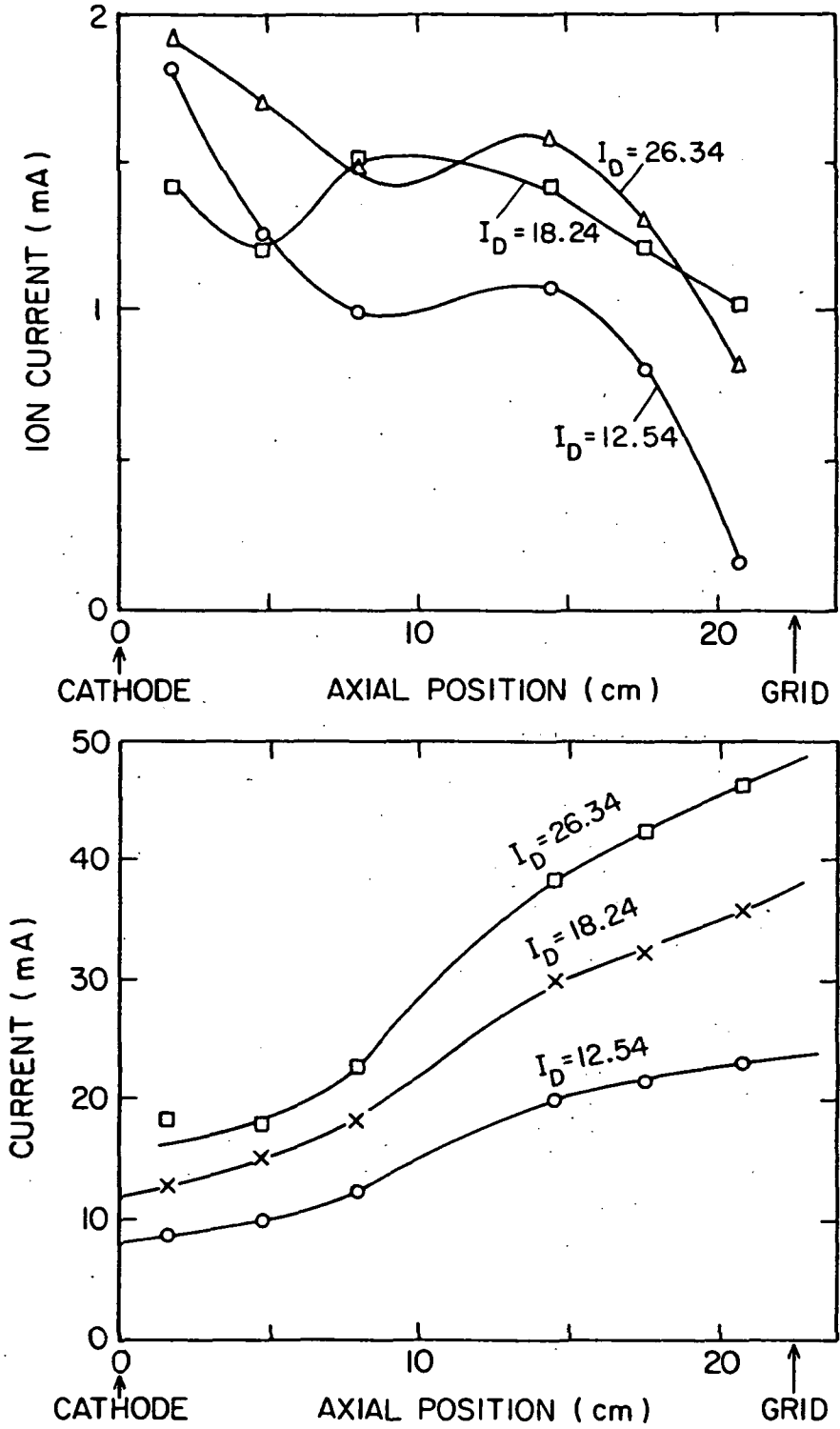


Fig. 2.5 Losses along the cusps in the line cusp configuration. Ion losses are shown in the upper graph and electron losses in the lower graph.

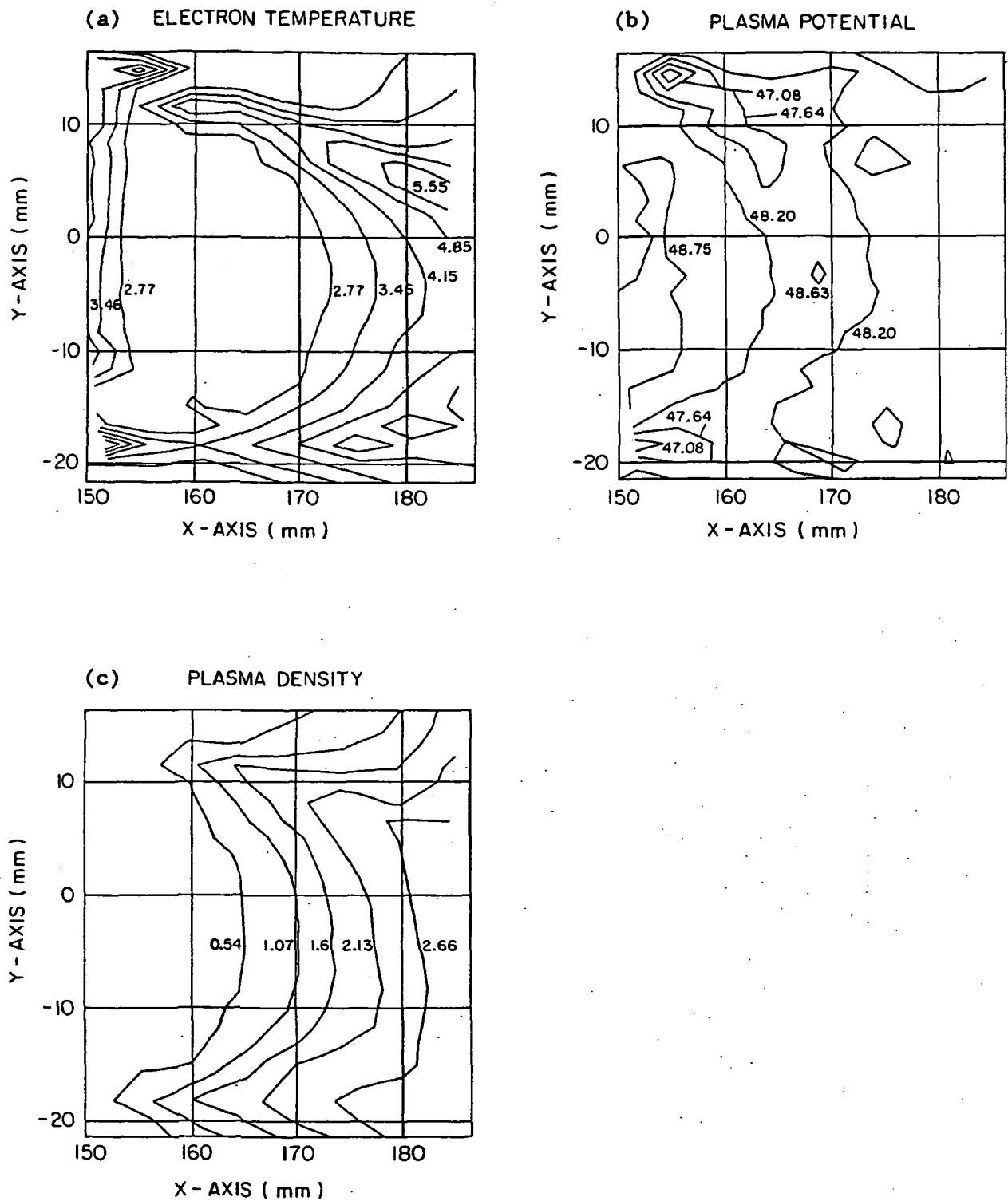


Fig. 2.6 Contour plots showing the variation in (a) electron temperature (b) plasma potential and (c) plasma density as they depend on the azimuthal position y and distance from the wall x (which is at 150 mm) at a point near the middle of the thruster in the line cusp configuration.

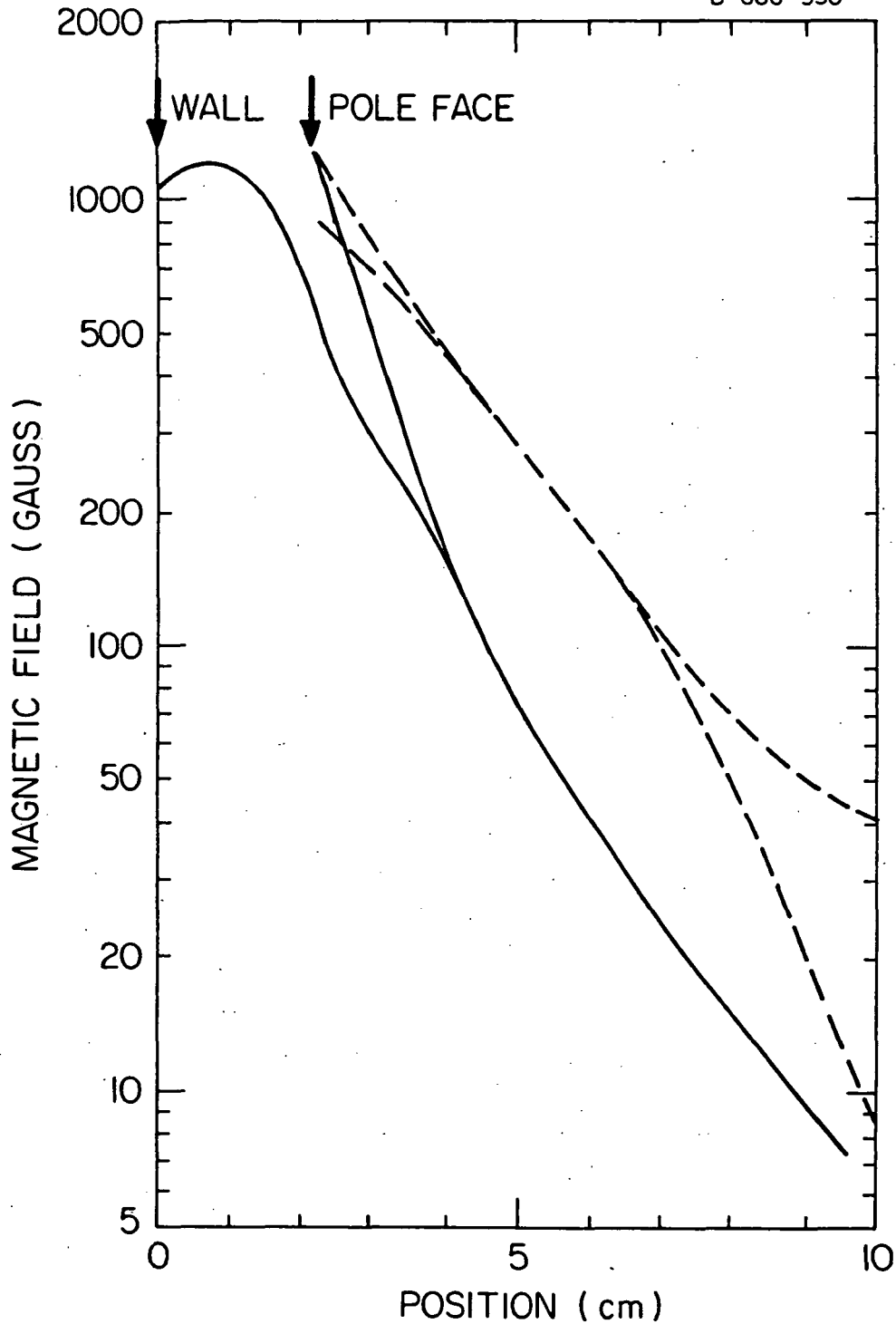


Fig. 2.7 Radial variation of the magnitude of the magnetic field in the line cusp case (solid curves) and the ring cusp case (dashed curves). In both cases the upper curves are along radii through the cusps and the lower curves are along radii between the cusps.

ELECTRON TEMPERATURE

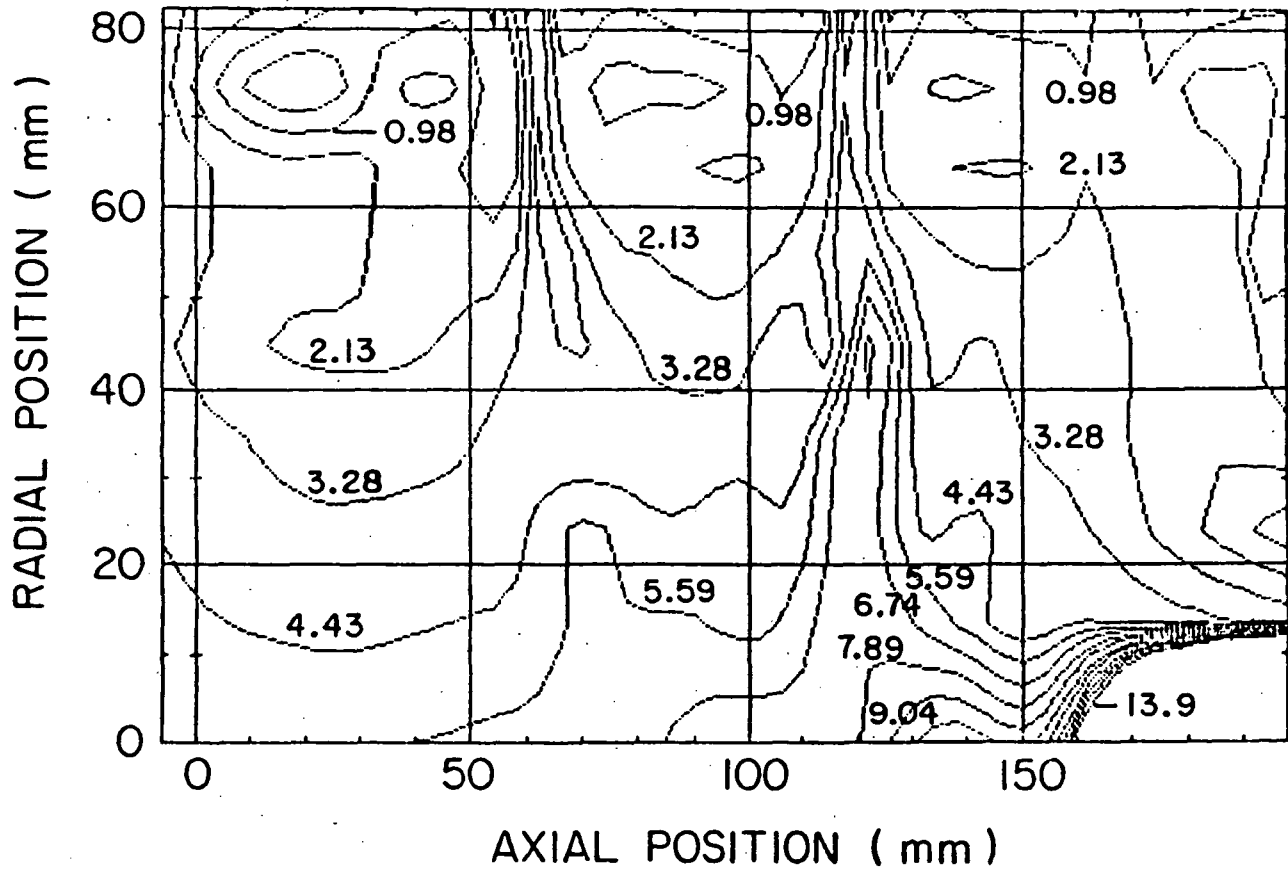


Fig. 2.8 Contour plot of the electron temperature for the ring cusp case.

PLASMA POTENTIAL

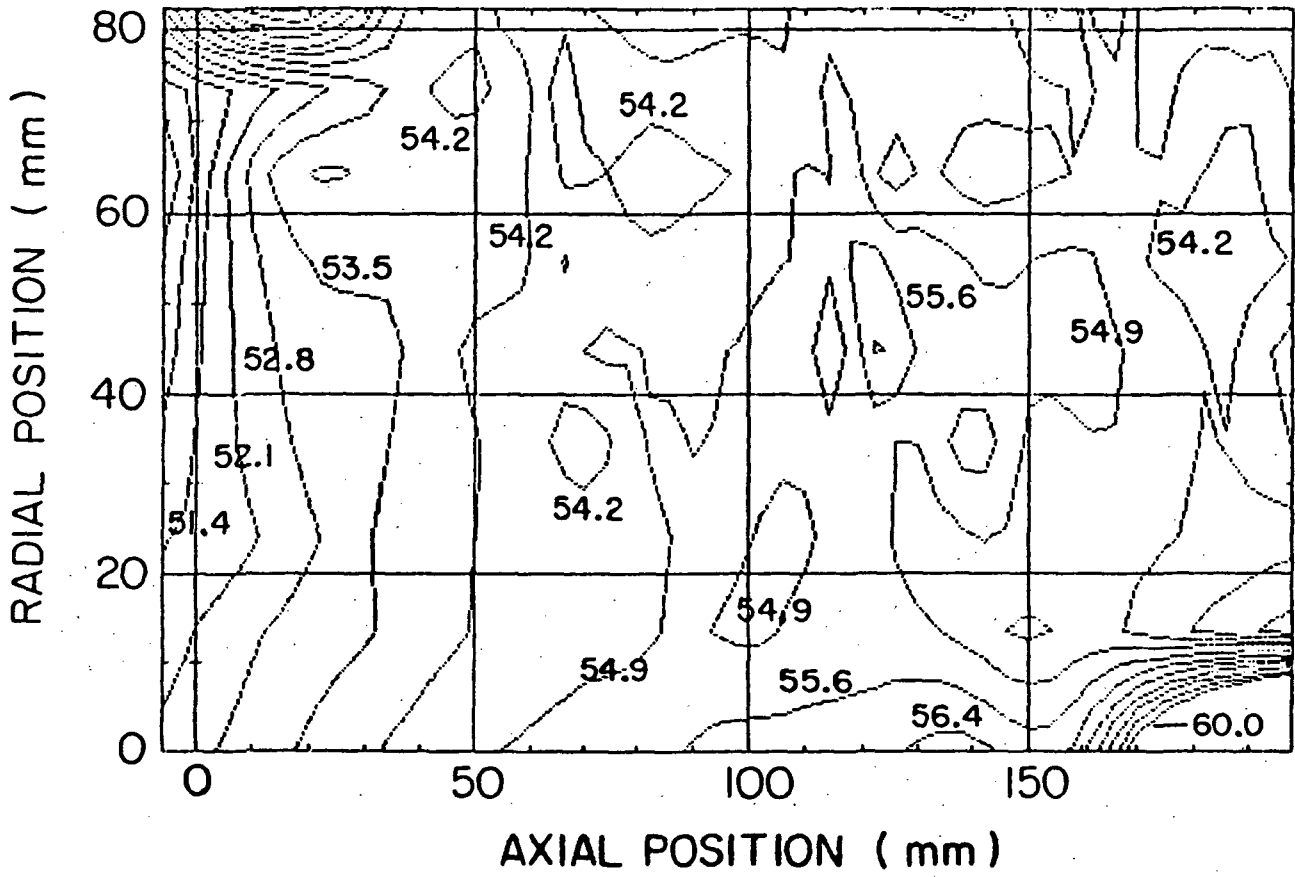


Fig. 2.9

Contour plot of the plasma potential in the ring cusp case.

PLASMA DENSITY

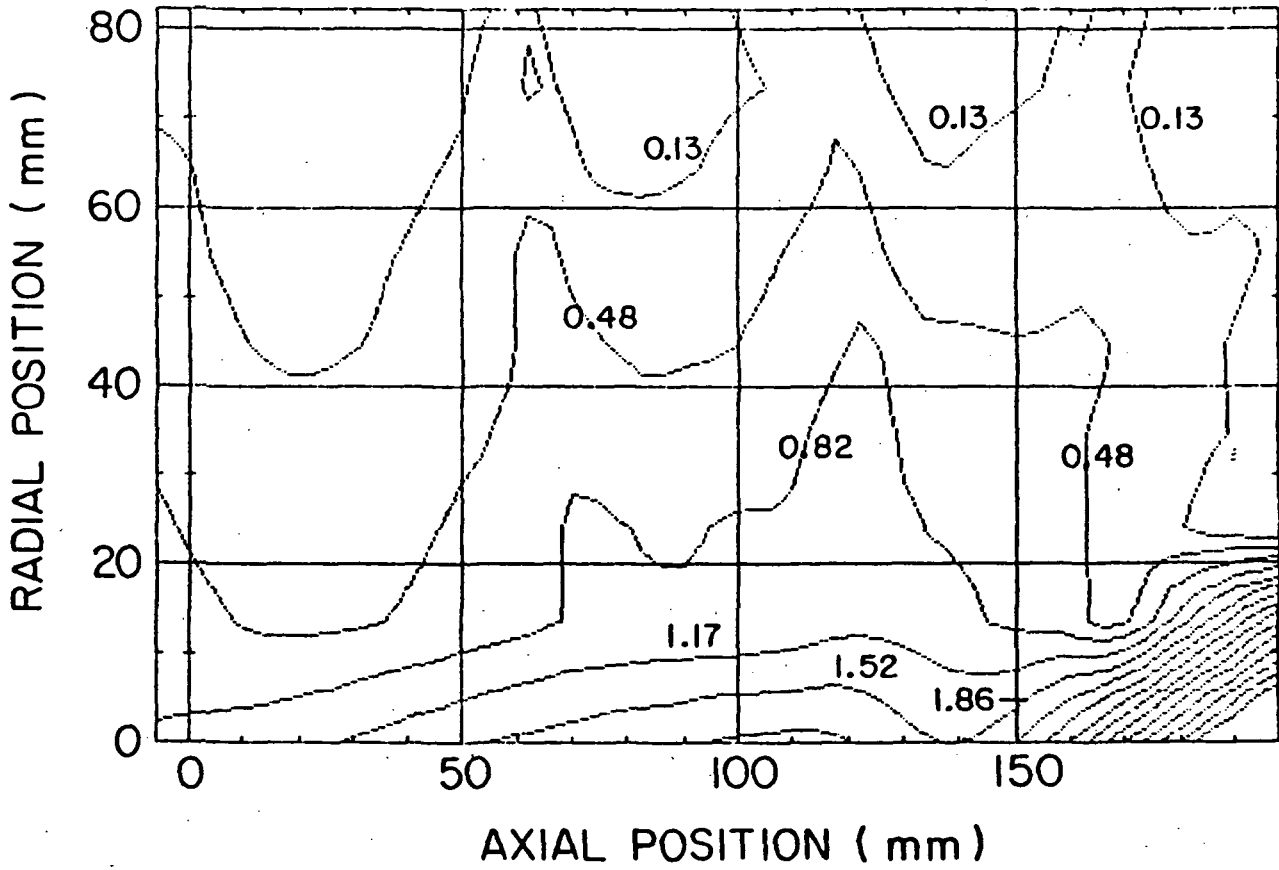


Fig. 2.10 Contour plot of the plasma density in the ring cusp case.

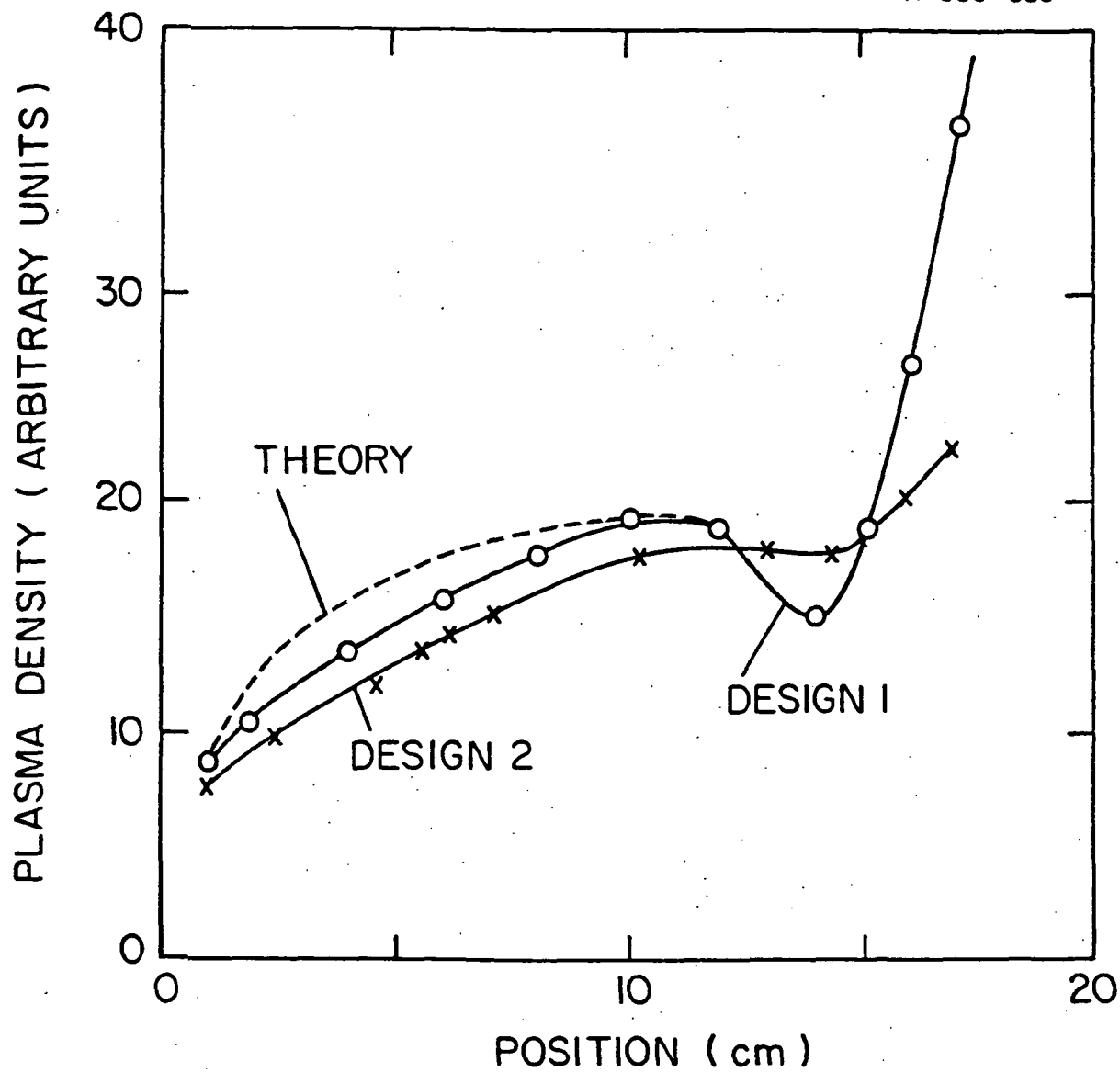


Fig. 2.11 Axial variation of the plasma density in the ring cusp case.

FIELD CONNECTION BETWEEN CATHODE AND GRID

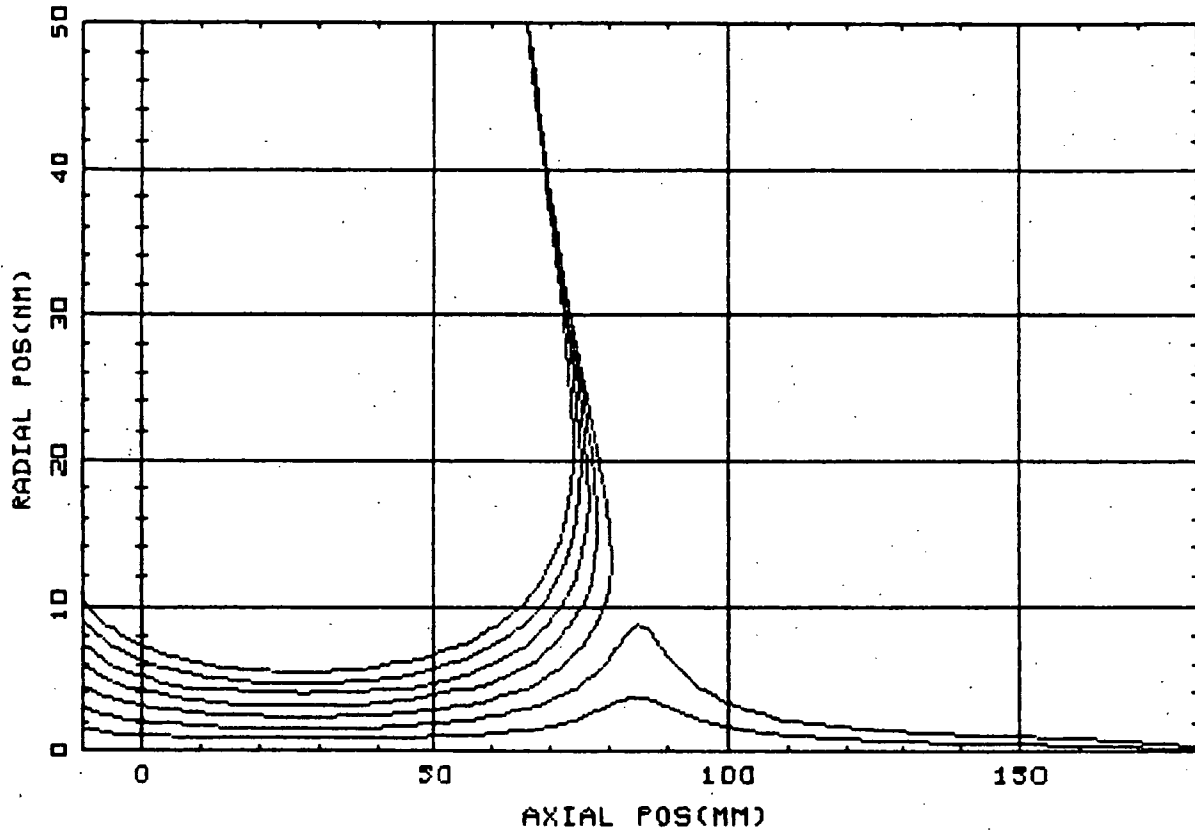


Fig. 2.12 Magnetic field near the axis of the thruster for the ring cusp case in arrangement number 1. The lines show the calculated directions of the magnetic field. The density of lines has absolutely no meaning. Note that only two of the lines which pass through the extraction grid connect to the cathode.

FIELD CONNECTION BETWEEN CATHODE AND GRID

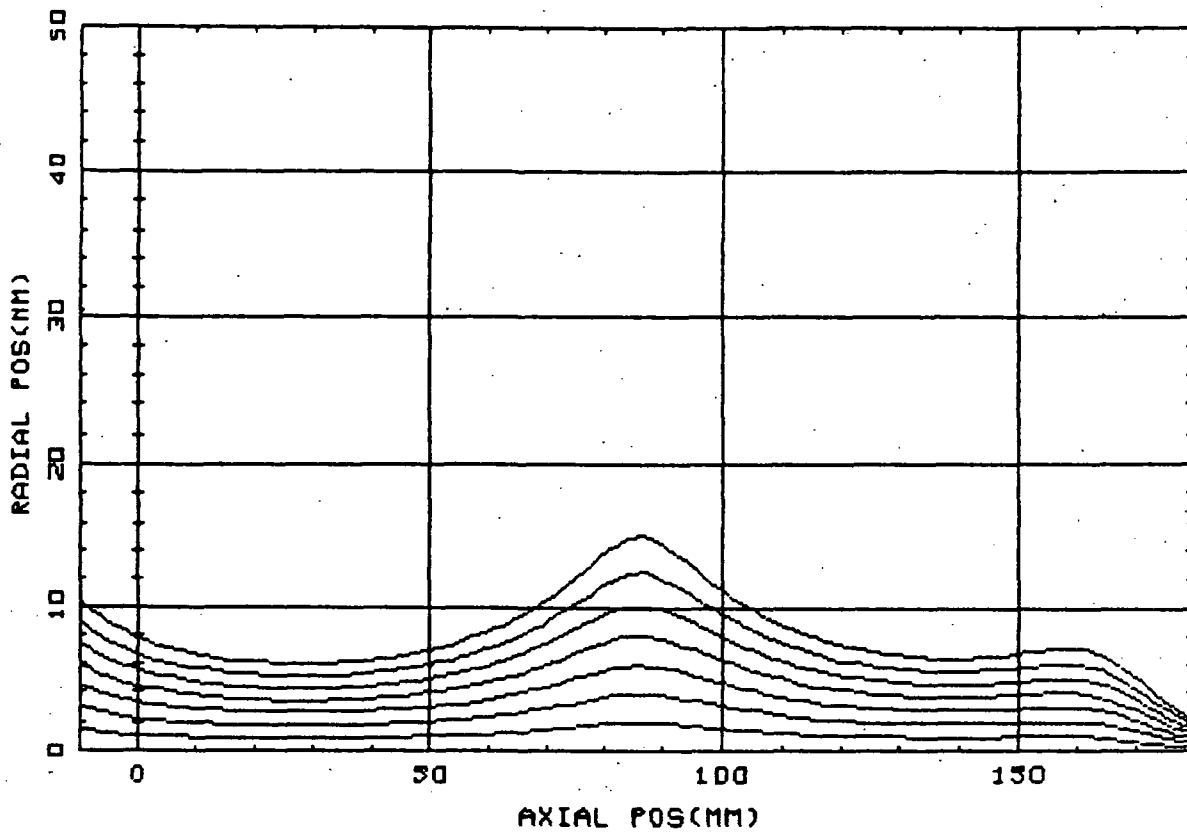


Fig. 2.13 Same as Fig. 2.12 except for arrangement number 2. Note the increase in the number of magnetic field lines that connect the cathode and the extraction grid.

ELECTRON TEMPERATURE

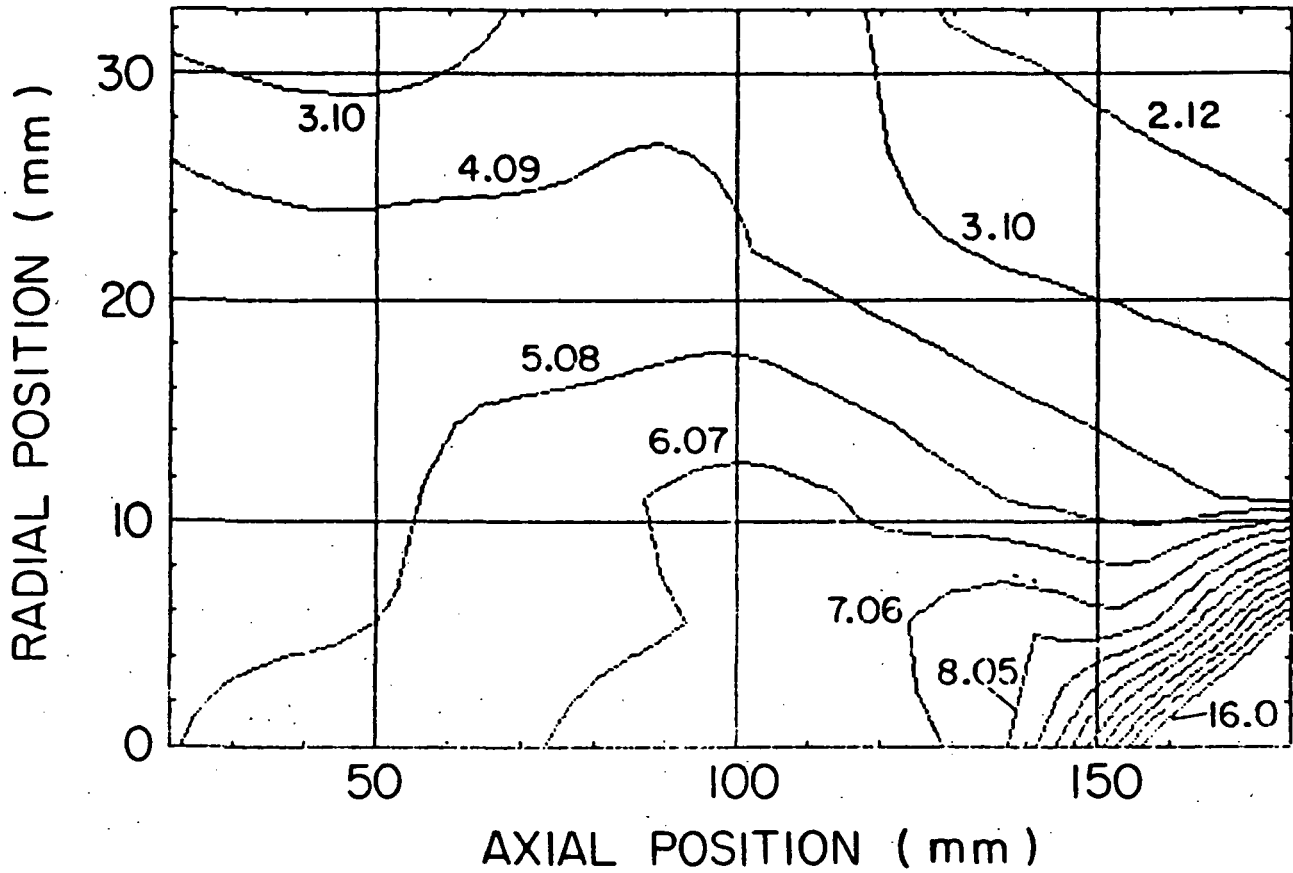


Fig. 2.14 Contour plot of the electron temperature for the ring cusp case in arrangement number 2.

PLASMA POTENTIAL

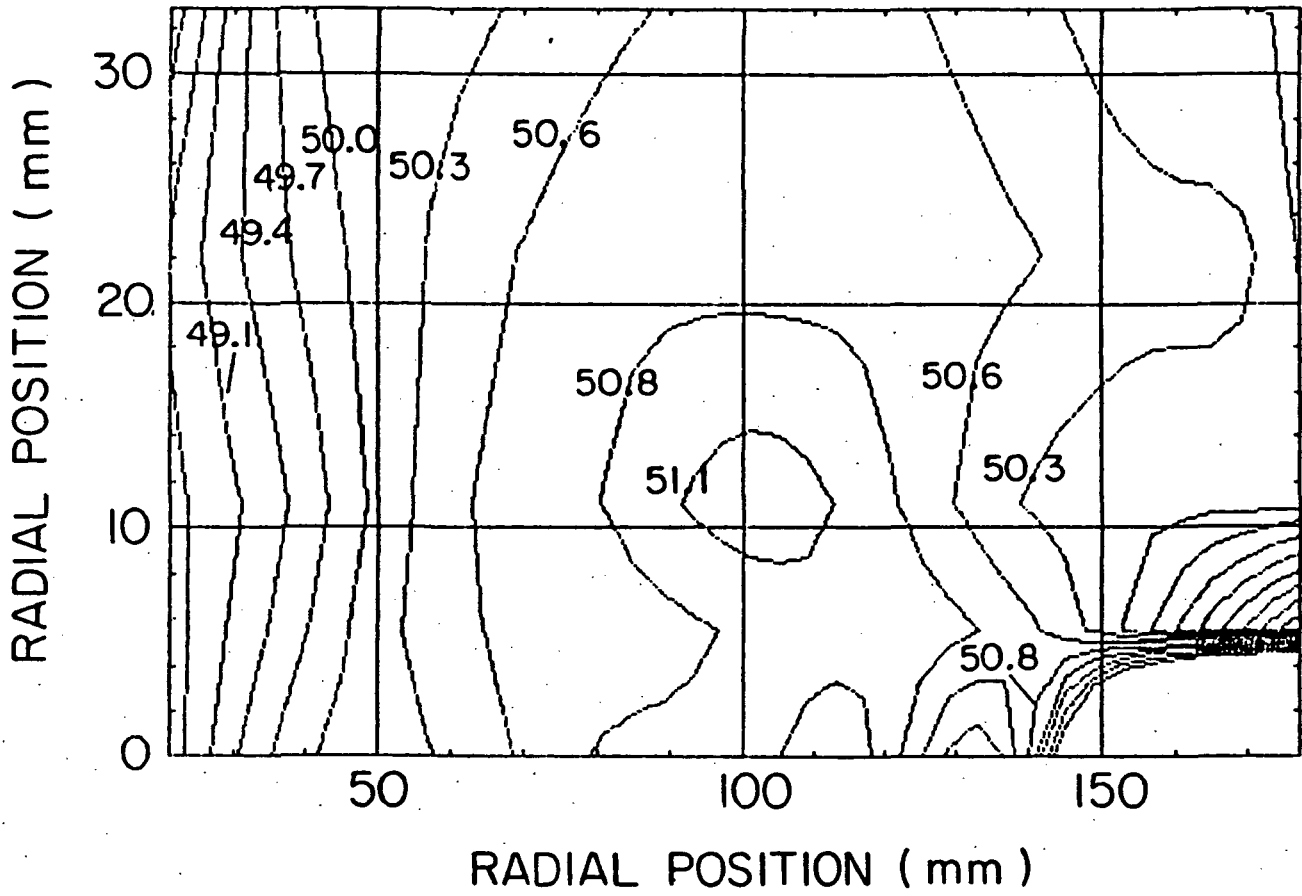


Fig. 2.15 Contour plot of the plasma potential for the ring cusp case in arrangement number 2.

PLASMA DENSITY

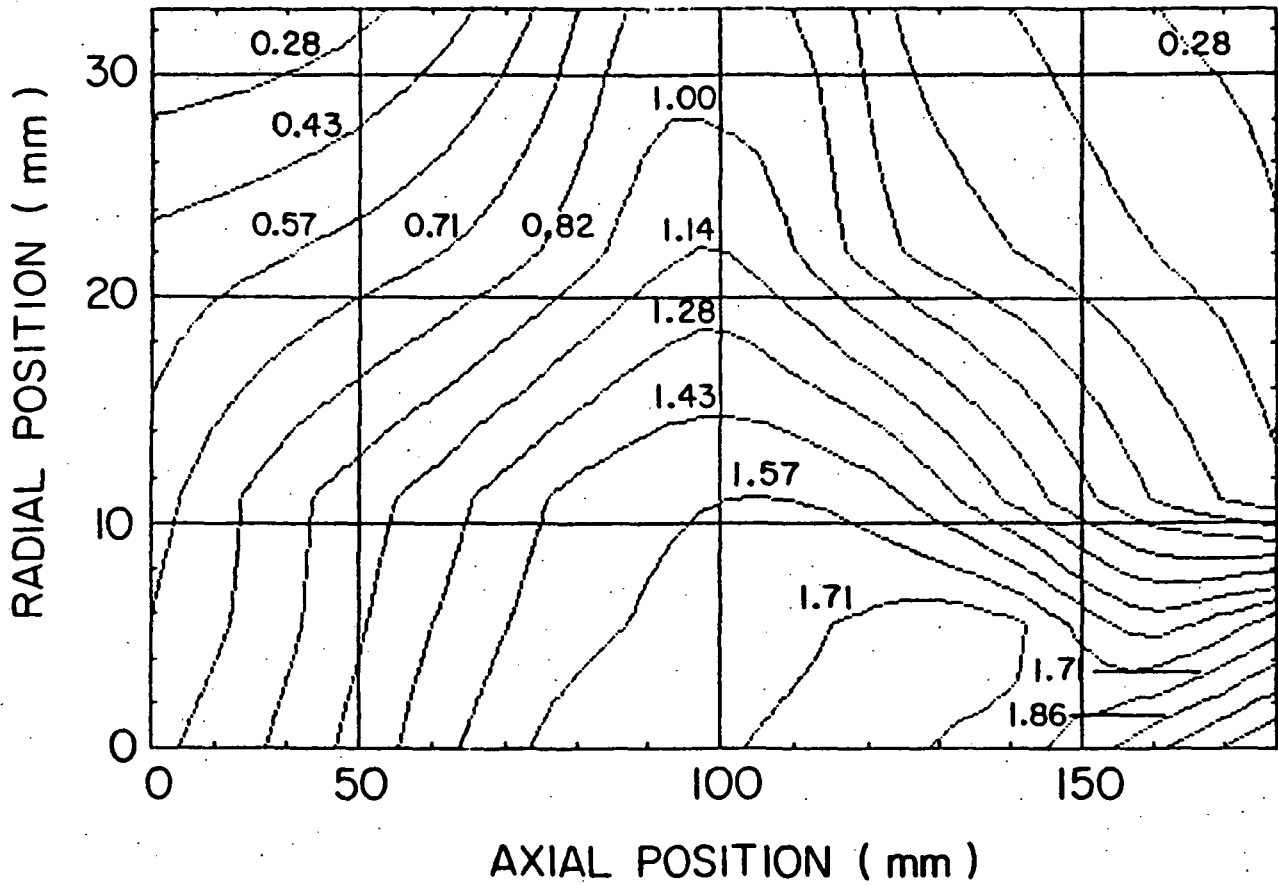


Fig. 2.16 Contour plot of the plasma density for the ring cusp case in arrangement number 2.

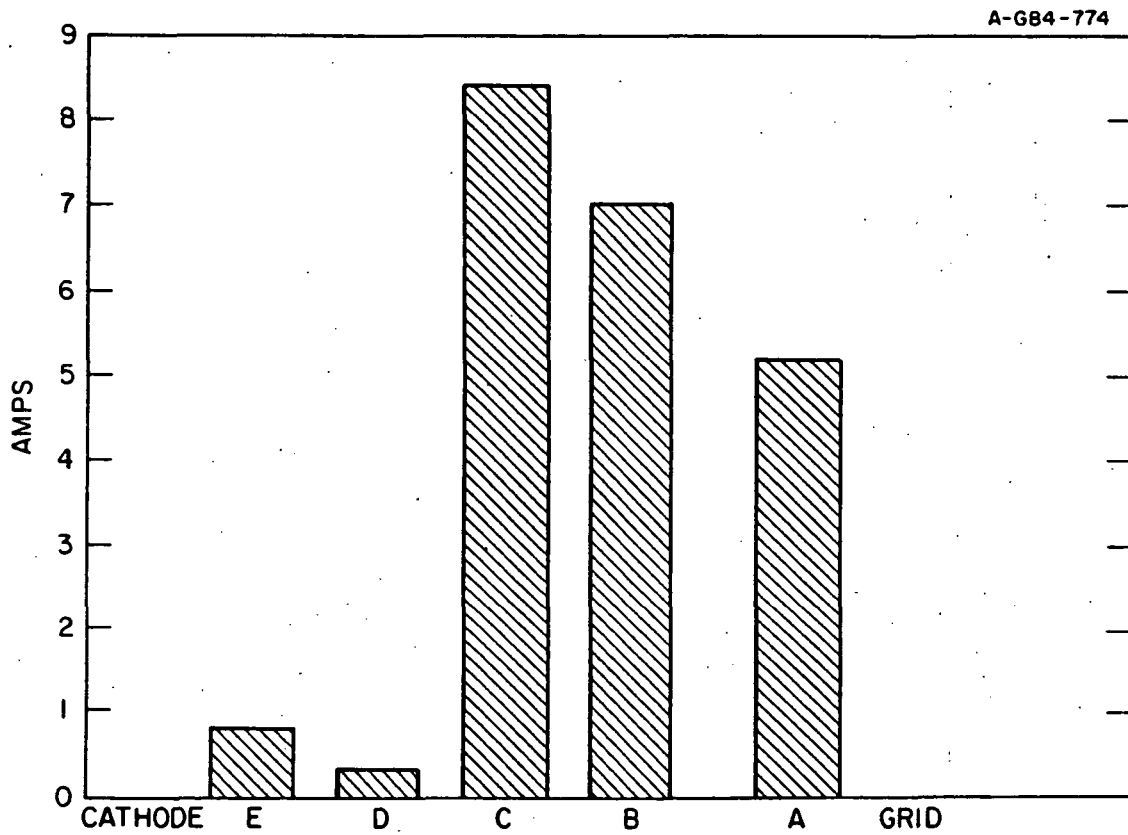


Fig. 2.17 Electron loss currents to the cusps in the ring cusp case, arrangement number 1. There were no electron currents to the cathode or to the extraction grid. The letters defining the cusps refer to the same locations as shown in Fig. 3.2.

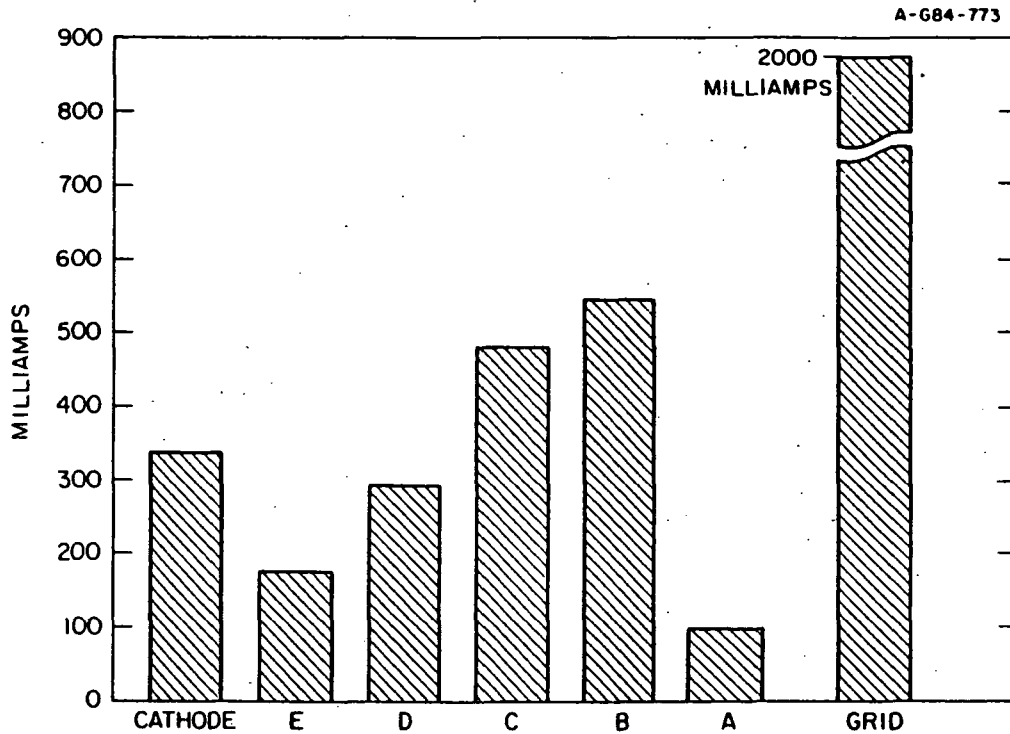


Fig. 2.18 Ion loss currents to the cusps and cathode in the ring cusp case, arrangement number 1. The letters defining the cusps refer to the same locations as shown in Fig. 3.2.

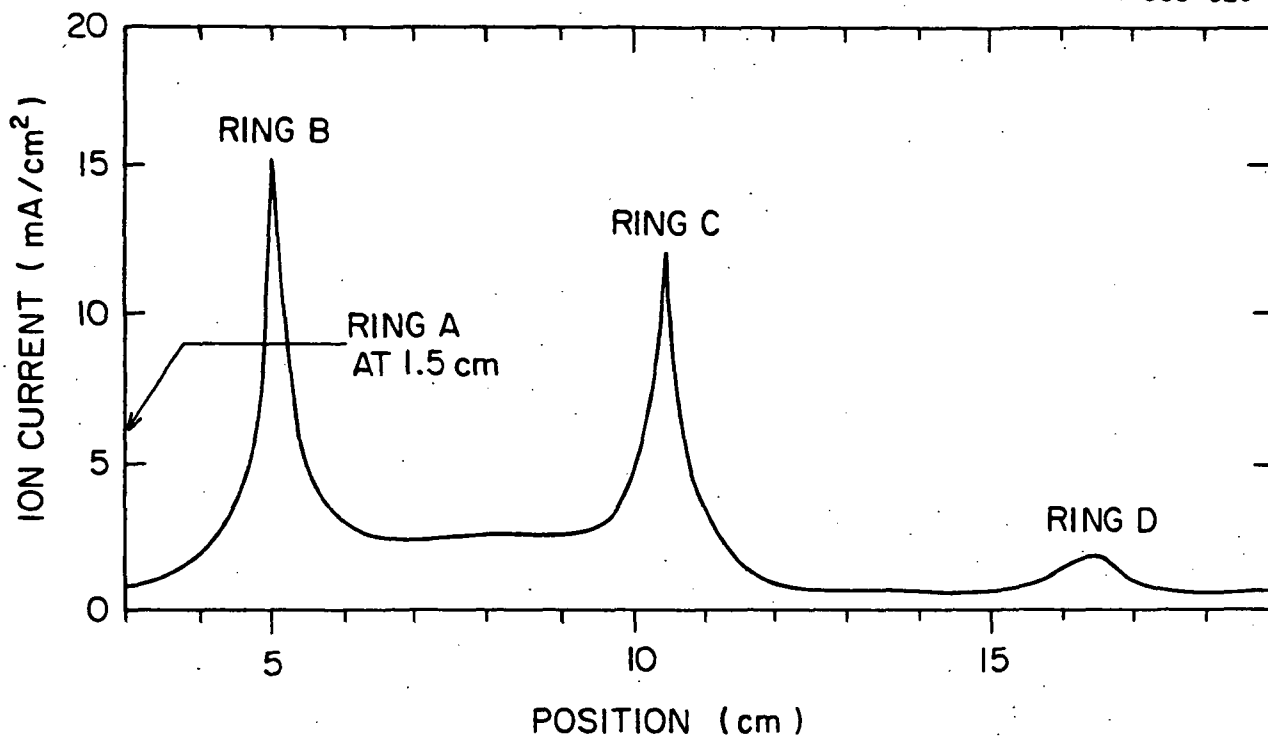


Fig. 2.19 Ion loss currents to a thin movable strip in the ring cusp case, arrangement number 2. The letters defining the cusps refer to the same locations as shown in Fig. 3.2.

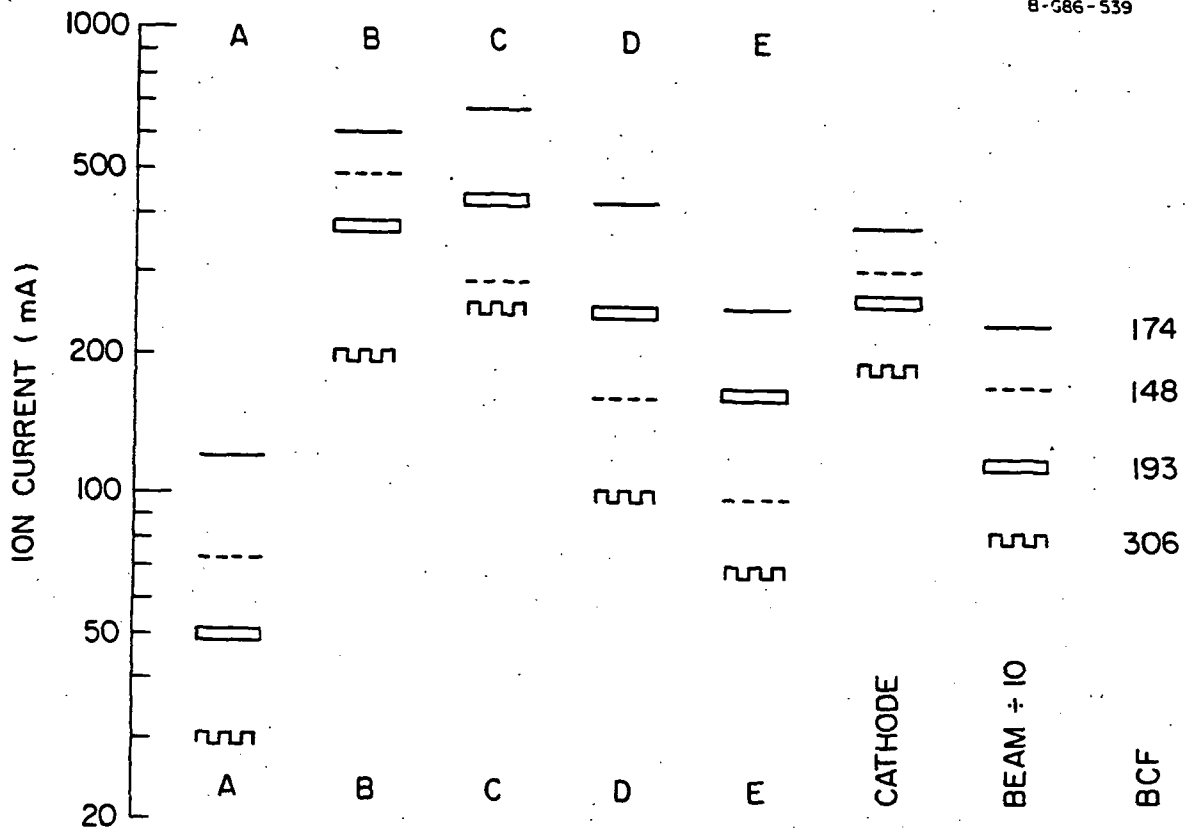


Fig. 2.20 Representative ion currents in the ring cusp case, arrangement number 2, for several operating conditions. The letters defining the cusps refer to the same locations as shown in Fig. 3.2.

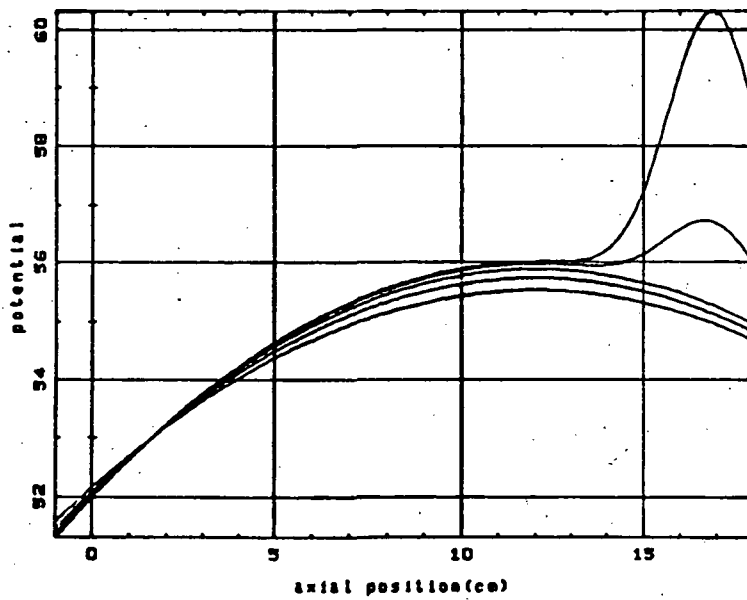
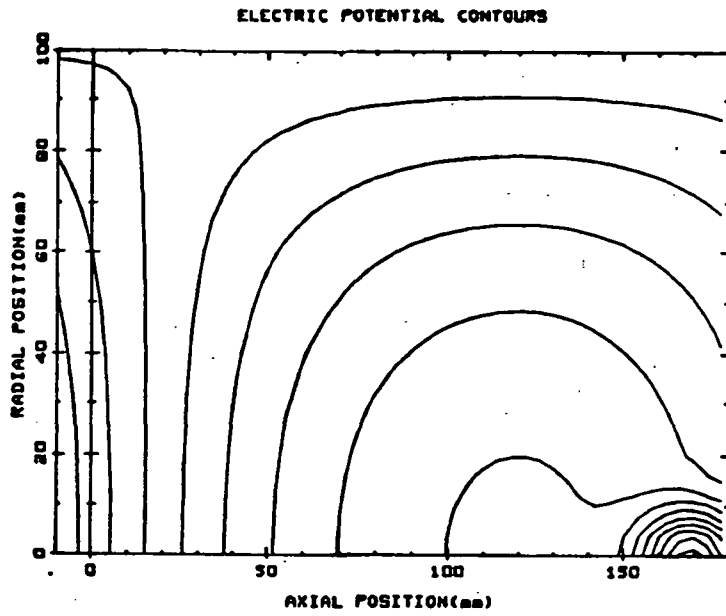


Fig. 3.1 Analytic function used to approximate the potential in order to calculate ion orbits.

ORIGINAL PAGE IS
OF POOR QUALITY

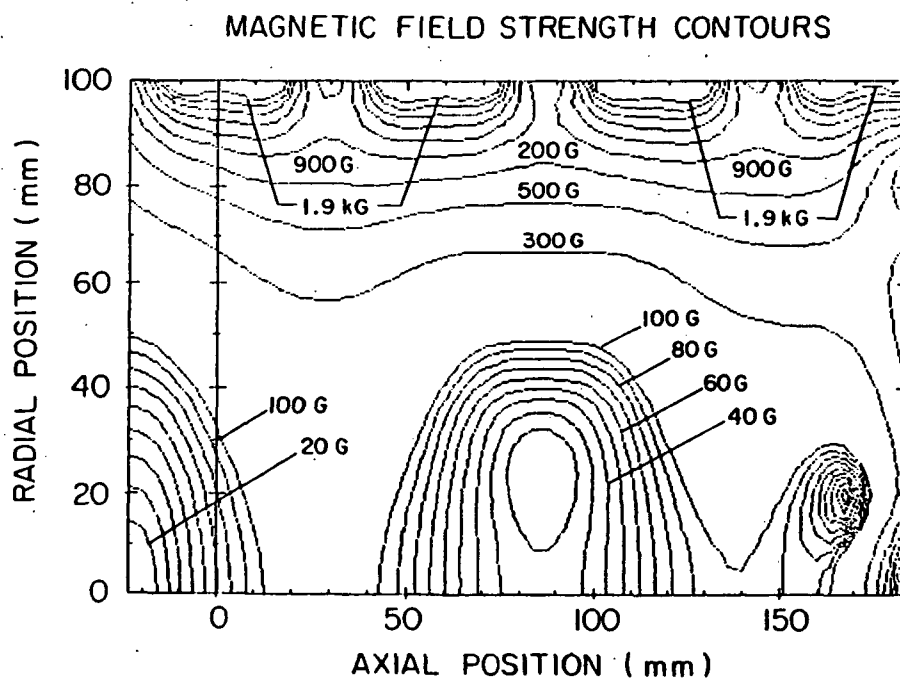
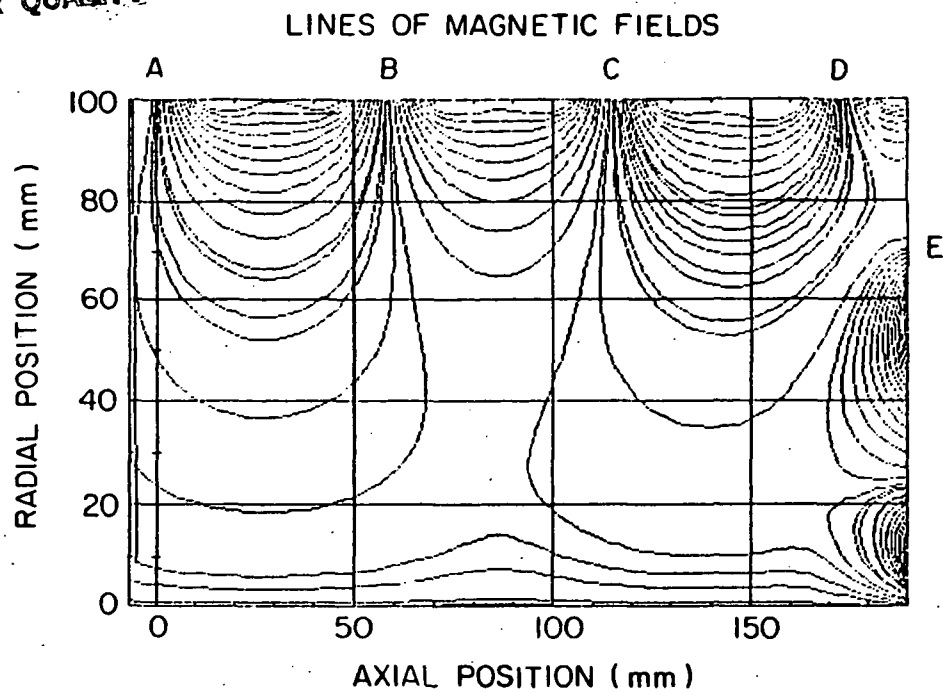


Fig. 3.2

Calculated magnetic field used in the orbit calculations.

ORIGINAL PAGE IS
OF POOR QUALITY

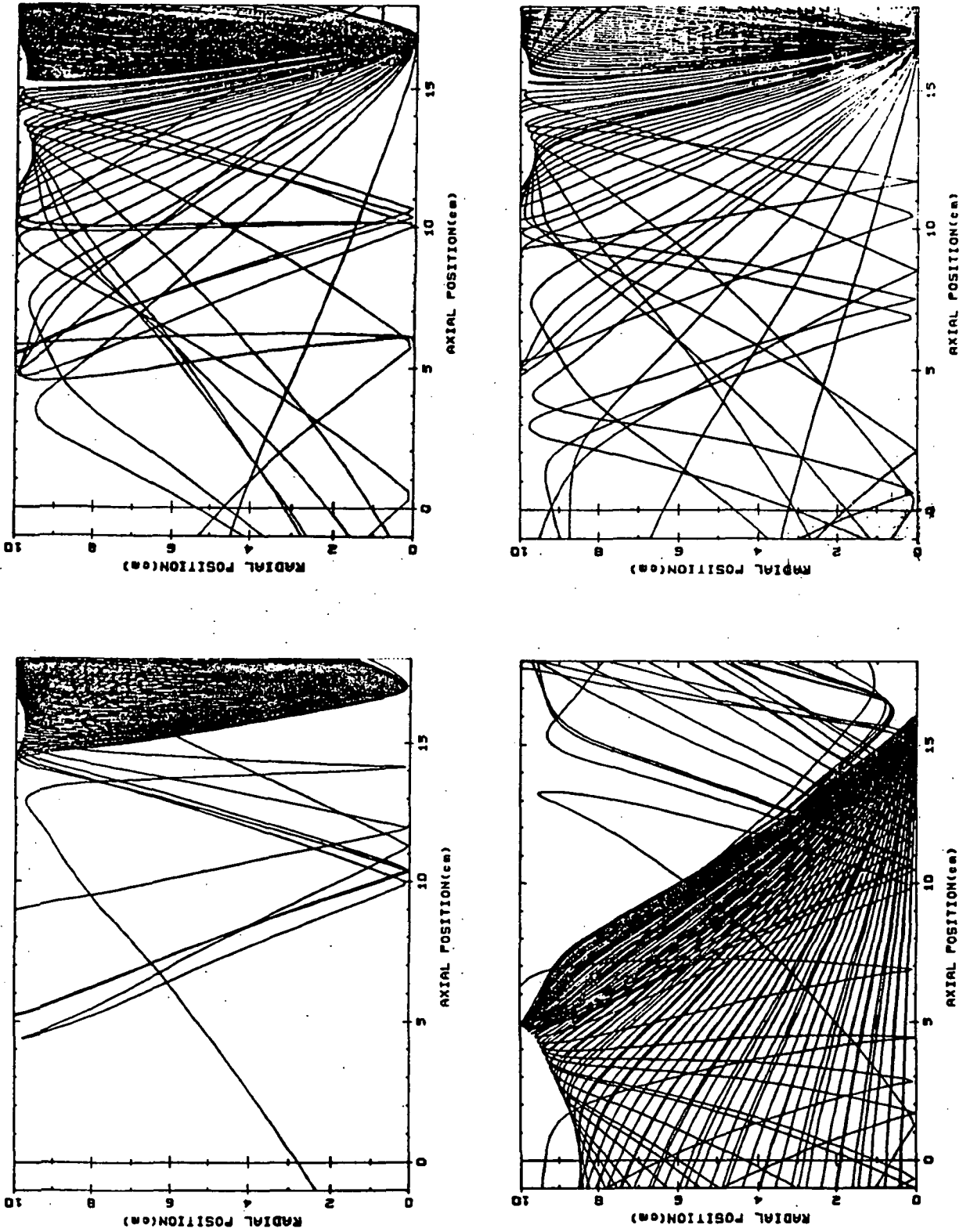


Fig. 3.3 Ion orbits for ions born with an energy of 0.1 eV. In each figure there are 91 orbits corresponding to initial directions from 0 to 180 degrees in 2 degree steps. The four figures correspond to four different starting points. See text for details.

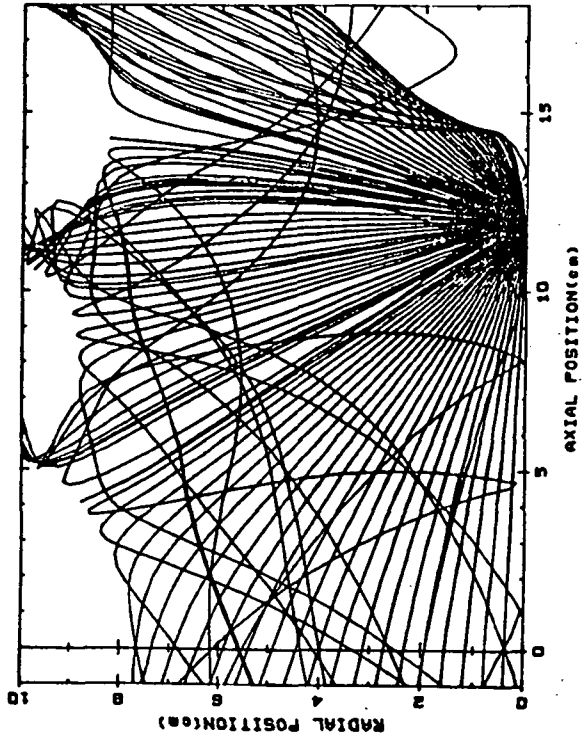
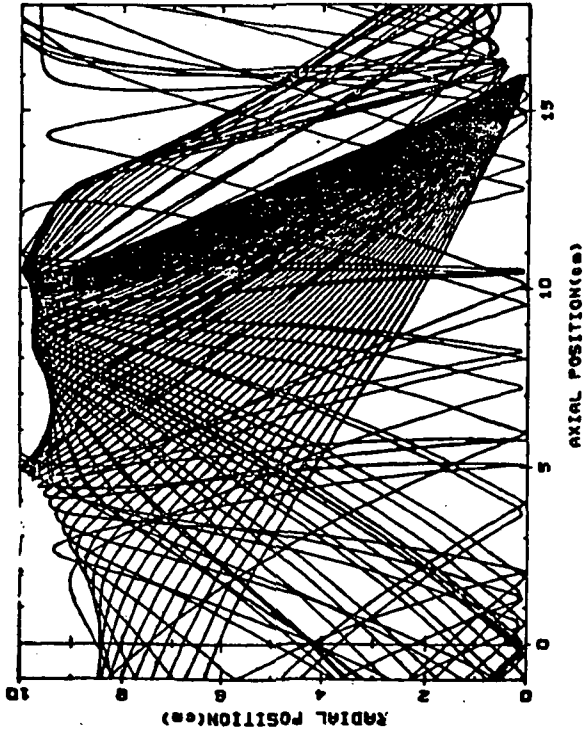
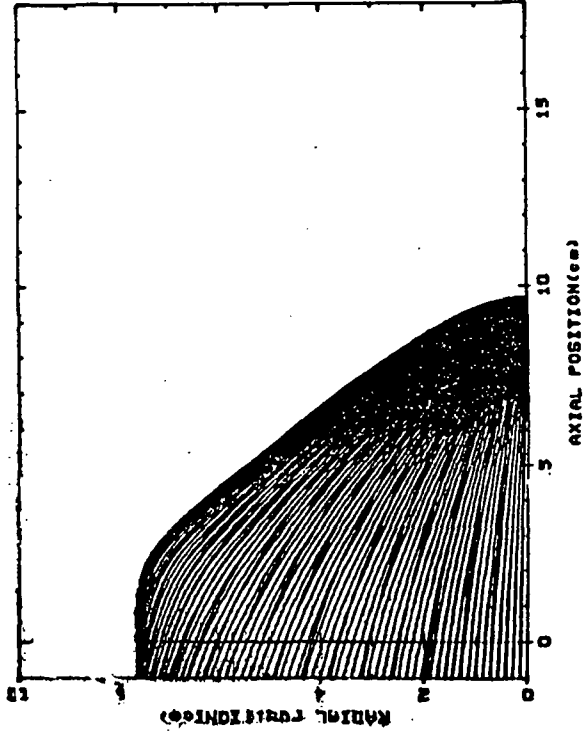
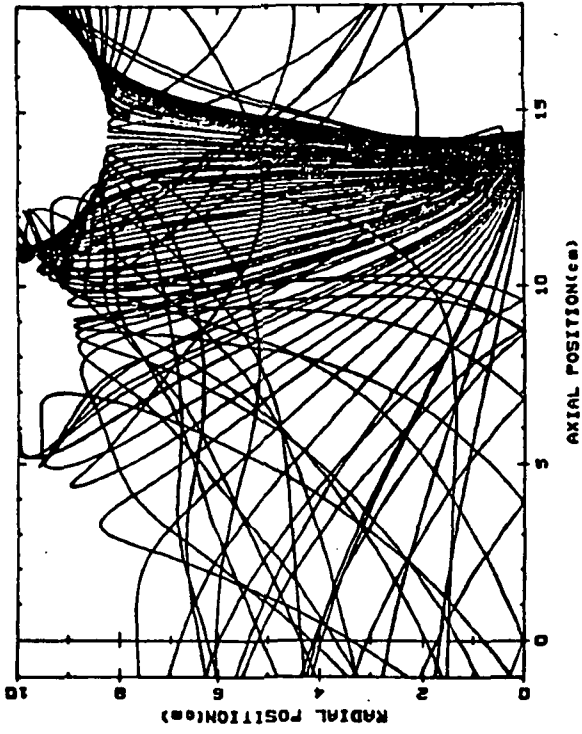


Fig. 3.4 Same as Fig. 3.3 for four other starting points.

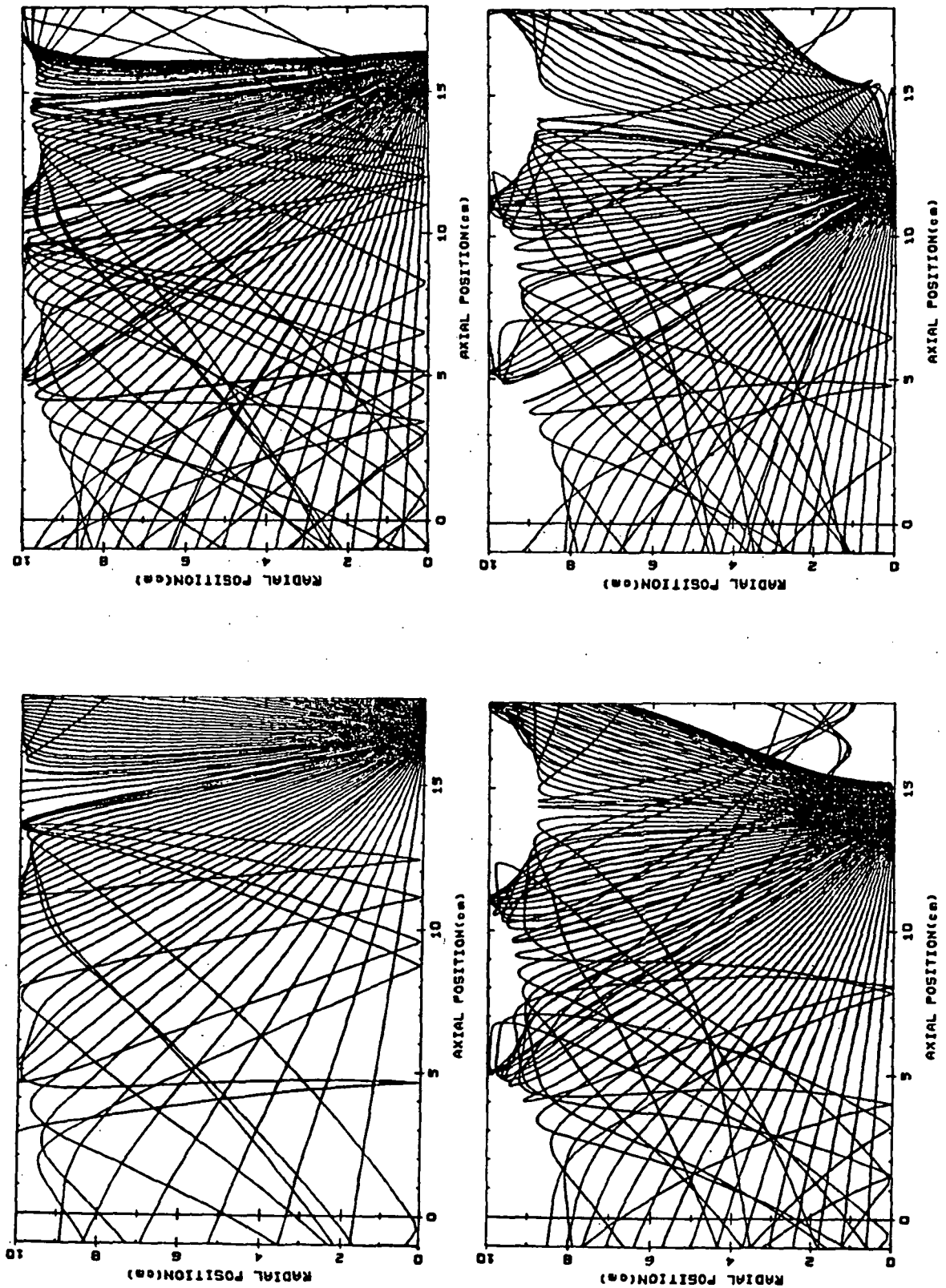


Fig. 3.5 Same as Fig. 3.3 except the initial ion energy is 0.4 eV.

ORIGINAL PAGE IS
OF POOR QUALITY

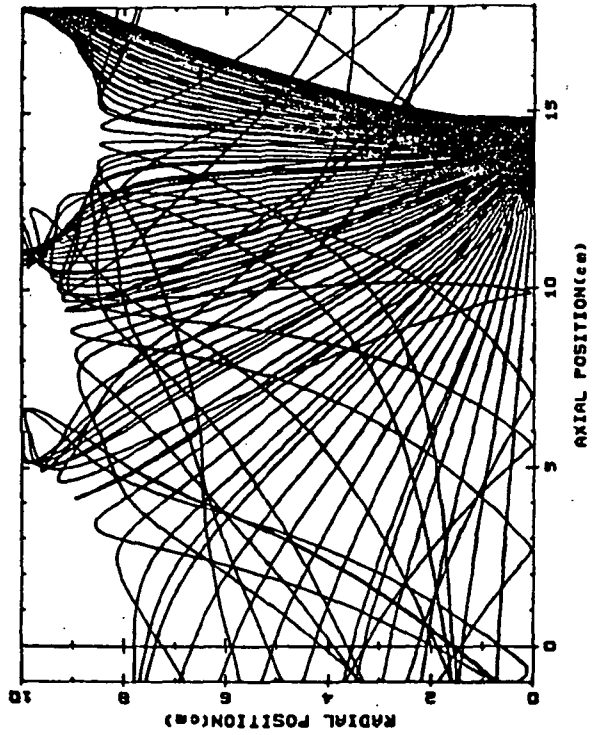
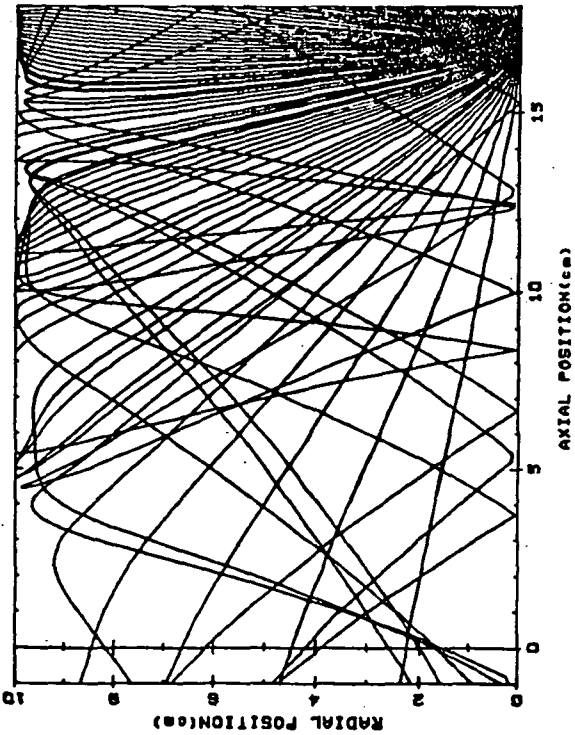
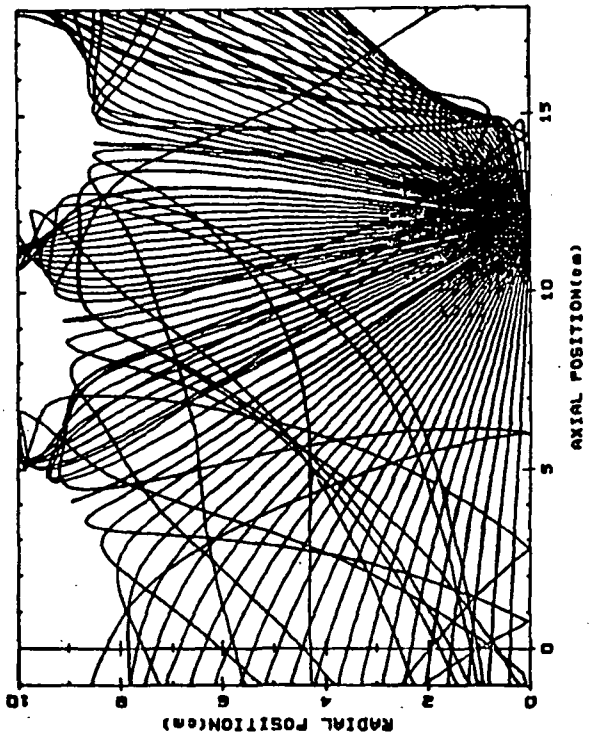
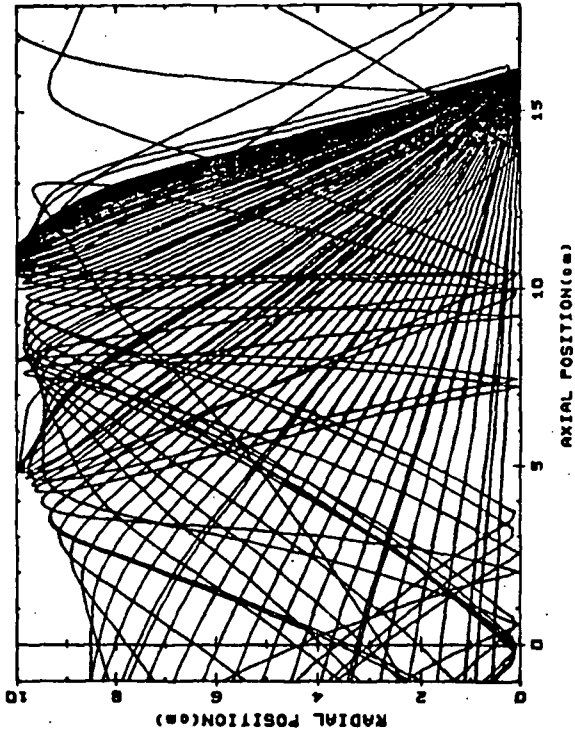


Fig. 3.6 Same as Fig. 3.3 except the initial ion energy is 1.0 eV.

APPENDIX

This appendix consists of chapters 3, 4 and 5 of the Master's thesis of Mr. Scott Boardsen together with all of the figures and tables of that work. It will be recognized that this Final Report has borrowed heavily from the figures in the thesis and that there are several duplications. The principle justification for including this appendix is that certain details are treated in the thesis that were otherwise omitted from this report. In particular, the Tables and the discussion that goes with them have considerable technical interest as an introduction to some quantitative aspects of the thruster. Also the data-taking program and the magnetic field calculations are more fully discussed. Further, it is felt that the discussion, while speculative, is provocative and therefore potentially useful.

CHAPTER III
EXPERIMENTAL METHODS

Langmuir (collecting) probes were used to measure plasma density and potential and electron temperature. Loss fluxes to various surfaces were determined by measuring the currents to foils attached to or imbedded in the surface in question. The Langmuir probe data were acquired using a microcomputer to generate the probe sweep and to store the resulting digitized probe current. The loss currents were determined from current vs voltage (I-V) characteristics observed on a Tektronix type 575 "transistor curve tracer" oscilloscope.

Probe Measurements

A schematic of the probe data system is shown in Fig. 7. The computer outputs a 256 step ramp. Each step is 0.02 volts, which is amplified by a factor of ten, yielding a 50 volt ramp. The computer requires 11 msec per ramp with a 8 msec waiting period after each ramp. Each ramp consists of 256 output points and reading 256 data points. Each trace that is recorded is averaged over 10 cycles. Each trace is stored in a 1 by 256 point array. There is a linear relationship between array location and voltage applied to the probe whose array value corresponds linearly to the current drawn at that corresponding voltage. The stored traces are transferred to a minicomputer where they are analyzed.

The Langmuir probe was cylindrical in nature consisting of the exposed tip of 10 mil tungsten wire, whose surface area ranged from 0.012 to 0.02 cm², collecting no more than 80 milliamps at any time. Due to the small Debye lengths of approximately 2×10^{-3} cm compared to a probe radius of 2.5×10^{-2} cm a planar Langmuir probe theory is used in the analysis. The data analysis is described in Appendix B.

The interior of the device was mapped out by cutting a horizontal slit in the extraction grid through which a Langmuir probe was inserted, whose exposed end was at the tip of an elbowed insulating rod. The insulating rod was lined up with the device axis and could move back and forth in that direction. The probe also had horizontal motion along the slit and could be rotated about the axial direction. This allowed access to any point inside the ion thruster.

Due to the aximuthal symmetry of the ring cusp configuration, data was taken in axial rows for various radial positions whose range swept out the device. The probe was moved in 1 cm steps between data points except in regions with large density gradients where smaller steps were taken. Programs were constructed that computed various volume intervals of some function of the plasma parameters. The integrals were computed by fitting the data with cubic splines in the axial direction and with linear interpolation in the radial direction.

Loss Current Measurements

In the ring cusp configuration the measurement of the total current to a given surface was just the reading of an ammeter connected

between a foil on the magnet surface and the anode surface. The location and size of these probes are shown in Figs. 8 and 9. To separate this into electron and ion components, and to correct for voltage drops in the measuring circuit, it is necessary to obtain an I-V characteristic for the foil. At high positive bias, relative to the surface, electron saturation current is drawn. The curve is not horizontal, however, due to IR drops and expansion of the sheath around the foil. Therefore, the straight, but sloped, line was extrapolated to zero bias (the point where the foil was at wall potential) to obtain the electron current to the wall, this was done in the line cusp configuration. The ion current was similarly obtained by extrapolating the negatively biased saturation curve back to the wall potential. Some error due to the slight geometric distortion produced by the foils (Fig. 9) could not easily be avoided. In one case, the foils were embedded in holes drilled into the iron pole faces used in the line cusp configuration. This prevented the foils from extending into the plasma, but instead distorted the magnetic field somewhat. From these measurements, plus the extraction grid currents, the total ion production rate can be determined.

CHAPTER IV
EXPERIMENTAL RESULTS

Line Cusp Configuration

The line cusp configuration was mapped out by measuring its plasma characteristics. The results are discussed in an earlier paper.⁸ A summary of the results will be given. The line cusp configuration consists of 18 rows of samarium cobalt magnets, each row alternating in polarity. This type of configuration tends to push the magnetic fields away from its axis toward the anode walls. The field strength in the central axial region is negligible and only has a significant effect within 3 cm of the anode wall. For a given radial profile the density profile has little variation until the probe is in the cusp region near the anode, as shown in Figs. 10 and 11, for two different operating conditions. The potential profiles follow the density profiles but with a smaller variation. The low central field strength allows the electrons to mix readily and the electron temperature is constant to within experimental uncertainties throughout most of the device, except in the cusp regions.

The possible presence of positive potential islands existing between the cusps was investigated which have been observed⁸ in similar multicusp plasmas. A detailed map of the plasma characteristics between the cusp regions was made in the middle of the device. Figs.

12-14 are contour maps of electron temperature, plasma potential, and plasma density. They show decreasing density, decreasing temperatures, and positive potential islands when moving from the device center toward the anode. The decreasing density is due to the magnetic confinement and slow diffusion rates across field lines. The decreasing electron temperature is due to the cooling of plasma electrons due to neutral particle collisions. Since the ion temperature is very low (< 0.1 eV), the potential islands play a role in channeling the ions into the cusps. This decreases the ion loss width, leading to better confinement.

Ring Cusp Configuration Design 1

Unlike the line cusp configuration, which has a field free central region, the central region in the ring cusp configuration has fields large enough to effect the electron motion. Therefore, in this case, the constant radial dependence of plasma density and electron temperature observed in the line cusp configuration is not observed in the ring cusp configuration.

Fig. 15 is a contour map of the field configuration for ring cusp design 1, which consists of 5 magnet rings of alternating polarity. The fifth ring lies on the endplate and is of opposite polarity with the cathode magnet. Fig. 16 is a plot of magnetic field lines that indicate the field direction. Fig. 17 shows the seven distinct flux regions into which the field lines are separated. The confinement strength of each region is related to the magnetic flux contained in that region.

To get an idea of the important physical processes going on in the main body of the thruster, a detailed picture of the thruster operation will be drawn for one parameter setting. This setting is close to the maximum efficiency for this particular configuration called design 1. Table 4 gives the external parameter readings.

Figures 18, 19, and 20 are axial graphs for electron temperature, plasma potential, and plasma density at radial position equaling 0.0 mm. Figure 21 gives a better idea of axial plasma potential including the cathode and grid. The graphs show that electron temperature, plasma density and plasma potential all vary when approaching the orifice (axial position = 180 mm). The high plasma potential could indicate high plasma production given the large electron temperatures and their large mobilities. High plasma density and electron temperature also indicate large ion production.

Figures 22, 23, and 24 are contour maps of the electron temperature, plasma potential, and plasma density, respectively. Notice that the electron temperature and density contours have a tendency to follow the field lines which is expected since the collisional mean free paths are longer than the device length. Also notice the enhanced penetration of the electron temperature contours in the region of magnetic ring C compared to the penetration into the region of magnetic ring B. This suggests that a large portion of the power emitted from the cathode orifice ends up in region 1.

Figures 25 and 26 show the electron and ion currents to the magnetic poles, cathode, and grid. A large proportion of the discharge

current tends to go to pole C. Minimizing the fraction of discharge current to pole C would probably lead to higher efficiencies.

Figures 16 and 17 indicate why the efficiency is poor for this configuration. Region 2 is weak and narrow near the orifice, while the field structure in Region 1 strongly links the cathode orifice with the anode. To get better efficiencies for the ring cusp configuration, Region 2 must be enhanced, weakening the coupling with pole C. With this idea a new design was tested which amounted to switching the polarity on magnet ring E. In design 2, Region 2 is larger in diameter when compared to design 1 as shown in Figs. 27 and 28. The best efficiencies were achieved in this configuration when compared to the line cusp configurations tested and other ring cusp configurations.

Ring Cusp Design 2

Figures 5 and 6 are magnetic field strength and direction plots, respectively, for ring cusp design 2. Note the enhanced axial field region connecting the cathode orifice with the extraction grid. Table 4 gives the external parameters close to maximum efficiency for design 2 which was mapped out.

Figures 29-31 are contour plots of electron temperature, plasma potential, and plasma density, respectively. Note that the electron temperature and plasma density contours are different compared to those of design 1. The high temperature lobular arm extending toward pole C present in design 1 is no longer present in design 2, which indicates that the magnetic coupling between the cathode and pole C has been significantly weakened.

Figures 32 and 33 are BCF curves for design 1 and design 2. Design 2 is much more efficient than design 1 or the line cusp configuration. Enhancing the number of field lines that connect the orifice, or regions near the orifice, with the grid seems to be an important factor in reducing the BCF. Enhancing this linkage in the line cusp configuration is difficult because there are many poles on the anode close to the cathode and of opposite polarity that provide a strong magnetic coupling between the cathode and anode. Therefore, the ring cusp configuration appears to be an inherently better design.

Ring Cusp Calculations

Table 5 gives the values of various volume integrals of physical quantities averaged over the chamber volume for both design 1 and design 2. In regions of the device with temperatures above 17 eV those temperatures were truncated to 17 eV because temperatures above the primary electron energy seem physically unobtainable. The ion production rate, due to Maxwellian electrons, was calculated by performing a volume integral throughout the thruster. The neutral density inside the device must be known to make this calculation and other similar calculations. The neutral density was determined by mounting an ionization gauge on the thruster endplate. The neutral density is given in Table 4. Near the endplate* cathode the plasma density is 30% of the neutral density. It was assumed that the plasma density, plus the neutral density is constant. This might not be a good assumption. Under the above assumptions, thermal ionization accounts for roughly 10 to 30% of the total ion production.

Beam-Plasma Observations

Probing the area around the cathode orifice using an Tektronix type 575 "curve tracer" oscilloscope indicates the presence of a very turbulent lobular region of 3-5 cm in size projecting from the cathode orifice. In this region large amplitude low frequency noise in the range of 8 KHz to within a factor of 10 was observed. The amplitude of this noise falls off rapidly as the probe is moved away from the orifice. Figures 34-37 are Langmuir traces. Their corresponding fits are taken on the device axis in thruster design 1. Although not shown in the figures, the base line is flat. Figure 34 is nearest to the orifice; roughly 1 cm away, while Fig. 37 is the furthest. Figure 34 has the shape characteristic of a primary beam (although the indicated energy is about a factor of 2 too large), which is rapidly thermalized as it moves away from the cathode orifice (Figs. 35-37). If the above interpretation is correct, the primary electron beam is damped away within 4 cm of the cathode orifice.

The power input into the thruster main body by the primary beam can be estimated from the observation that the external current to the cathode exterior is, in most cases, less than 1 amp. This means that

*Two pressure gauges were used. One was mounted on the thruster and the other was downstream of the thruster. The flow meter and downstream gauge give no indication of a change in flow rate after device ignition, which is not surprising since most of the flow impedance is due to the gas feed tubing. But the thruster mounted gauge indicates a pressure drop after ignition. This is probably because a large proportion of argon atoms are pumped from the thruster as ions.

the primary current is roughly equal to the discharge current. Therefore, the power input is

$$P_I \sim I_d \times \Phi_E \quad . \quad (4)$$

One would expect that the primaries are initially directed along the magnetic field lines as they leave the orifice. The lines of magnetic fields in all configurations diverge slowly at the orifice and range between 0.5 and 1.0 kG, depending upon the configuration. The initial primary density can be estimated knowing the area of the orifice A_0 , the primary energy E_p , and I_D . In Table 6 the calculation is made giving an initial value of primary beam density n_B of 10^{14} cm^{-3} .

Initially, a dense energetic primary beam is impinging on the main body plasma which has a much lower density $n_p \sim 4 \times 10^{12} \text{ cm}^{-3}$. Instabilities and radial electric fields could lead to a substantial spreading of the beam downstream of the orifice. There are two important factors that must be understood in the beam-plasma interaction. 1) How the beam yields its energy to the plasma leading to damping and thermalization of beam particles, and 2) The role beam primaries play in ion production by direct ionization.

It is observed that these processes occur within a very turbulent lobular region emanating from the cathode orifice of roughly 3 to 5 cm in size. Outside this region the plasma appears to be close

to Maxwellian in nature with little evidence of the existence of a primary beam.

There are two processes that contribute to the damping of the primary beam. 1) Damping due to binary collision between primaries and other particles, and 2) Collective interactions between the beam and the plasma leads to strong damping.

Table 7 gives collision cross sections, collision frequencies and mean free paths for various binary collisions between a 17 eV primary and another particle. Collisions within the beam and elastic neutral or ion particle collisions do not change the primary energy but produce scattered primaries which are capable of producing ions in single step processes. All other types of collisions lead to the rapid thermalization of the primaries into plasma electrons.

Table 7 indicates that binary collisions play a minor role in the damping of the primary beam. Collisions within the beam itself gives the largest contribution of all the binary collisional processes. The beam-beam collisions initially have a small mean free path but the decay in density due to this type of collision is a power law decay, not an exponential decay. Further, beam-beam collisions do not cause the primary beam to damp. What causes the rapid damping of the beam?

Another mystery lies in accounting for the ion production rate. As noted earlier, ionization due to the high energy Maxwellian tail of the plasma electrons accounts for only 10 to 30% of the total production rate. The direct ionization due to primary electrons has an

extremely large mean free path but the primaries seem to be rapidly damped after being emitted from the hollow cathode. Multistep ionization seems to be negligible, assuming a collision cross section of primaries with excited neutrals of $20 \times 10^{-16} \text{ cm}^2$ (probably too large), an initial primary density of $10^{14}/\text{cm}^3$, and a relaxation time of 10^{-8} s , the mean time between collisions with primaries for excited neutrals is $2 \times 10^{-8} \text{ s}$, therefore $1/3$ of all excited neutrals would still be excited during the collision, but the primary density falls off by at least a factor of 30 within 1 cm of the orifice so this method of ion production seems negligible.

This suggests that collective interactions in the form of strong turbulence plays a central role in energy transfer and ion production. (It is possible, however, that we are not seeing the primaries, many of which might escape the lobular turbulent region. They could account for the ion production rate if they are effectively trapped, for example, by electrostatic trapping between the cathode and extraction grid or magnetic trapping between the anode pole faces and the cathode.)

High frequency turbulence of large enough amplitude if present, could cause the primaries to make a random walk in velocity space that would lead to an enhancement in absolute distance traveled in the turbulent region. This would increase the probability of direct ionization and other binary collisional processes. The turbulence that the primary beam generates could explain the observed heating of the plasma

electrons and ions. In general, turbulence of the proper frequency and amplitude for a given particle retards the migration of that particle from that region. Without this random walk in velocity space the distance traveled from a given point is

$$D = vt \tag{5}$$

but with it the distance traveled is

$$D = v\sqrt{t/\nu} \tag{6}$$

where ν is the collision frequency due to turbulence. If $\nu\ell/v \gg 1$, where ℓ is the size of the turbulent region, the particle has a larger probability of undergoing a binary collision compared to a situation where the turbulence is not present. The possible presence and nature of turbulence is thus an important question.

CHAPTER V
SUMMARY AND DISCUSSION

Plasma properties were mapped out and various loss currents were measured for different thruster configurations. Due to the almost field free interior of the line cusp configuration, the electron temperature was constant throughout the device and the plasma density and potential showed little radial variation, except near the anode walls, between the cusps, where positive potential islands are present, which are large enough to reduce the ion leak width.

The ring cusp designs tested have fields greater than 0.1 kG throughout most of the device, therefore the electron motion is different compared to the line cusp configuration. The radial dependence of electron temperature and plasma density is no longer constant but drops off rapidly, moving away from the device axis; and the electron temperature is no longer constant throughout the device but varies from region to region. Because of the large variations, simple soup pot calculations performed on the line cusp configuration⁷ involving total cusp length, ion and electron leak widths, and loss areas, which had some success in explaining qualitative and some quantitative features of the line cusp observations, become ambiguous in the ring cusp configuration.

Applying some soup pot calculations to the ring cusp configuration, leak widths were calculated using average values of plasma density, temperature, and potential (refer to Table 9). This yielded an ion leak width within a factor of 10 of the ion gyroradius and an electron leak width within a factor of 10 of the electron gyroradius. Grid current was calculated from the ring cusp data as an integral of Bohm velocity times plasma density at $z = -7$ mm (Fig. 24) over the grid area, giving answers within a factor of 2 of the actual currents.

Much higher efficiencies have been obtained in the ring cusp design 2 compared to the line cusp design. Data suggests that the important factor is the number of field lines connecting the cathode with the extraction grid. Enhancing the area of this connection seems to enhance the efficiency. This connection is weak in the line cusp configuration due to the line cusp topology, suggesting that the ring cusp configuration is inherently better.

The reason this type of connection enhances efficiency is strongly dependent on how the primaries generate ions and transfer their energy, which determines where in the main body the ions are generated, and, on how effective the magnetic field is in channeling ions throughout the device.

The interpretation of our data indicates that the primaries are rapidly damped after leaving the cathode orifice. However, measurements of primary density are difficult and the primaries presence could go undetected. If the primaries are rapidly damped, the majority of the ions are produced close to the cathode. This implies that

the magnetic channeling is important. Ions produced in region 2 move freely toward the grid while ions produced in region 1 have a tendency to be magnetically trapped and lost to the anode or cathode. There are problems with this scenario: 1) If more ions are produced near the cathode, ion losses to the cathode could be high, which is not observed. However, the bulk of them are probably produced at least 1 cm away from the cathode where the potential structures channel them toward the grid. 2) In most regions the relative change of magnetic field strength over an ion gyroradius is large, which implies that it is difficult to magnetically trap the ions.

If the primaries are escaping our detection and escape the highly turbulent region, then the scenario is the following. Beam primaries in region 2 will tend to be reflected back and forth between the extraction grid and cathode, losing their energy through inelastic collisions (mainly ionizing) or elastic collisions with plasma electrons. A large fraction of primaries in region 1 will be in the loss cone and lost to the anode pole faces. So enhancing region 2 reduces primary losses in region 1, leading to better plasma production and thus a lower BCF.

If primaries are attenuated or strongly scattered in the highly turbulent region near the cathode, this damping cannot be accounted for by typical mean free path calculations and the nature of this turbulence must be understood.

REFERENCES

- ¹Menon, M. M., et al., Proc. of the 8th Symposium on Engineering Problems of Fusion Research, p. 656, 1979.
- ²Spencer, E. G. and P. H. Schmidt, "Ion beam techniques for device fabrication," J. Vacuum Sci. Tech., 8, 552-570, 1971.
- ³Byers, D. C., V. K. Raulin, "Electron bombardment propulsion system characteristics for large space systems;" Paper no. 76-1039, to be presented at AIAA 12th Electric Propulsion Conference, Key Biscayne, FL, Nov. 1976.
- ⁴Jahn, Robert G., Physics of Electric Propulsion, McGraw-Hill, Inc., New York, 1968.
- ⁵Sovey, J. S., "Improved ion containment using a ring-cusp ion thruster," Proceedings of the 16th International Electric Propulsion Conference, New Orleans, 1982.
- ⁶Siegfried, Dan, Xenon and Argon Hollow Cathode Research, NASA Report No. 168340, 76-121, 1984.
- ⁷Hershkowitz, Noah, John R. Smith, and Hideo Kozima, "Electrostatic self-plugging of a picket fence cusped magnetic field," Phys. Fluids, 22(1), 122-125, 1979.
- ⁸Carpenter, R. T., S. A. Boardsen, and S. V. Daniels, "Plasma characteristics of a 17 cm diameter line-cusp ion thruster," Proceedings of the 16th International Electric Propulsion Conference, New Orleans, 1982.

APPENDIX A
DISCUSSION OF MAGNETIC FIELD PROGRAM

The magnetic field structure inside the ion thruster plays a central role in determining the efficiency of the device. It is important to know how the local and global plasma characteristics correlate with the field structure. A program was developed that determines the field structure of a given ring cusp configuration. This allows the experimenter to check out the field structure of a design before the design is constructed.

The idea is to approximate each magnet row with two current rings with opposite polarity. The field of one current ring can be given in terms of complete elliptic integrals. The solenoidal cathode magnet is approximated by a magnetic dipole. Without the iron shell that composes the anode which serves to complete the magnetic circuit this program would be a very good approximation to the actual field structure. The assumption is that to first order the effect of the shell is to modify the moments of the current rings and dipoles making them appear larger.

Table 8 gives the measured field values at the pole face and the measured local maximum on the device axis near the extraction grid for design 1 and 2. Figures 38, 39, 40, and 41 give graphs of the two

field components along the device axis and at a radial position of 100 mm which sweeps across the pole faces. Comparing the two suggests that the program gives answers that are accurate to within 10%.

APPENDIX B

DISCUSSION OF DATA ANALYSIS PROGRAM

The data analysis program is as follows, given an array $Y = Y[X(i)]$, where Y corresponds to probe current drawn and $X(i)$ corresponds to applied probe voltage. The first derivative at a given point in the array is found by fitting that point and its four nearest neighbors with a four degree polynomial as shown in Fig. 42. The point where the first derivative is a maximum is defined as point B. Then the trace between points A and B are least squares fit to the four parameter curve

$$Y = A + B*X + C*D**X \quad . \quad (B1)$$

The procedure is to pick a value for D . Since Y is linear in A , B , and C , a linear least squares fit can be made holding D constant. Then D is varied as a systematic way, repeating the above procedure until a minimum is found in chi-squared. This yields a curve shown in Fig. 43. $1/\ln(D)$ is proportional to the electron temperature. Next, a linear least squares fit is made on the portion of the probe trace between points $B + \text{DELTA}$ and C . The intersection point of the two fitted curves is used to determine the plasma potential and plasma density (Fig. 44).

Table 1

Typical exhaust velocities for various chemical fuels.

Propellant type	U_{eg} m/sec
Liquid monopropellants	1,700 - 2,900
Solid propellants	2,100 - 3,200
Liquid bipropellants (fuel and oxidizer)	2,900 - 4,500
"Exotic" bipropellants and tripropellants	4,000 - 6,000

Table 2

Table of velocity increments for various impulsive space missions.

Mission	Δv , m/sec
Escape from earth surface (impulsive)	1.12×10^4
Escape from 300-mile orbit (impulsive)	3.15×10^3
Escape from 300-mile orbit (gentle spiral)	7.59×10^3
Earth orbit to Mars orbit and return [†]	1.4×10^4
Earth surface to Mars surface and return [†]	3.4×10^4
Earth orbit to Venus orbit and return [†]	1.6×10^4
Earth orbit to Mercury orbit and return [†]	3.1×10^4
Earth orbit to Jupiter orbit and return [†]	6.4×10^4
Earth orbit to Saturn orbit and return [†]	1.1×10^5

[†]Values are quoted for typical impulsive missions over minimum propellant semiellipse trajectories.

Table 3

Typical operating parameters for thruster operation.

Operating Parameter	Plasma Parameter
Discharge Voltage V_D	20 - 40 volts
Discharge Current I_D	8 - 30 amps
Grid Voltage V_G	~ 50 volts
Extraction Current I_G	0.5 - 4.0 amps
Plasma Density	$10^{11} - 10^{12} \text{ cm}^3$
Electron Temperature	4 - 5 eV
Debye Length λ_D	~ 10^{-3} cm
Electron gyroradius r_e	~ 3×10^{-3} cm
Ion gyroradius r_{Lz}	~ 0.5 cm

Table 4

External operating conditions at which measurements
were made in ring cusp design 1.

	Design 1	Design 2
V_D	28.96 ± 0.3 volts	28.33 ± 0.05 volts
I_D	17.54 ± 0.28 amps	16.5 ± 0.2 amps
I_E	2.09 ± 0.03 amps	2.65 ± 0.05 amps
V_G	52.97 volts	49.20 volts
Neutral Pressure	2.81×10^{-4} torr	3.9×10^{-4} torr
Ion Loss Rate	4 amps	not measured
Electron Loss Rate	22 amps	not measured
Neutral Density	9.25×10^{12} cm ³	12.84×10^{12} cm ³
BFC	243	176

Table 5

Various calculations for ring cusp design 1 and design 2.

	Method	Design 1	Design 2
Ion Production Rate R_I	measured	4 amps	> 2.67 amps
Electron Production Rate R_E	measured	22 amps	> 16.5 amps
Number of Ions in Device N_I	$\int n_p d^3x$	1.24×10^{15}	> 4.8×10^{14}
Average Plasma Density \bar{n}_p	N_I/V	$2.74 \times 10^{11} \text{ cm}^3$	insufficient data
Average Electron Temperature	$\int n_p T_e d^3x$	3.63 eV	3.90 eV
Electron Confinement Time τ_{ce}	$\tau_{ce} = N_I/R_E$	$1.1 \times 10^{-5} \text{ s}$	insufficient data
Ion Confinement Time τ_{ei}	$\tau_{ei} = N_I/R_I$	$5.0 \times 10^{-5} \text{ s}$	"
Neutral Collisions and Electron Undergoes	$\bar{v}_E \sigma n_o \tau_{ce}$	6	"
Rate of Ionization due to Thermal Plasma Electrons	$\int \langle \sigma_I V \rangle n_e n_p d^3x$	0.8 amps	1.4 amps

Table 6

Calculation of initial primary beam density
as it leaves the orifice.

Area of Orifice A_o	0.00454 cm ²
I_D	17 amps
E_p	17 eV
Flux Conservation	$n_B = I_D / e A_o V_B$
V_B	$= c \sqrt{\frac{2 E_p(\text{eV})}{m_e(\text{eV})}} = 2.45 \times 10^8 \text{ cm/s}$
n_B	$= 9.55 \times 10^{13} / \text{cm}^3$

Table 7

Binary collisional information between 17 eV
primaries and other particles.

Particle	Collision Type	Collision Cross Sec. (10^{-16}cm^2)	Mean Free Path (cm)	Primary Collision Frequency with Particle (Hz)
Neutral Argon Atom	elastic	~ 21	51.48	4.75×10^6 Hz
Neutral Argon Atom	inelastic	~ 0.3	3.6×10^3	6.8×10^4 Hz
Neutral Argon Atom	ionizing	~ 0.2	5.4×10^3	4.5×10^4 Hz
Plasma Electron		.769	4.3×10^3	5.7×10^4 Hz
Other Primary		130	0.8 cm	8.5×10^7 Hz

Note:

$$n_o = 9.25 \times 10^{12}/\text{cm}^3$$

$$n_p = 3 \times 10^{12}/\text{cm}^3$$

$$T_p = 1.3 \text{ eV}$$

$$n_B = 10^{14}/\text{cm}^3$$

Table 8

Measured magnetic field values at anode pole faces and orifice; axial maximum near grid for ring cusp design 1 and design 2.

Pole Face	Design 1 (kG)	Design 2 (kG)
A	2.7	2.1
B	2.5	2.5
C	2.5	2.5
D	2.3	2.3
E	2.8	2.1
Cathode Orifice	1.0	0.5
Axial Maximum (near grid)	0.11	0.11

Table 8

Calculated leak widths compared to gyroradius
and ion current to grid.

Particle	Leak Width (cm)	Gyroradius (cm)
Electron	0.017	0.0024
Ion	0.88	0.1 *

$$\text{ion leak width} = I_i / l_c J_i$$

$$\text{electron leak width} = I_e / l_c J_e$$

$$J_i = 1/2 e \bar{n}_p \sqrt{(T_e/m_i)}$$

$$J_e = 1/2 e \bar{n}_p \exp(-\phi_p/T_e) \sqrt{(T_e/m_e)}$$

$$\bar{T}_e = 3.63 \text{ eV}$$

$$\bar{n}_p = 2.74 \times 10^{11} \text{ cm}^{-3}$$

$$I_i \equiv \text{ion current to anode} = 1.7 \text{ Amps}$$

$$I_e \equiv \text{electron current to anode} = 22 \text{ Amps}$$

$$l_c \equiv \text{cusp length} = 290 \text{ cm}$$

$$\phi_p = 3.43 \text{ volts}$$

$$\text{Ion grid current} = \int_{\text{grid}} \frac{1}{2} e \bar{n}_p \sqrt{T_e/m_i} dA = 1.29 \text{ Amps compared to}$$

measured value of 2 Amps.

*Ion energy was assumed to be 0.1 eV in a 2.4 kG field.

Table 9

Calculated leak widths compared to gyroradius
and ion current to grid.

Particle	Leak Width (cm)	Gyroradius (cm)
Electron	0.017	0.0024
Ion	0.88	0.1 *

$$\text{ion leak width} = I_i / l_c J_i$$

$$\text{electron leak width} = I_e / l_c J_e$$

$$J_i = 1/2 e \bar{n}_p \sqrt{(T_e/m_i)}$$

$$J_e = 1/2 e \bar{n}_p \exp(-\phi_p/T_e) \sqrt{(T_e/m_e)}$$

$$\bar{T}_e = 3.63 \text{ eV}$$

$$\bar{n}_p = 2.74 \times 10^{11} \text{ cm}^{-3}$$

$$I_i \equiv \text{ion current to anode} = 1.7 \text{ Amps}$$

$$I_e \equiv \text{electron current to anode} = 22 \text{ Amps}$$

$$l_c \equiv \text{cusp length} = 290 \text{ cm}$$

$$\phi_p = 3.43 \text{ volts}$$

$$\text{Ion grid current} = \int_{\text{grid}} \frac{1}{2} e \bar{n}_p \sqrt{T_e/m_i} dA = 1.29 \text{ Amps compared to}$$

measured value of 2 Amps.

*Ion energy was assumed to be 0.1 eV in a 2.4 kG field.

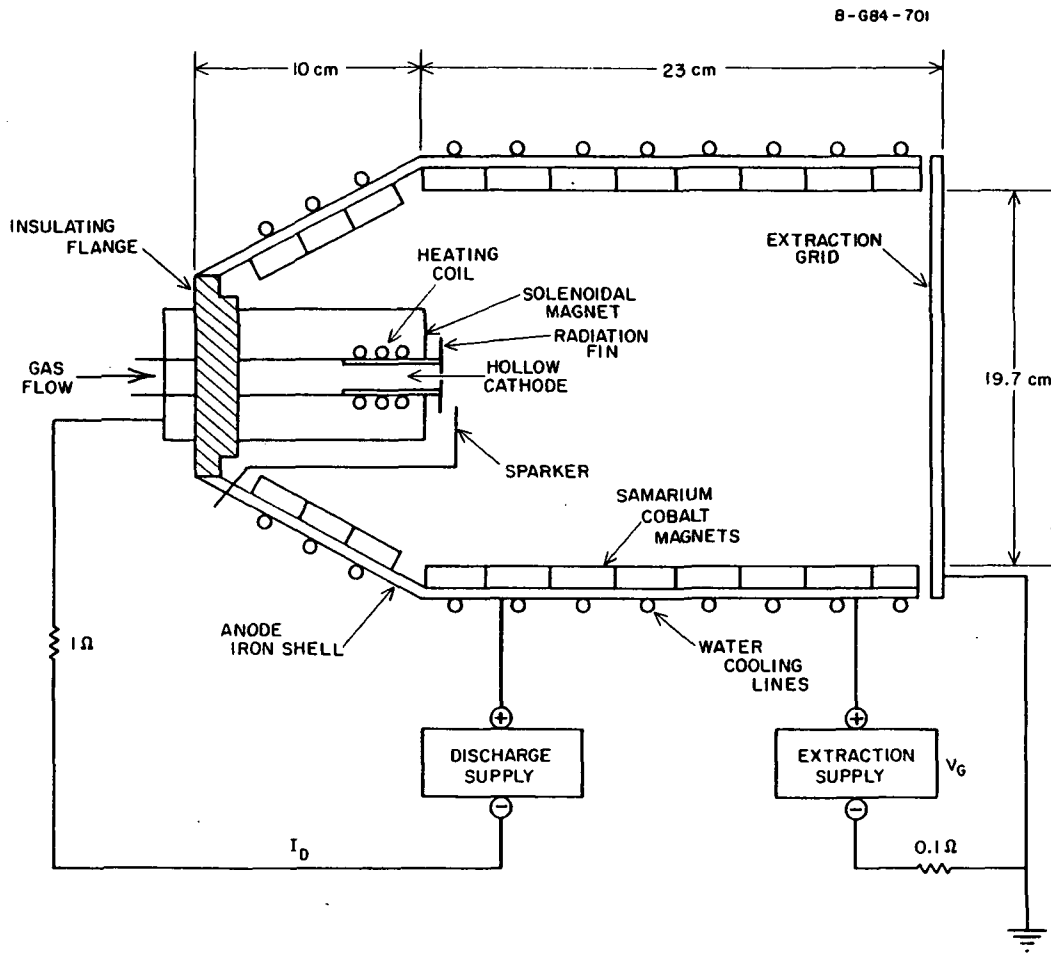


Figure 1. Diagram of line cusp configuration.

A-684-702

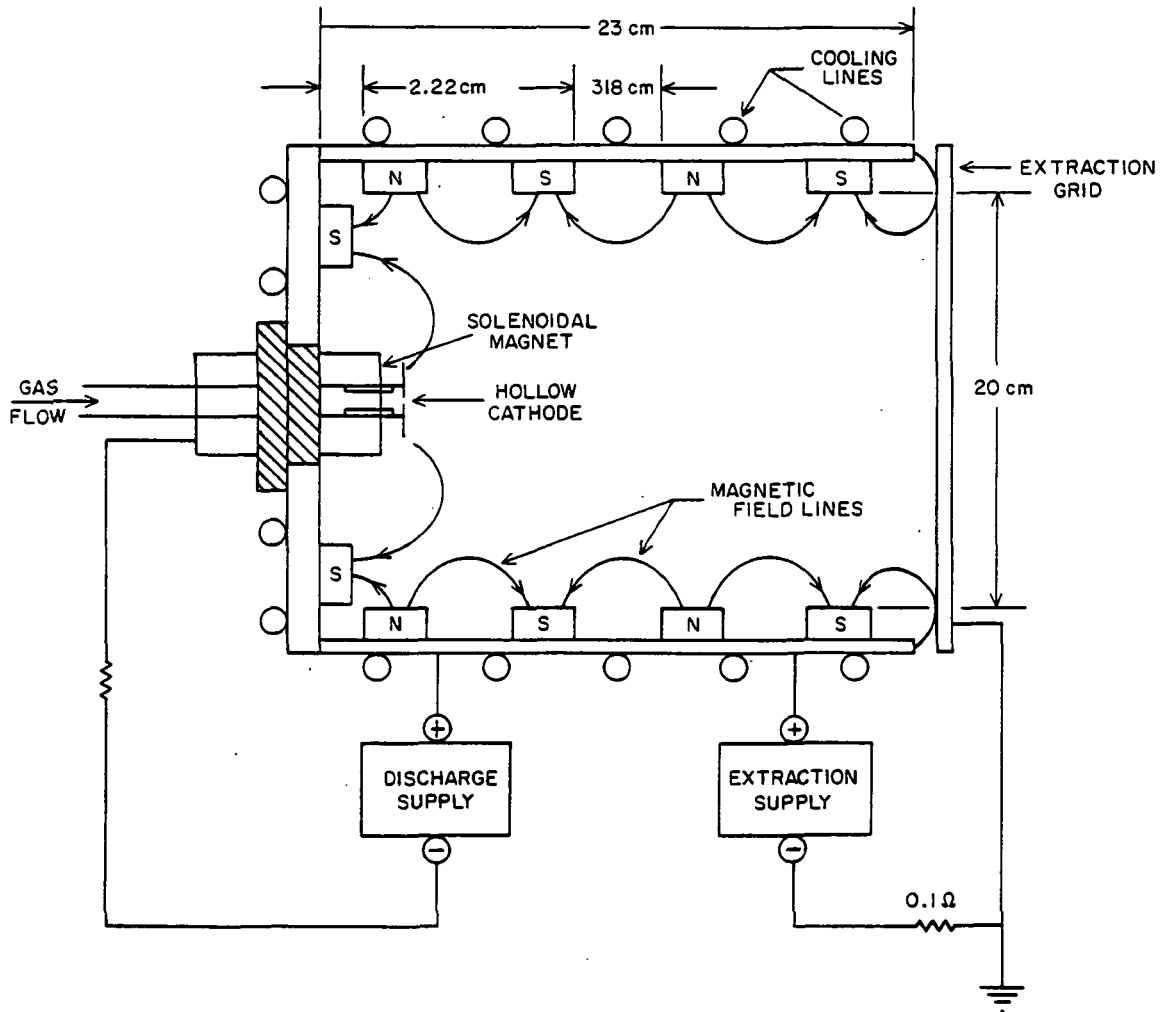


Figure 2. Diagram of ring cusp configuration.

c-2

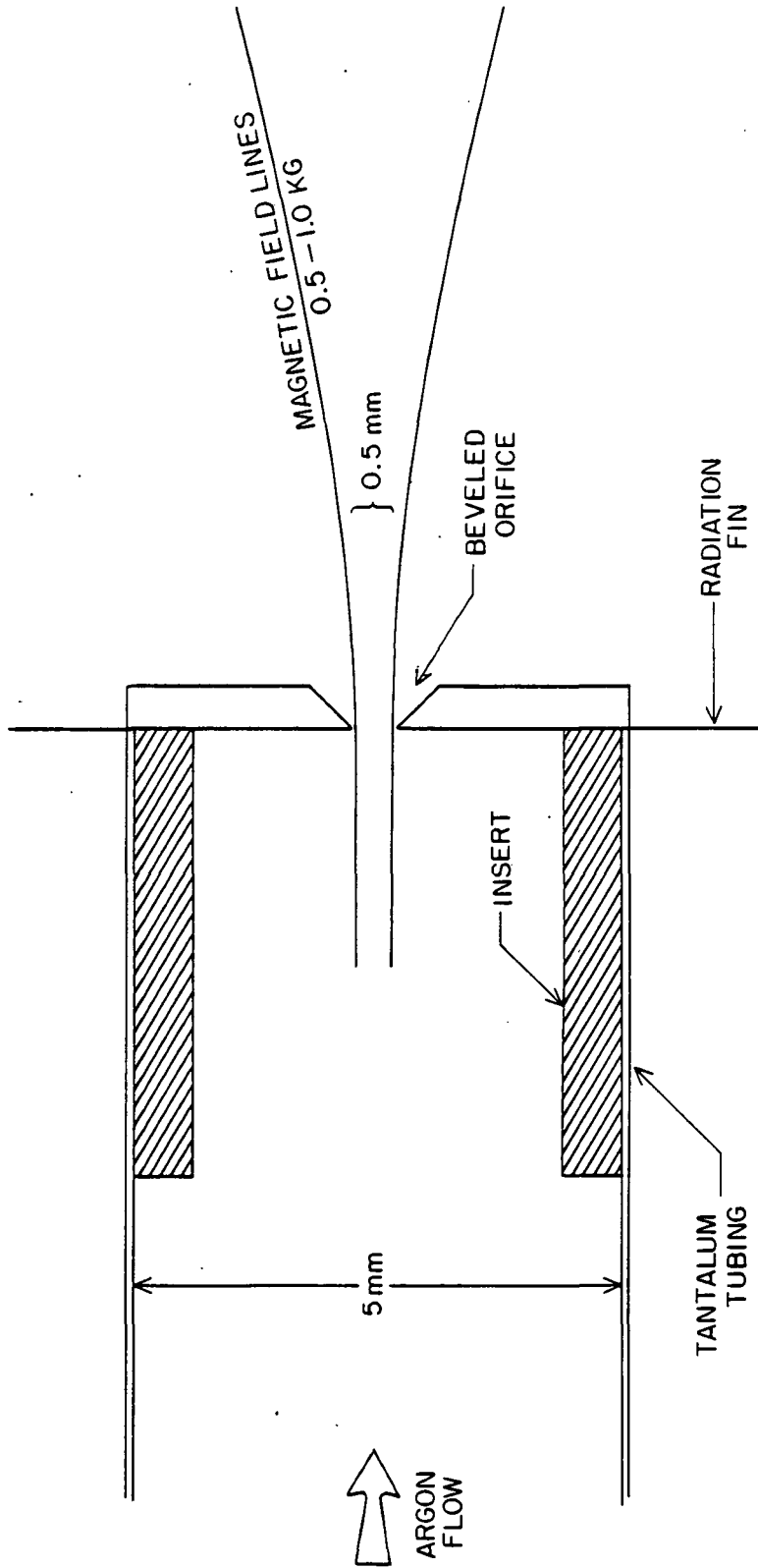


Figure 3. Diagram of hollow cathode.

A-G84-794

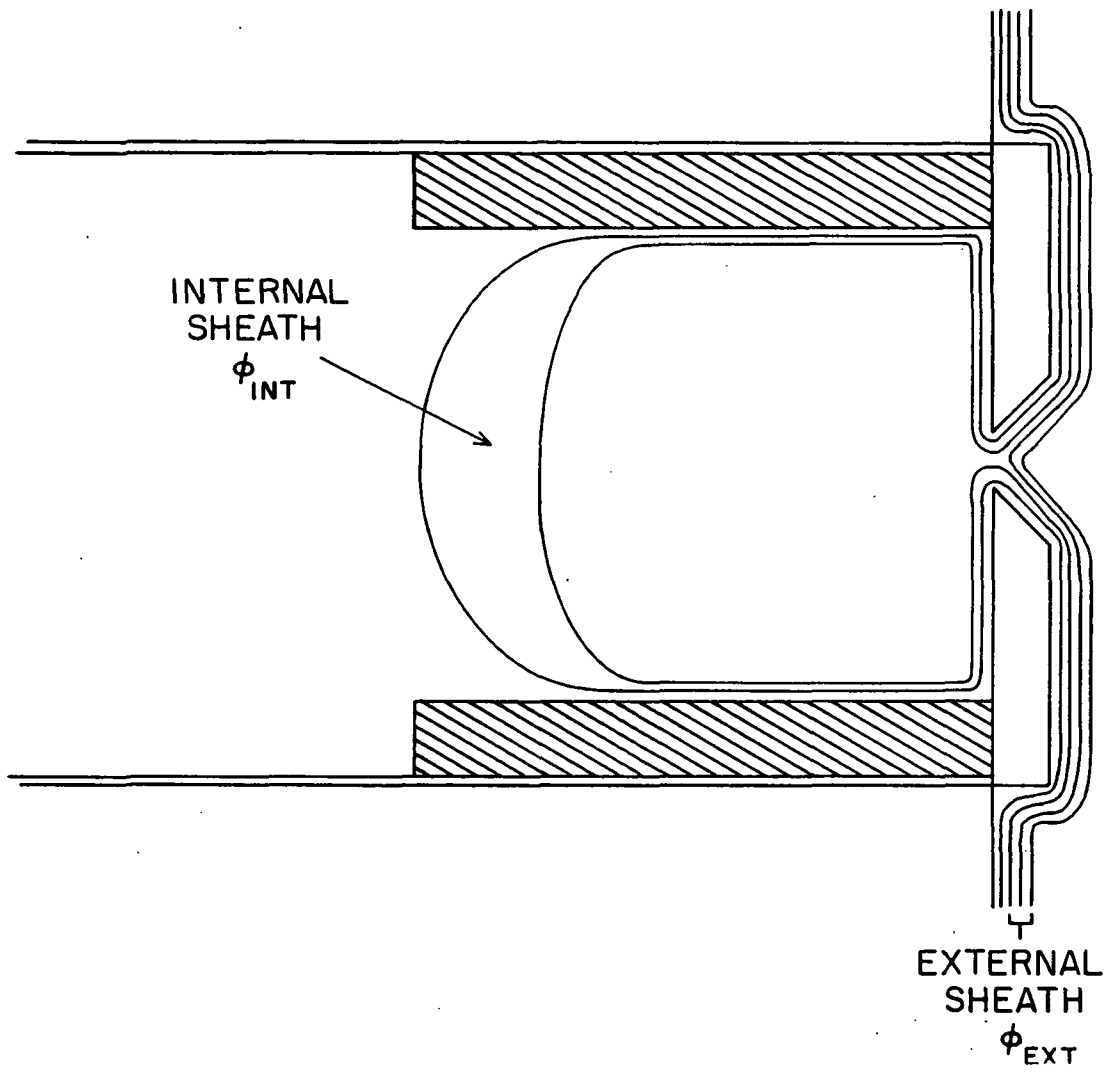


Figure 4. Qualitative potential structure around cathode.

MAGNETIC FIELD STRENGTH CONTOURS

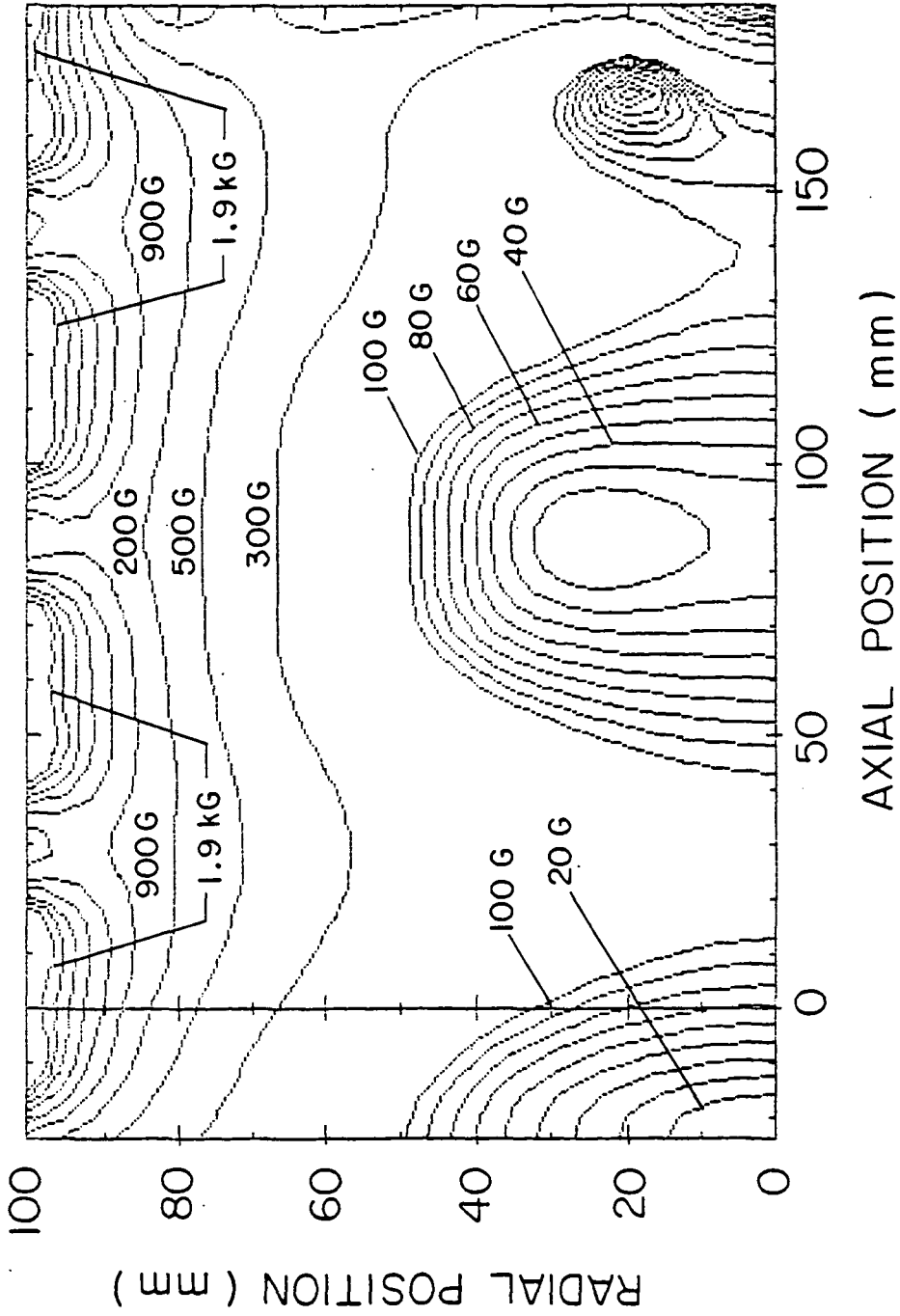


Figure 5. Magnetic field strength contour plot of ring cusp design 2.

LINES OF MAGNETIC FIELDS

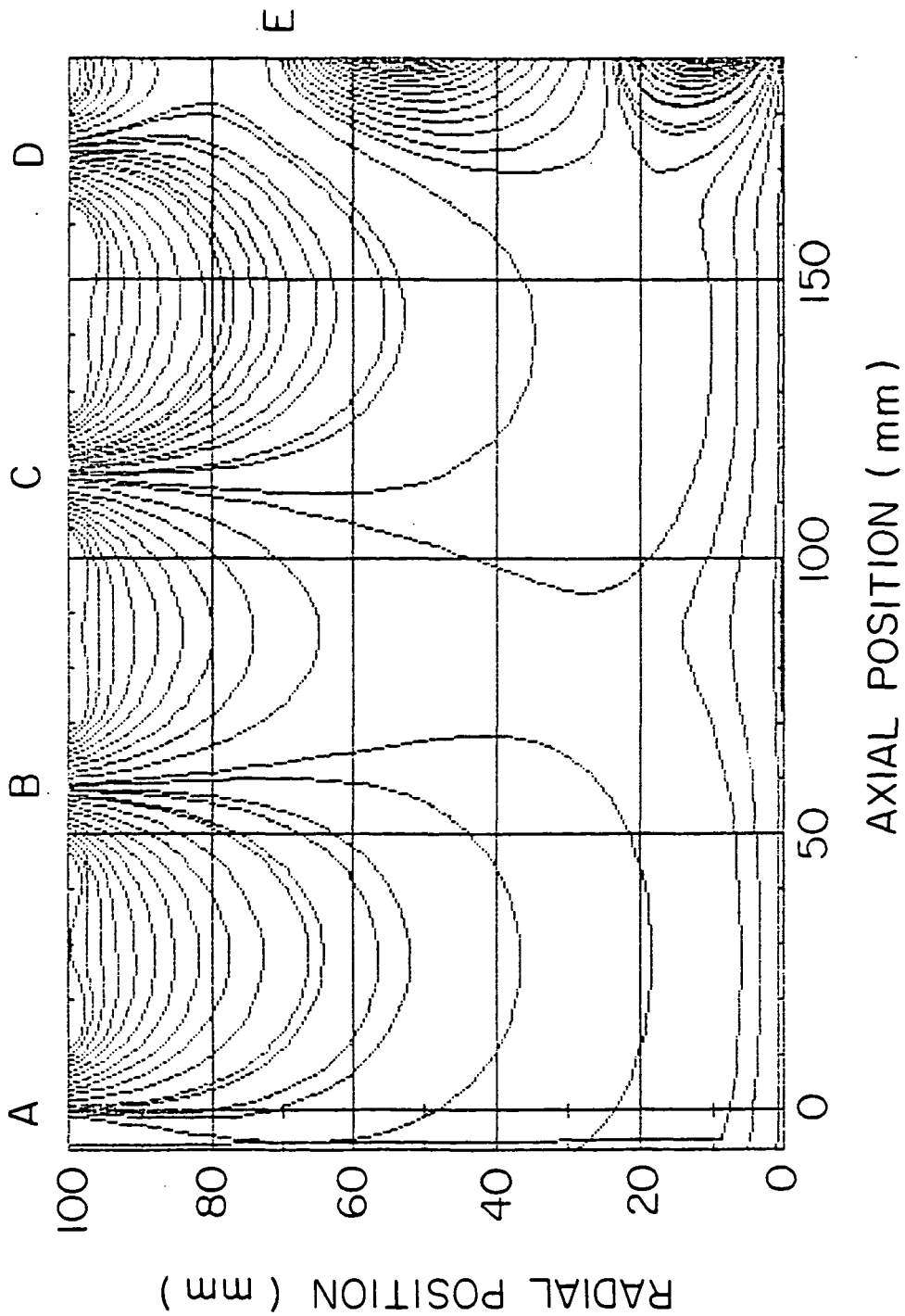


Figure 6. Magnetic field direction plot of ring cusp design 2.

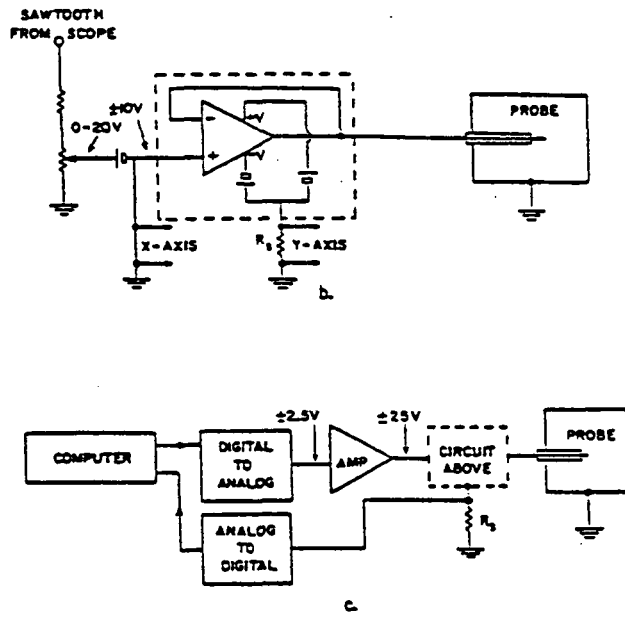
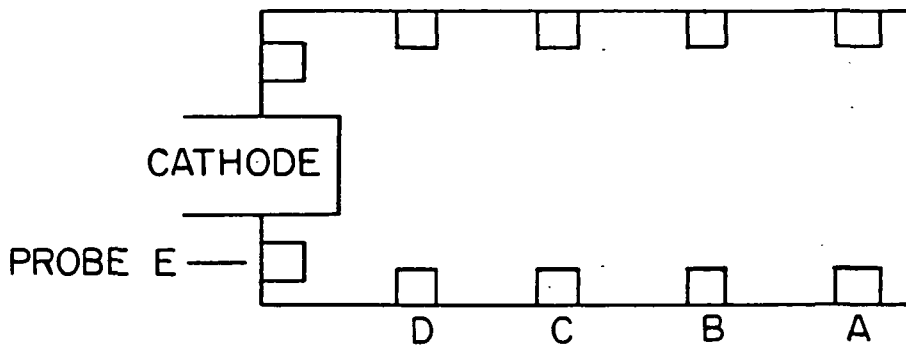


Figure 7. Schematic of probe sweep circuit.

LOCATION OF PROBES



CATHODE PROBE (FACE OF CATHODE)

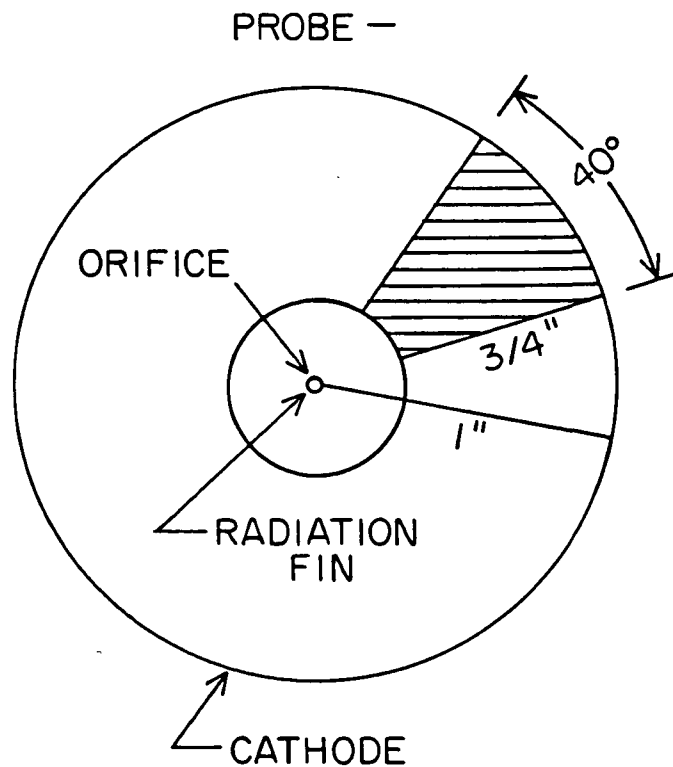


Figure 8. Location of probes. (a) Probe locations on anode.
 (b) Probe locations on cathode.

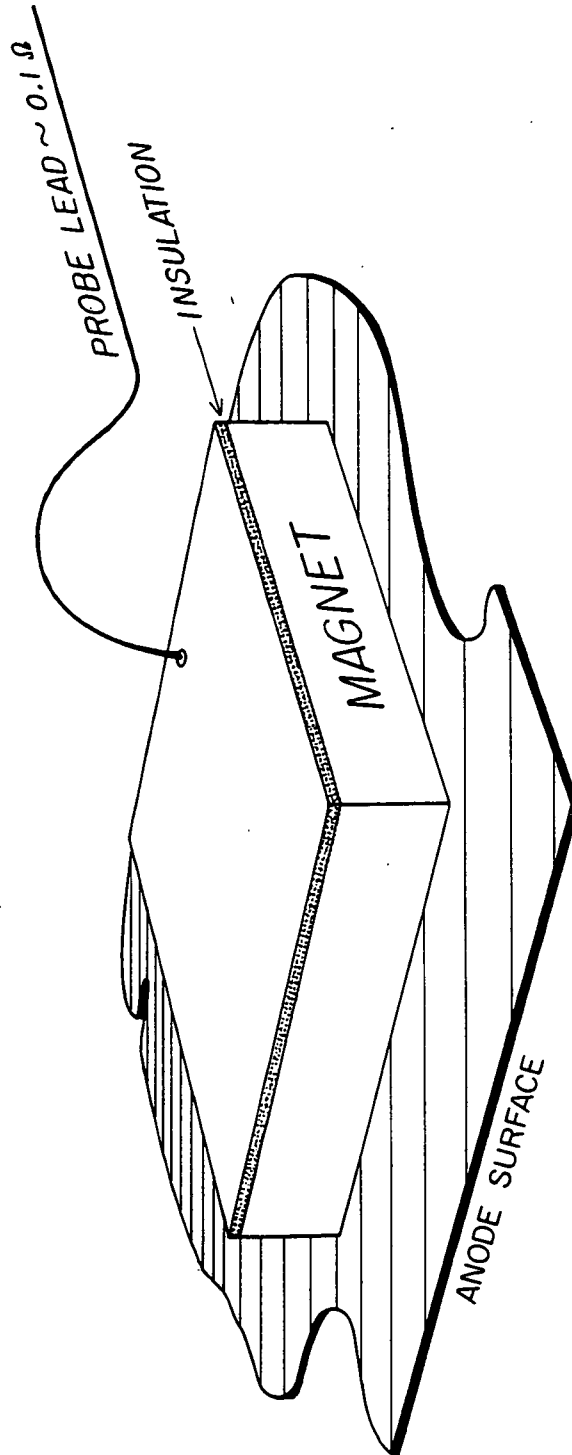


Figure 9. Setup for measuring total current.

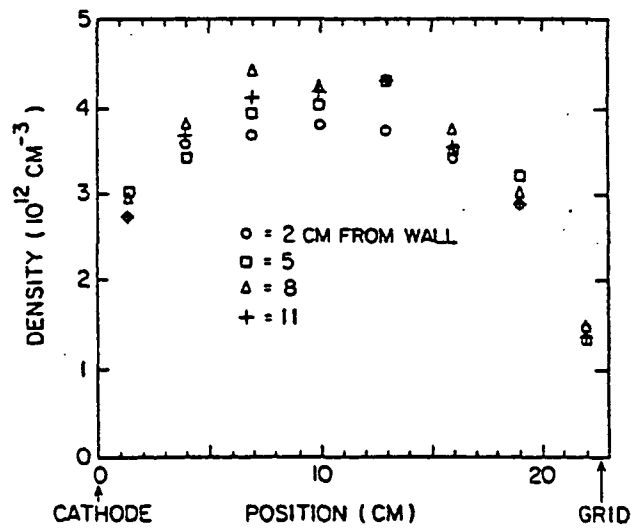


Figure 10. Plasma density at various distances from the anode wall in the line cusp configuration $I_D = 20$ amps.

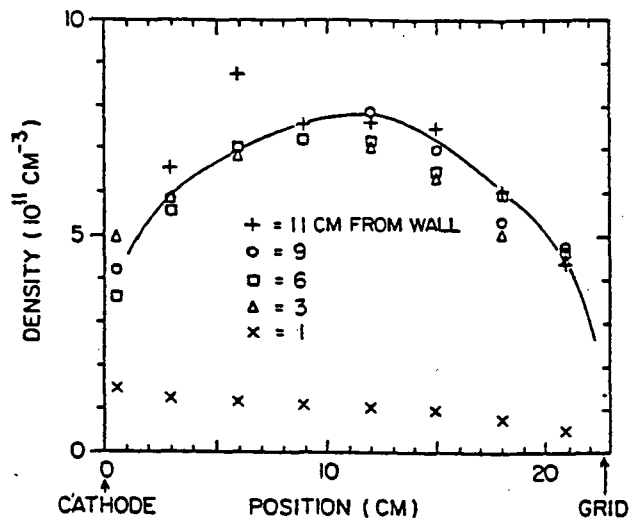


Figure 11. Plasma density at various distances from the anode wall in the line cusp configuration $I_D = 12$ amps.

A-684-769

ELECTRON TEMPERATURE

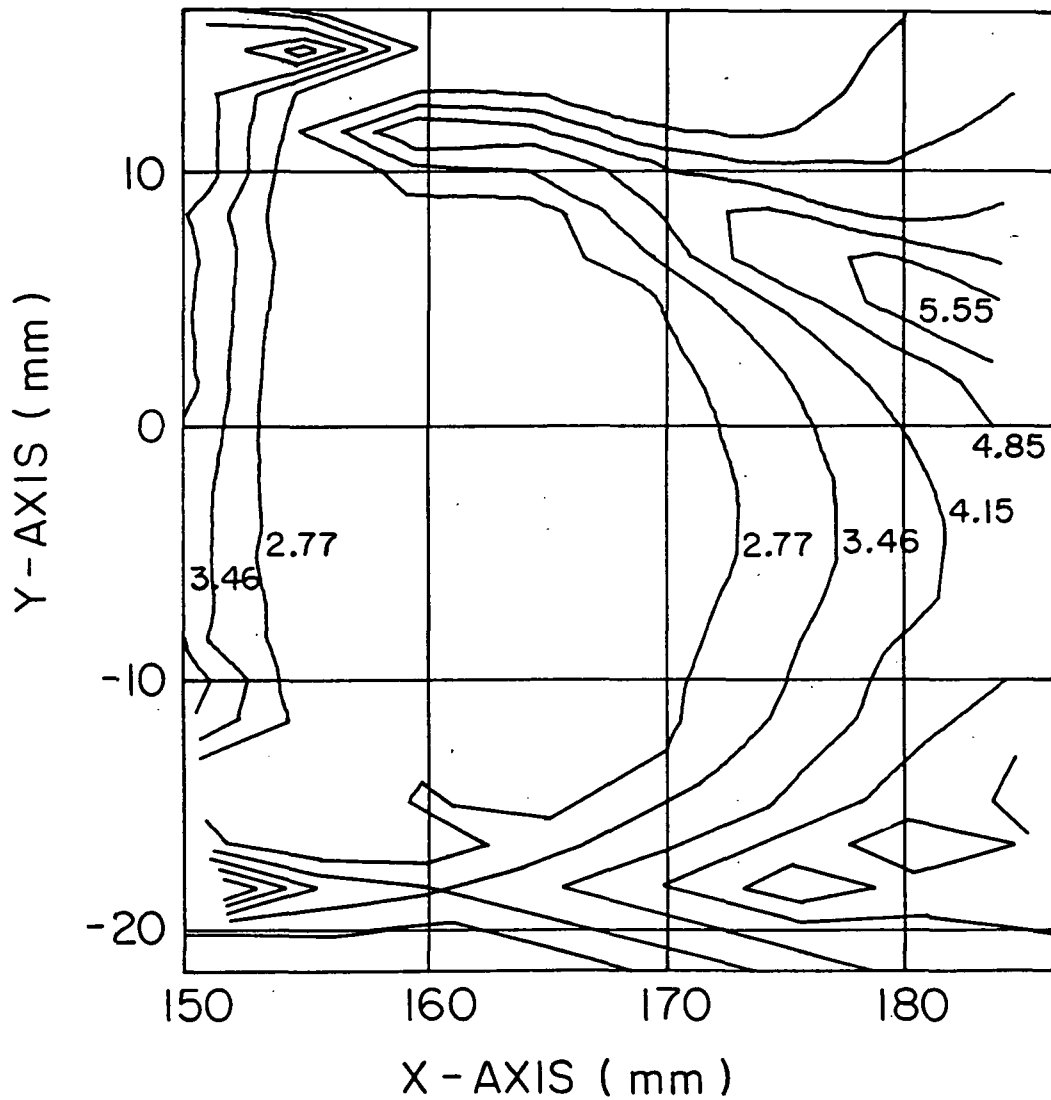


Figure 12. Contour map of electron temperature in the line cusp configuration in electron volts. $V_D = 33.26$ volts, $I_D = 20.2$ amps, $I_G = 2.5$ amps, Pressure = 2.8×10^{-4} mm Hz.

A-G84-770

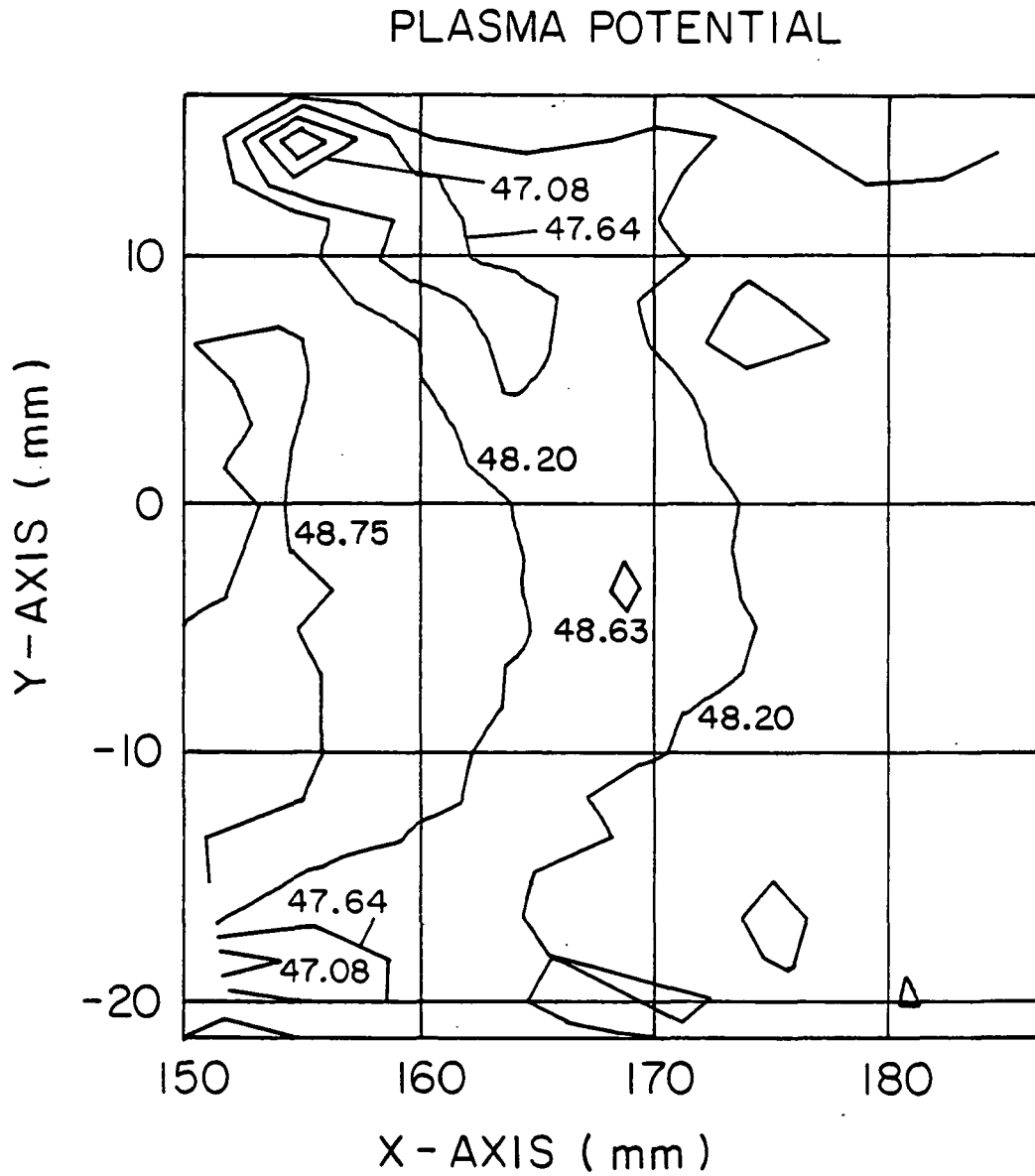


Figure 13. Contour map of plasma potential in units of volts in the line cusp configuration.

A-684-771

PLASMA DENSITY

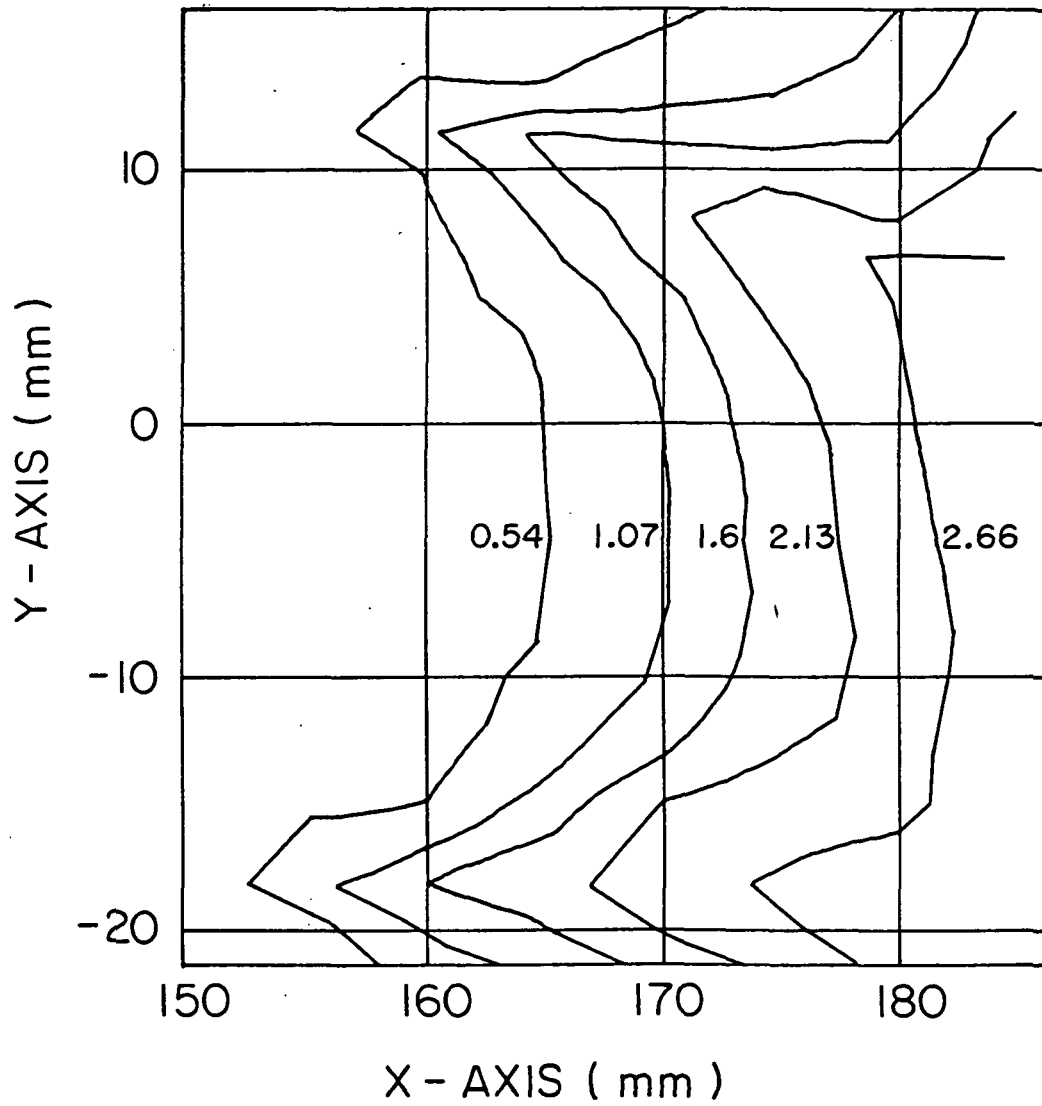


Figure 14. Contour map of plasma density in units of 10^{12} cm^{-3} in the line cusp configuration.

A-684-805

MAGNETIC FIELD STRENGTH CONTOURS

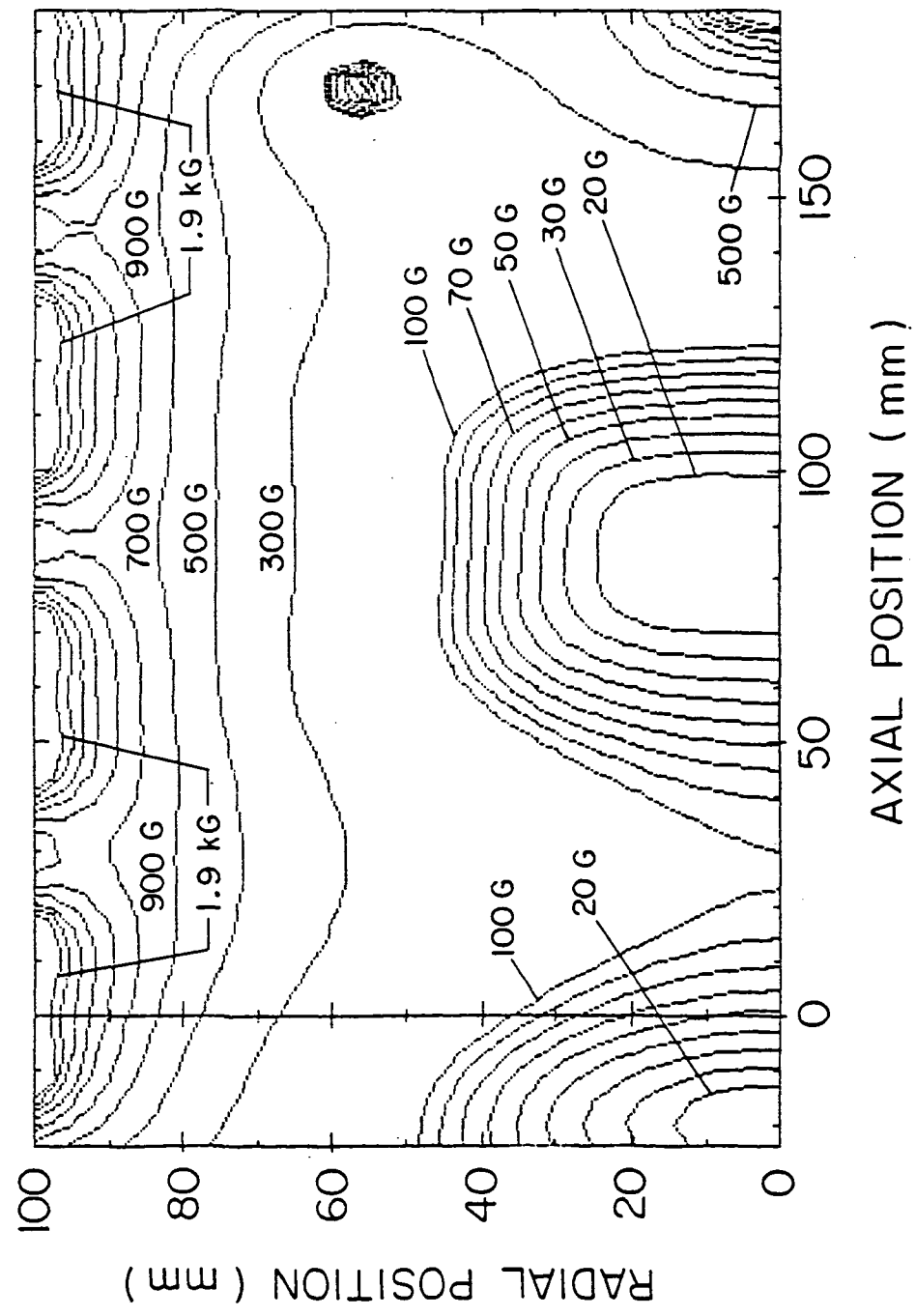


Figure 15. Magnetic field strength contour plot for ring cusp design 1.

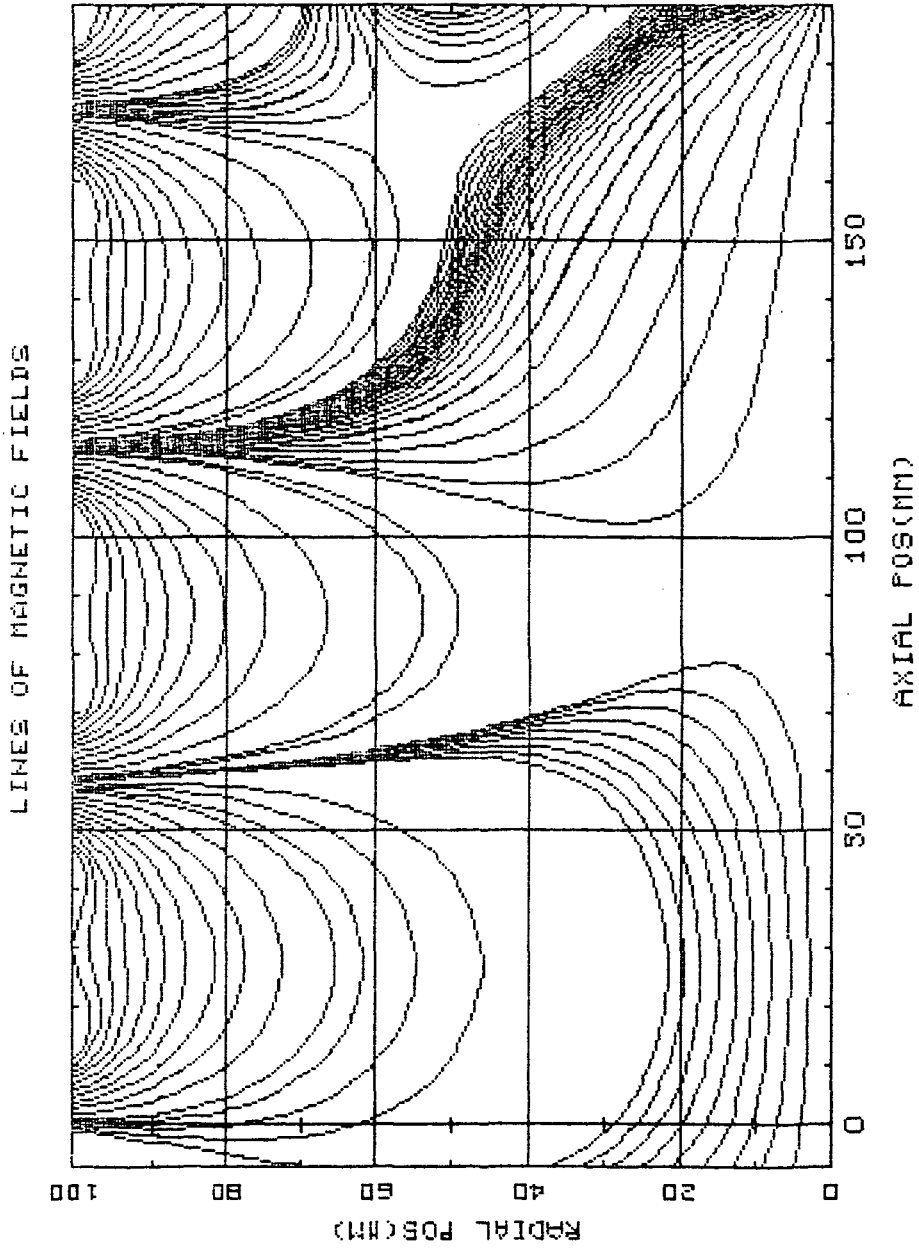


Figure 16. Magnetic field direction plot for design 1.

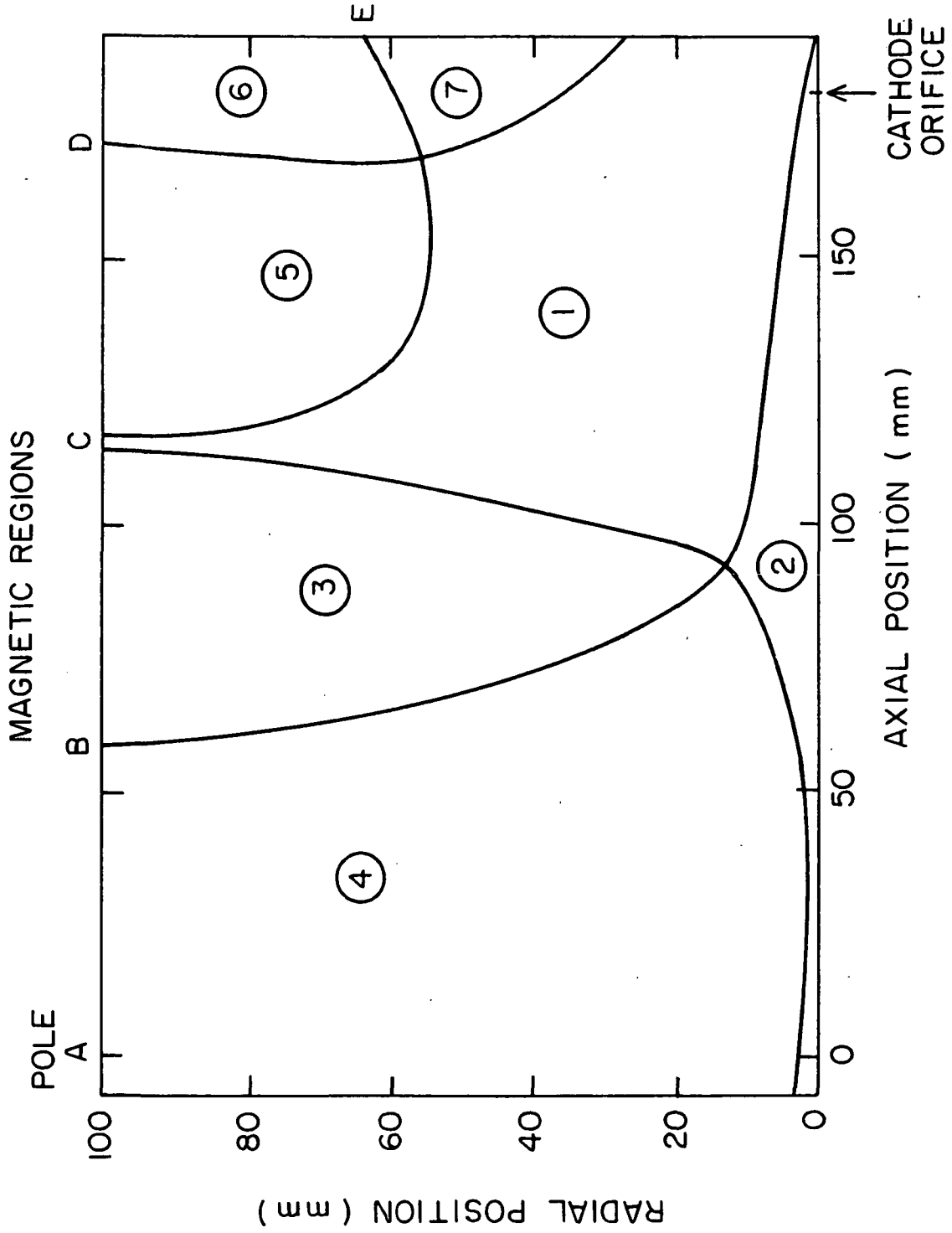


Figure 17. The 7 regions into which the thruster is divided by the magnetic flux tubes.

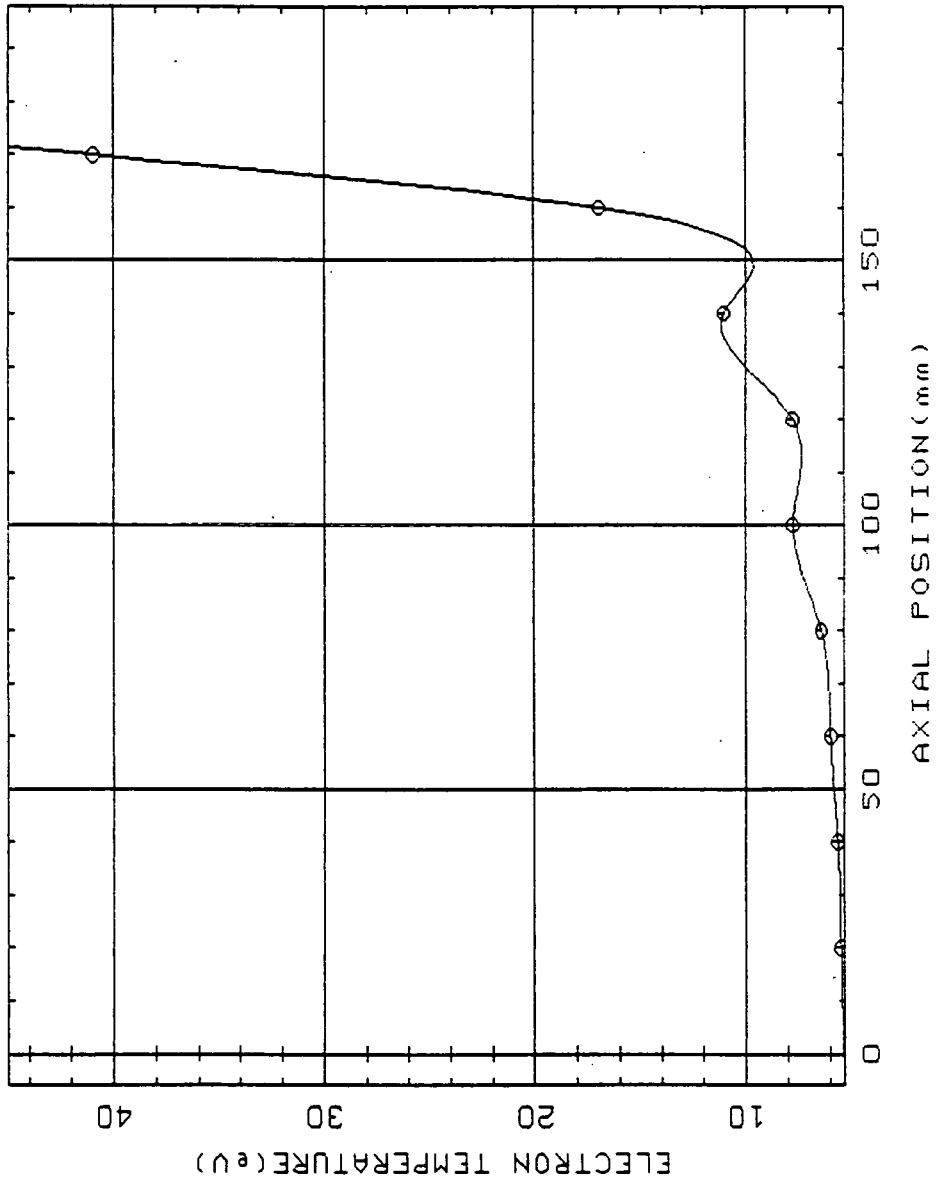


Figure 18. Axial profile of electron temperature along the device axis in ring cusp design 1. Dots indicate data points.

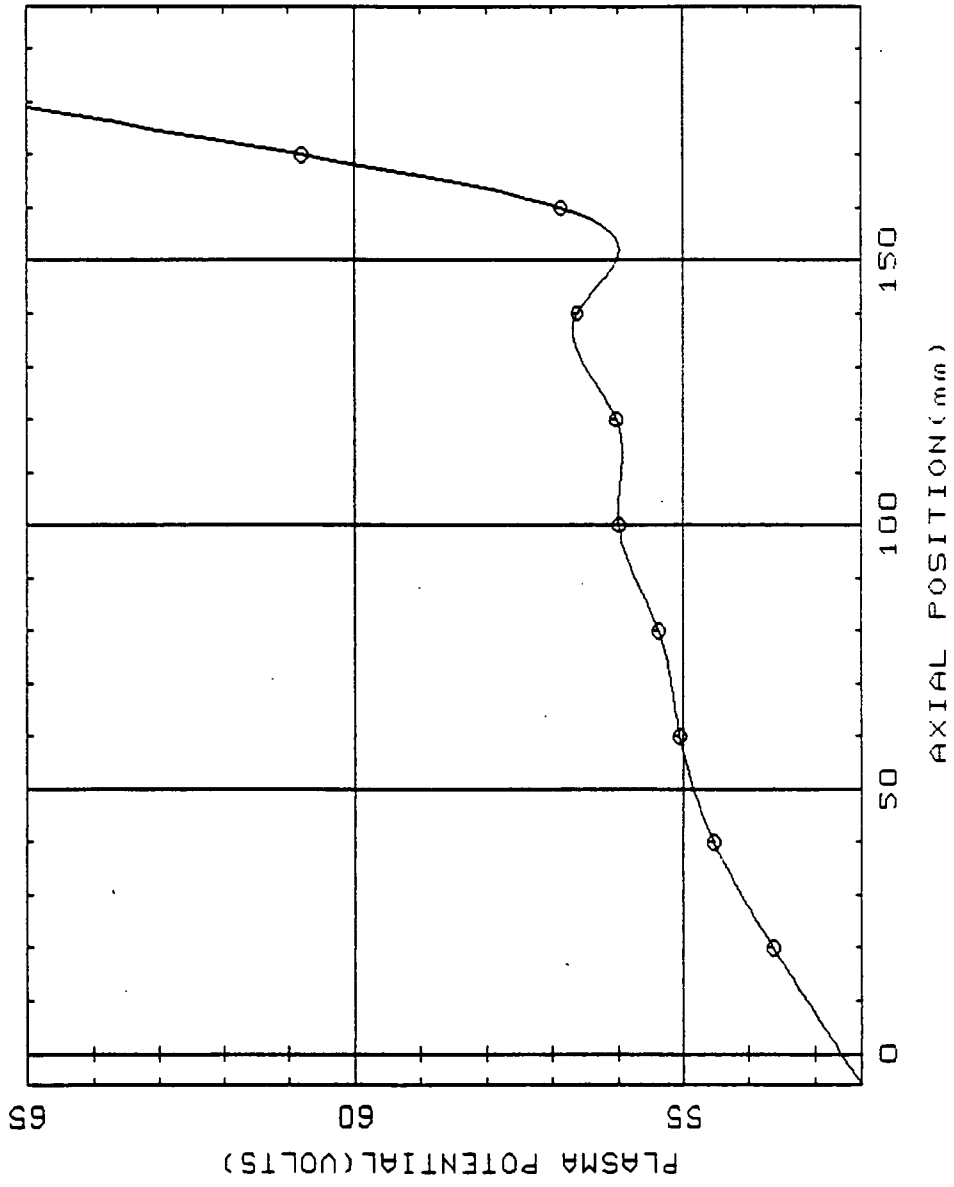


Figure 19. Axial profile of the plasma potential along the device axis for ring cusp design 1.

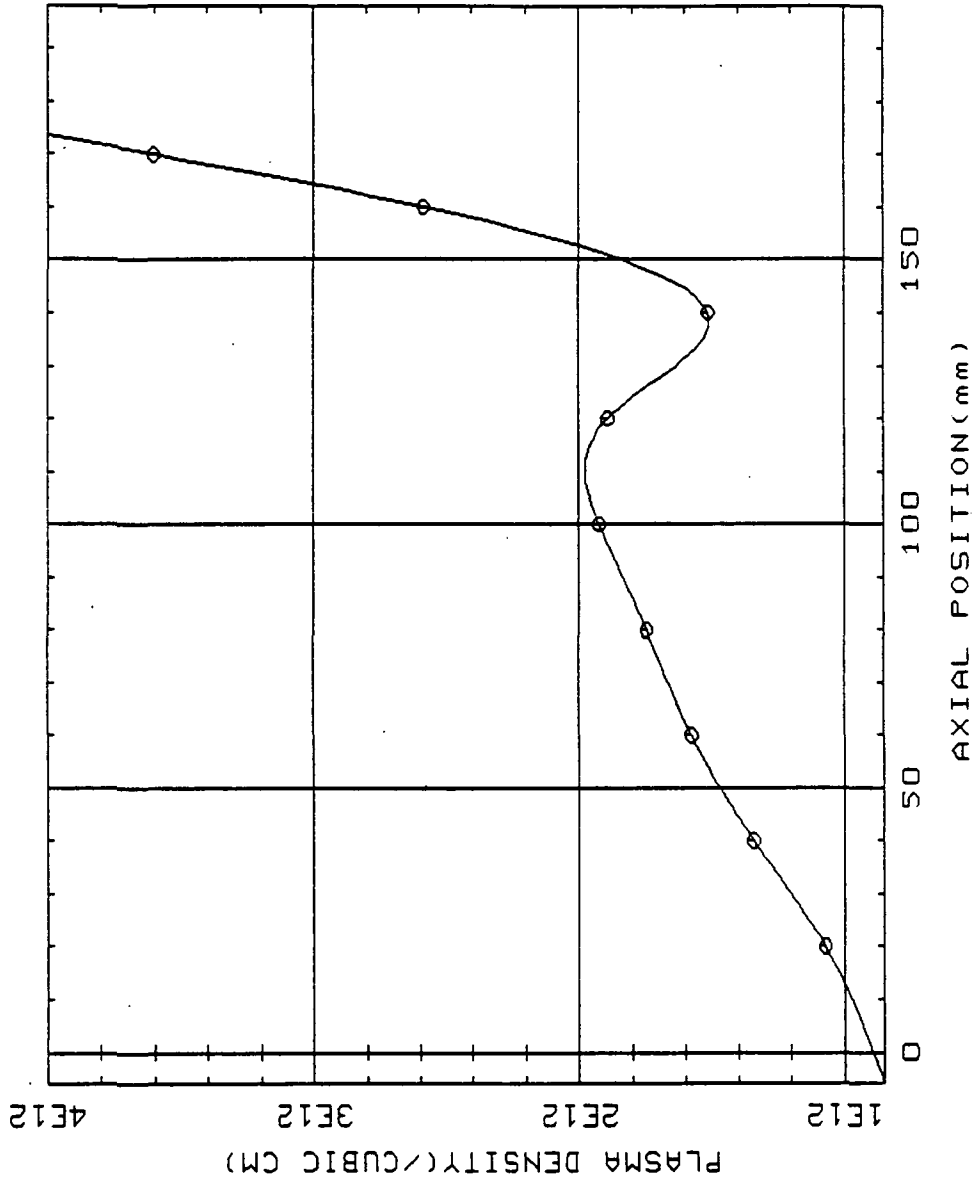


Figure 20. Axial profile of plasma density along the device axis for ring cusp design 1.

A-684-772

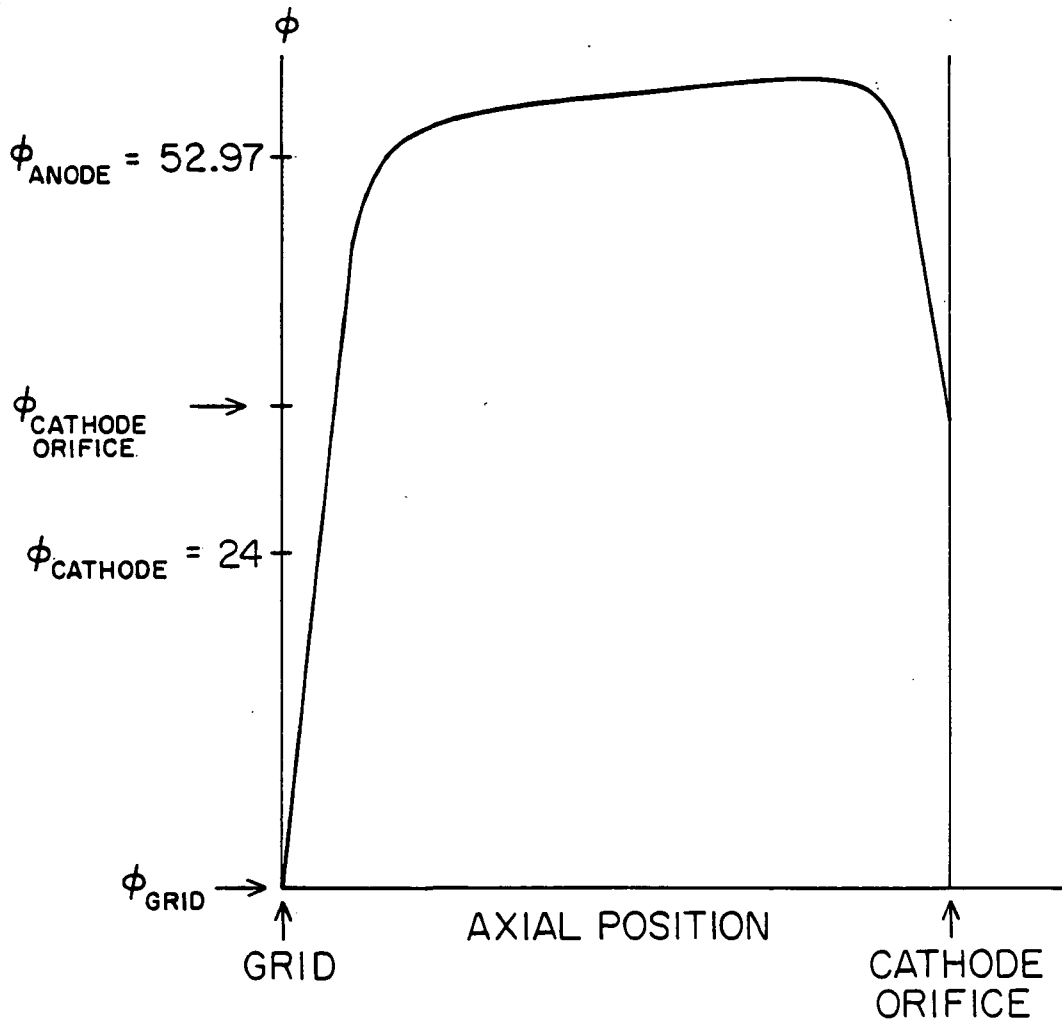


Figure 21. Qualitative structure of the potential between grid and cathode orifice.

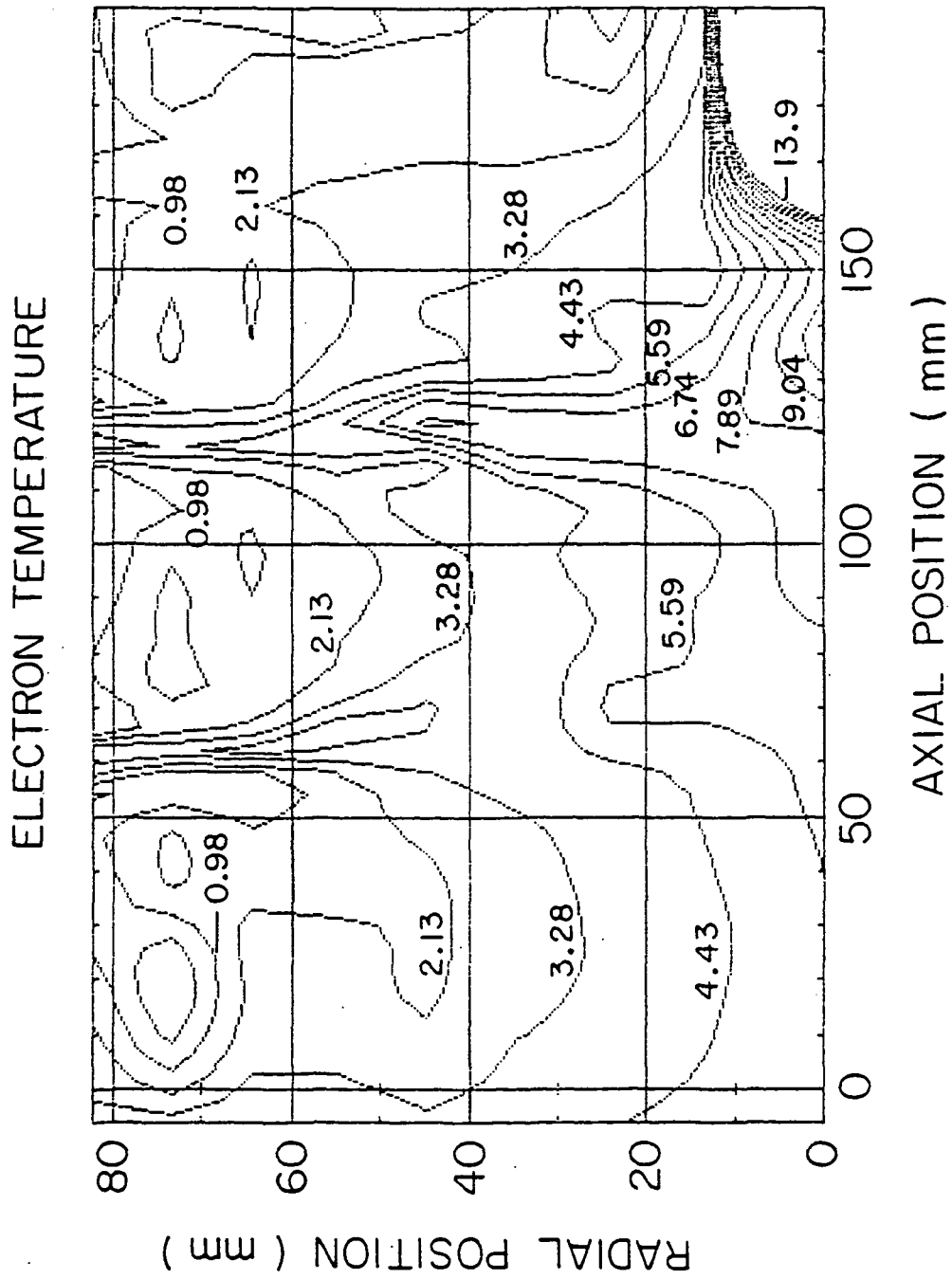


Figure 22. Contour map of electron temperature in eV for ring cusp design 1.

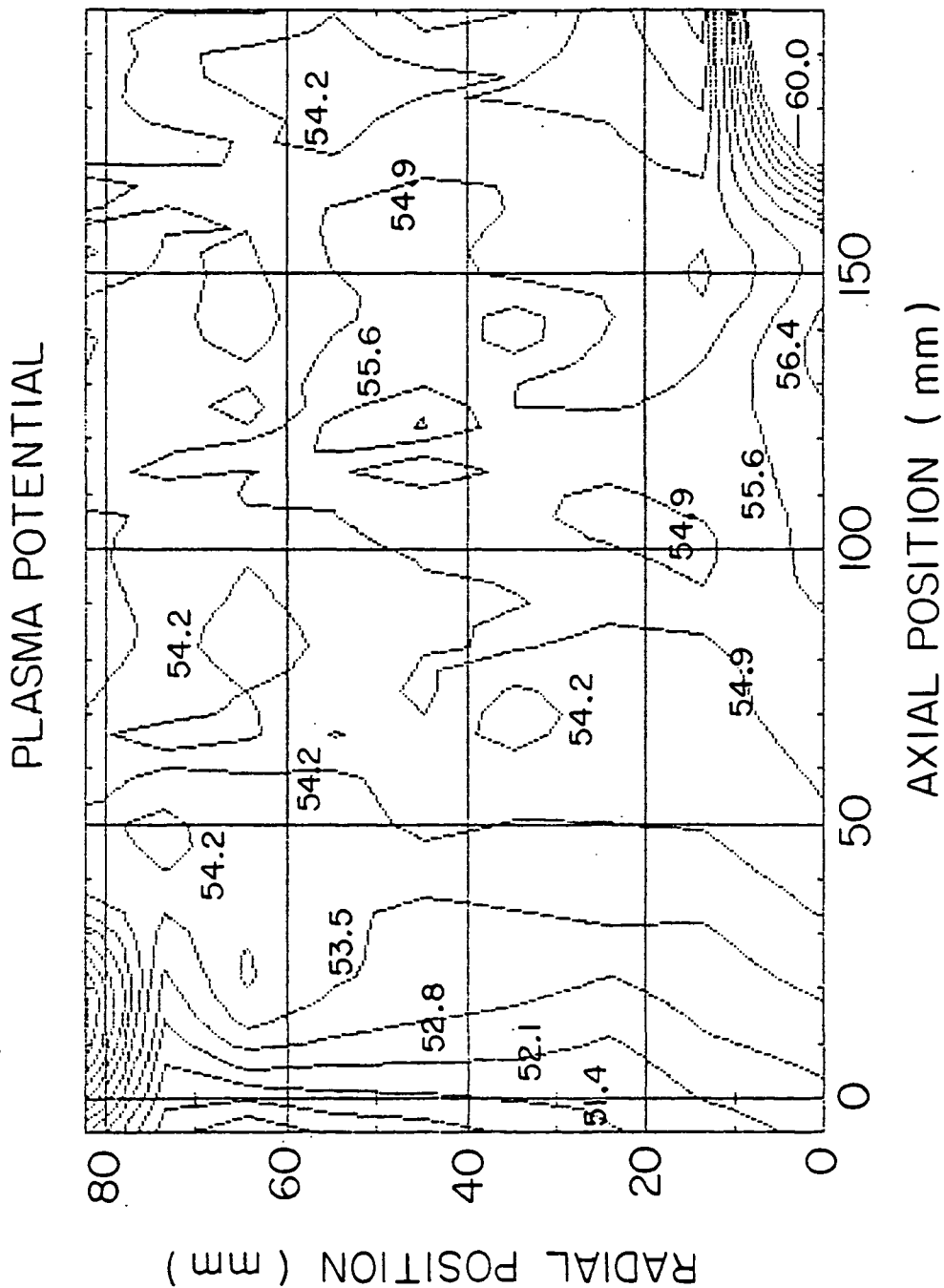


Figure 23. Contour map of plasma potential in volts for ring cusp design 1.

A-684-800

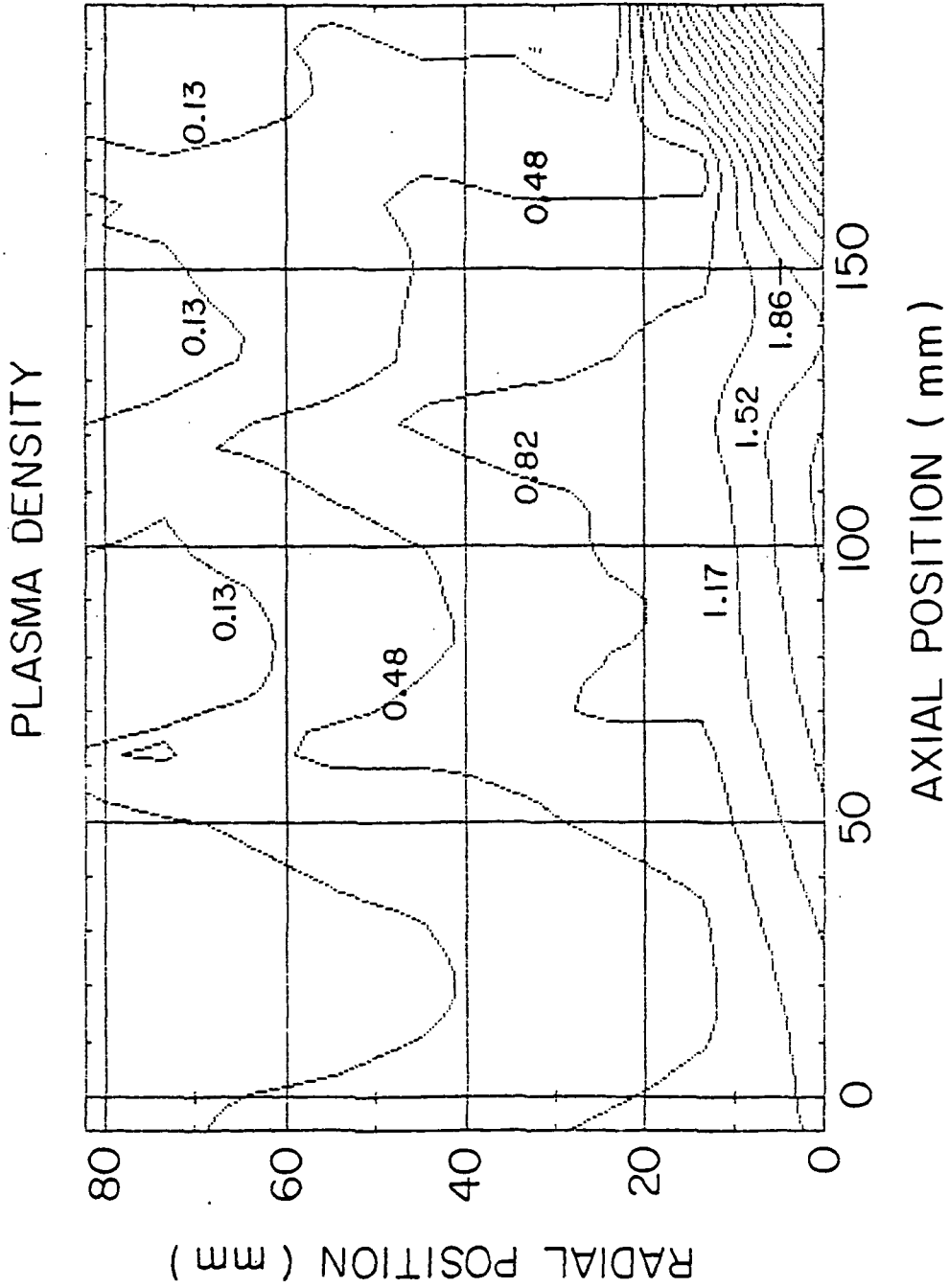


Figure 24. Contour map of plasma density in units of 10^{12} cm^{-3} for ring cusp design 1.

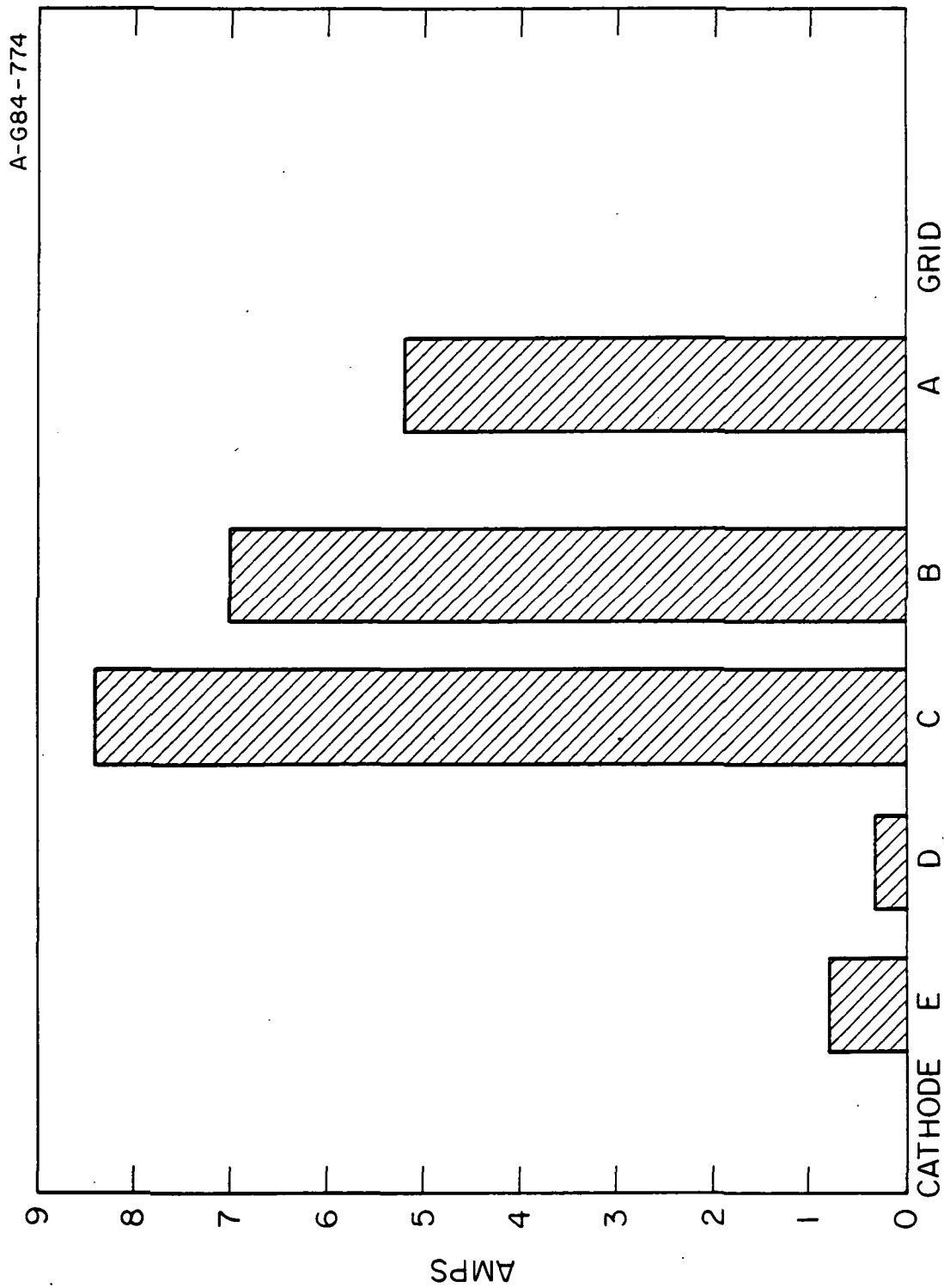


Figure 25. Electron currents to anode and cathode pole faces.

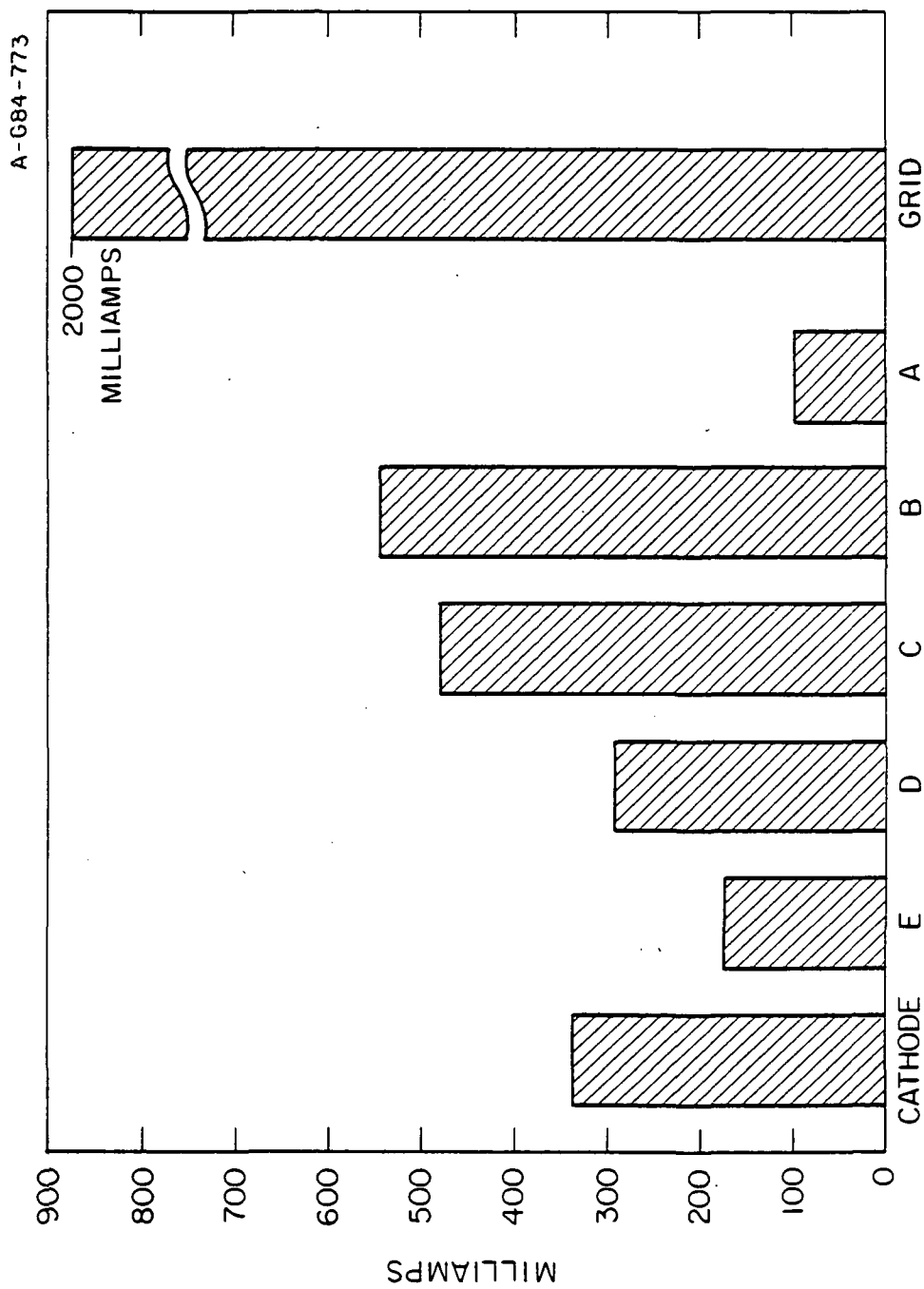


Figure 26. Ion current to pole faces.

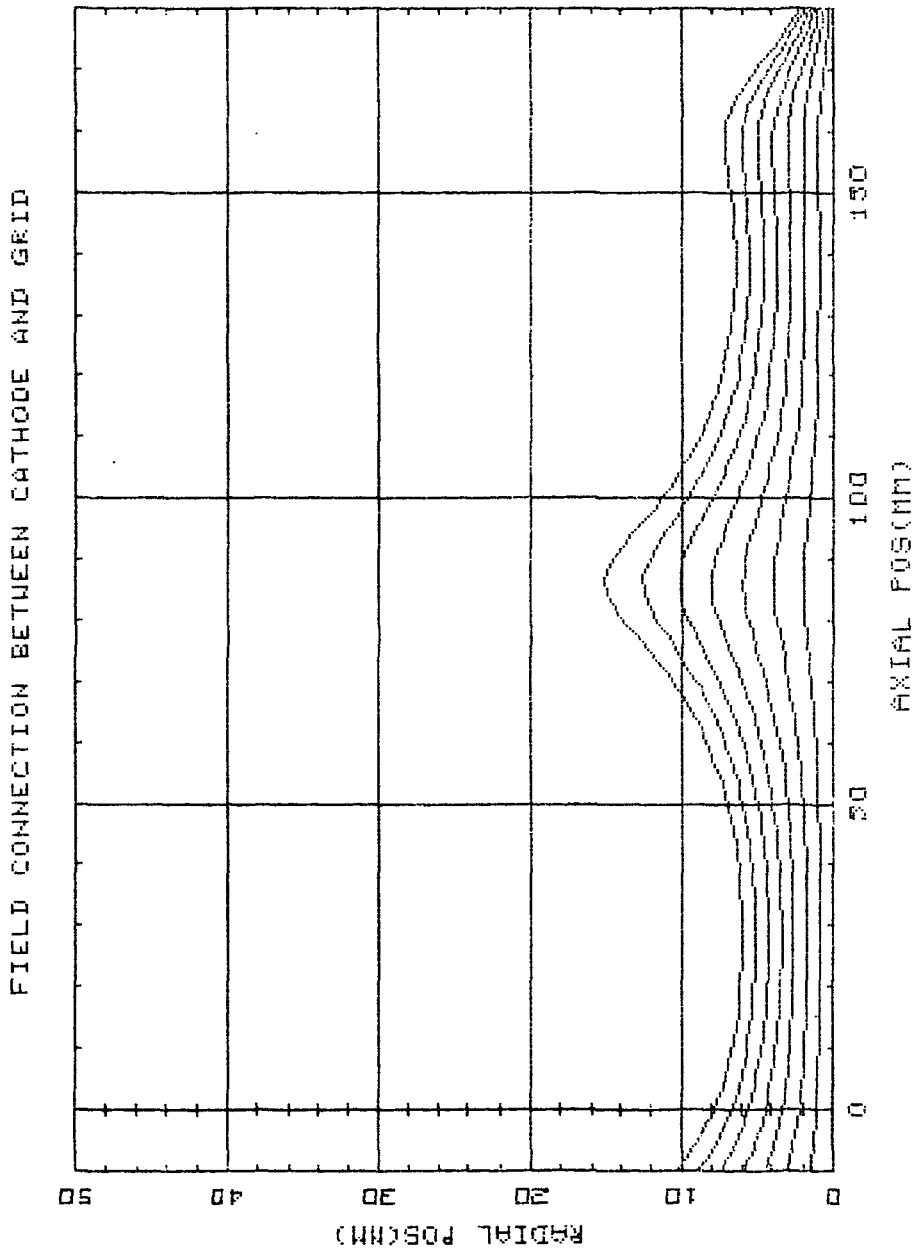


Figure 27. Amount of field linkage between grid and orifice design 2.

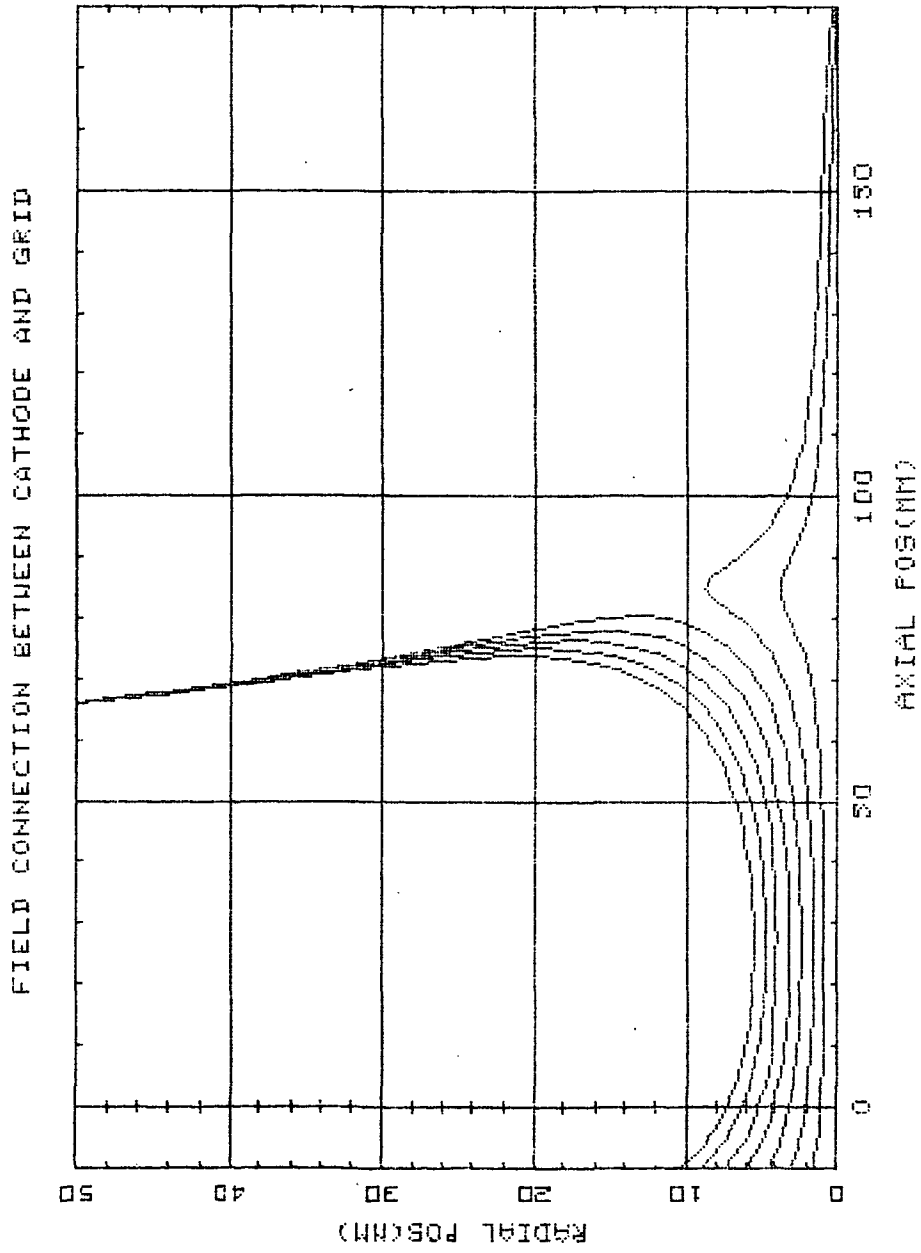


Figure 28. Amount of field linkage between grid and orifice design 1.

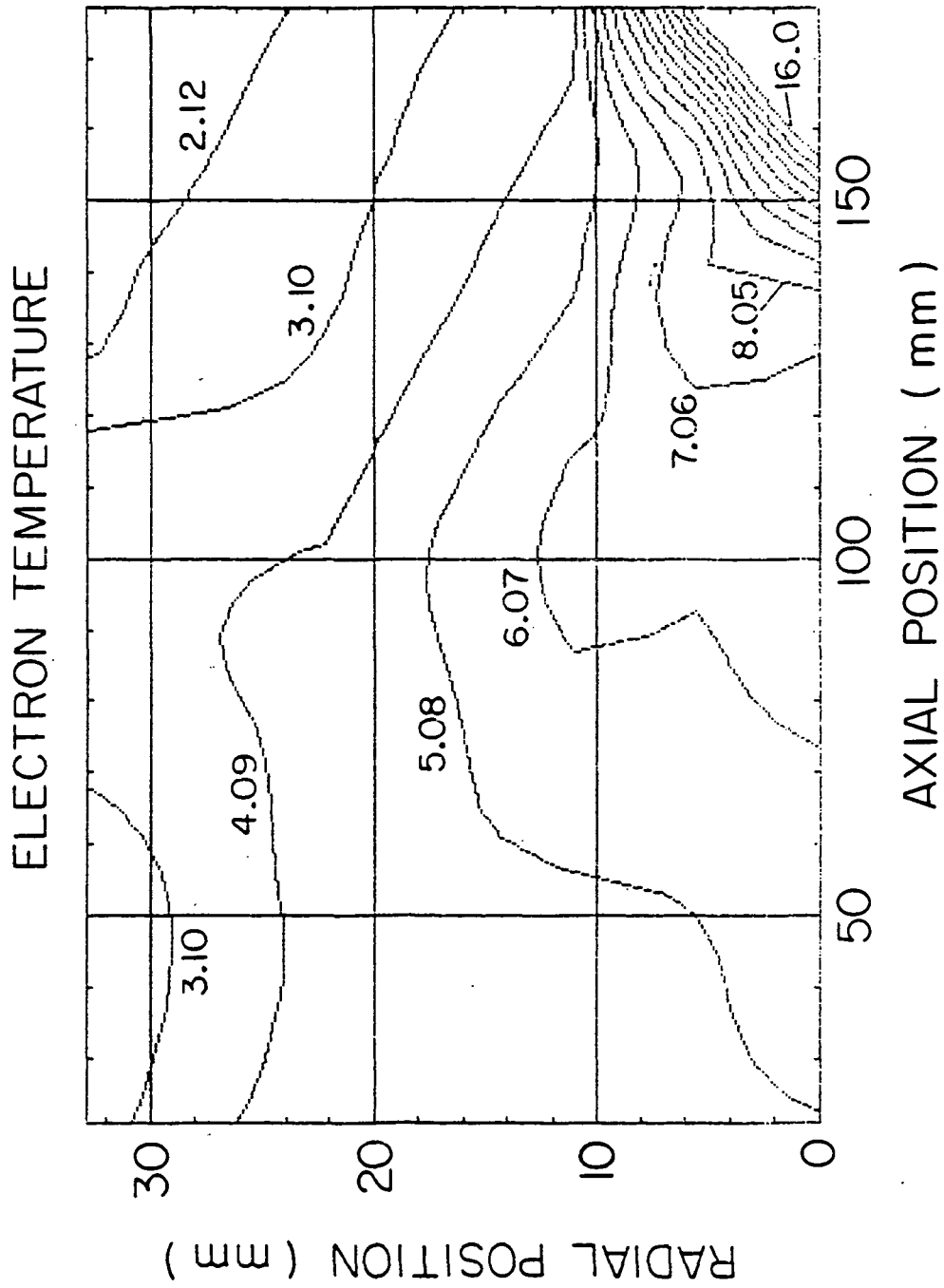


Figure 29. Contour map of electron temperature in eV for design 2.

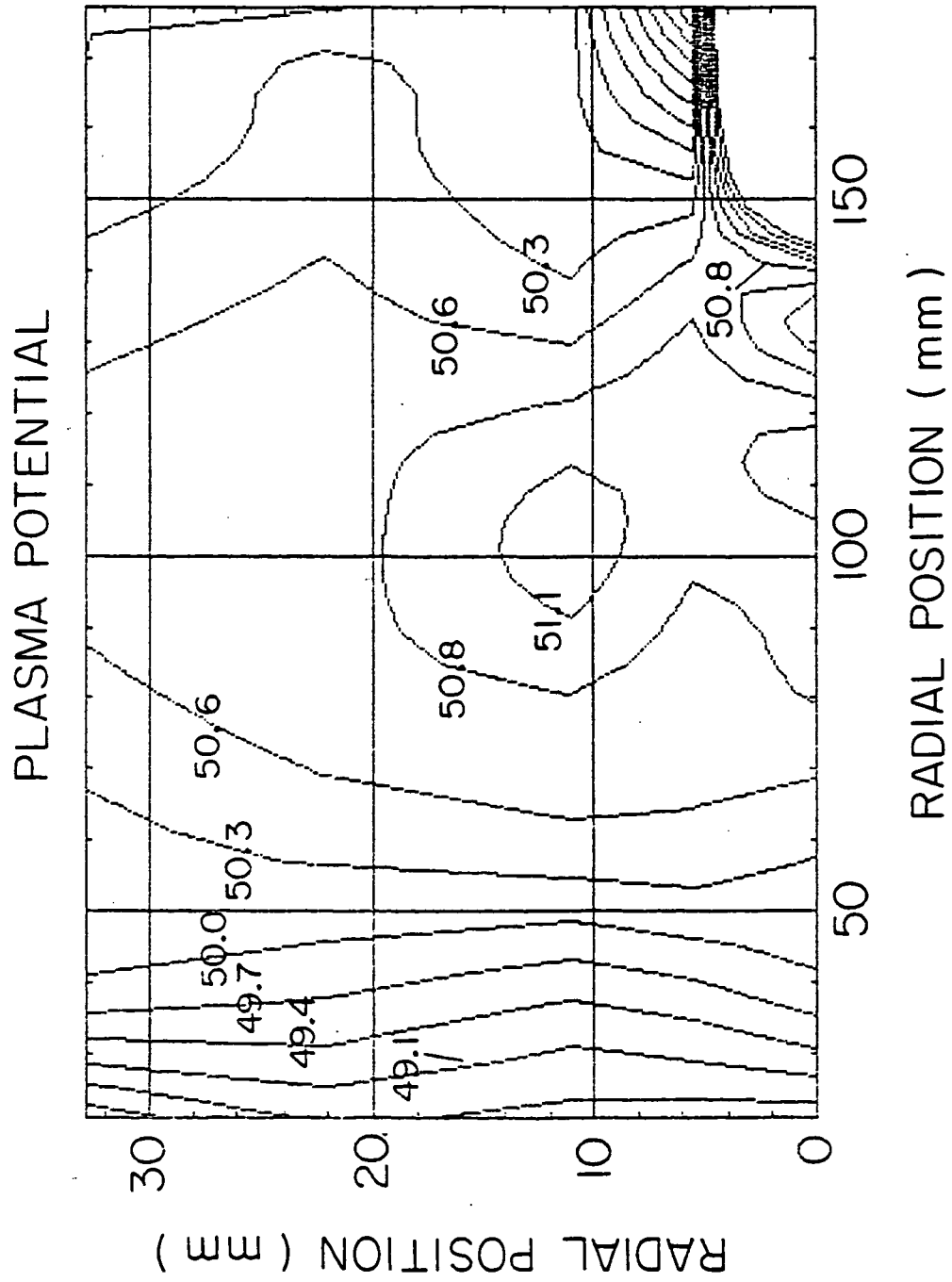


Figure 30. Contour map of plasma potential in volts for design 2.

A-684-801

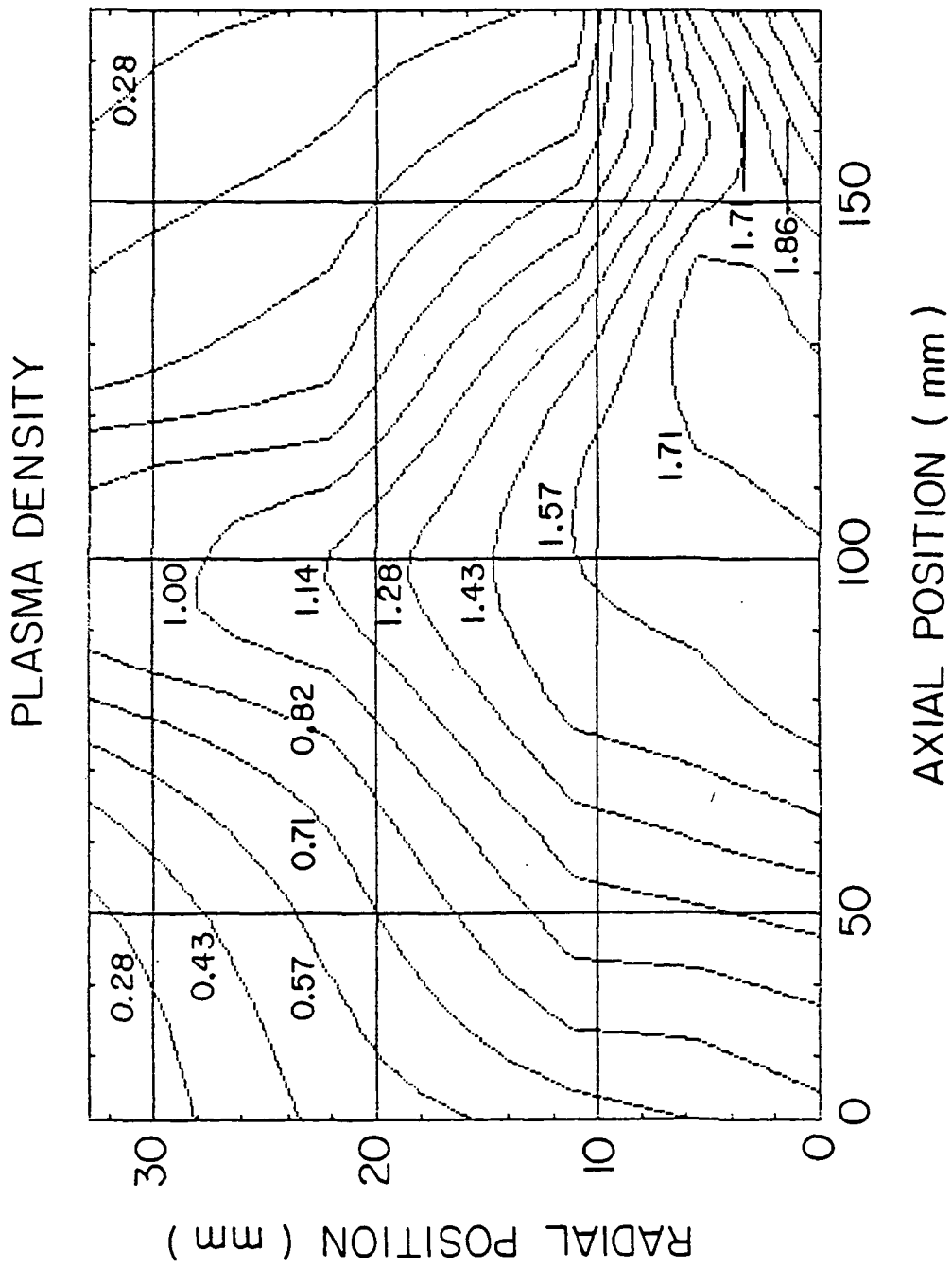


Figure 31. Contour map of plasma density in units of 10^{12} cm^{-3} for design 2.

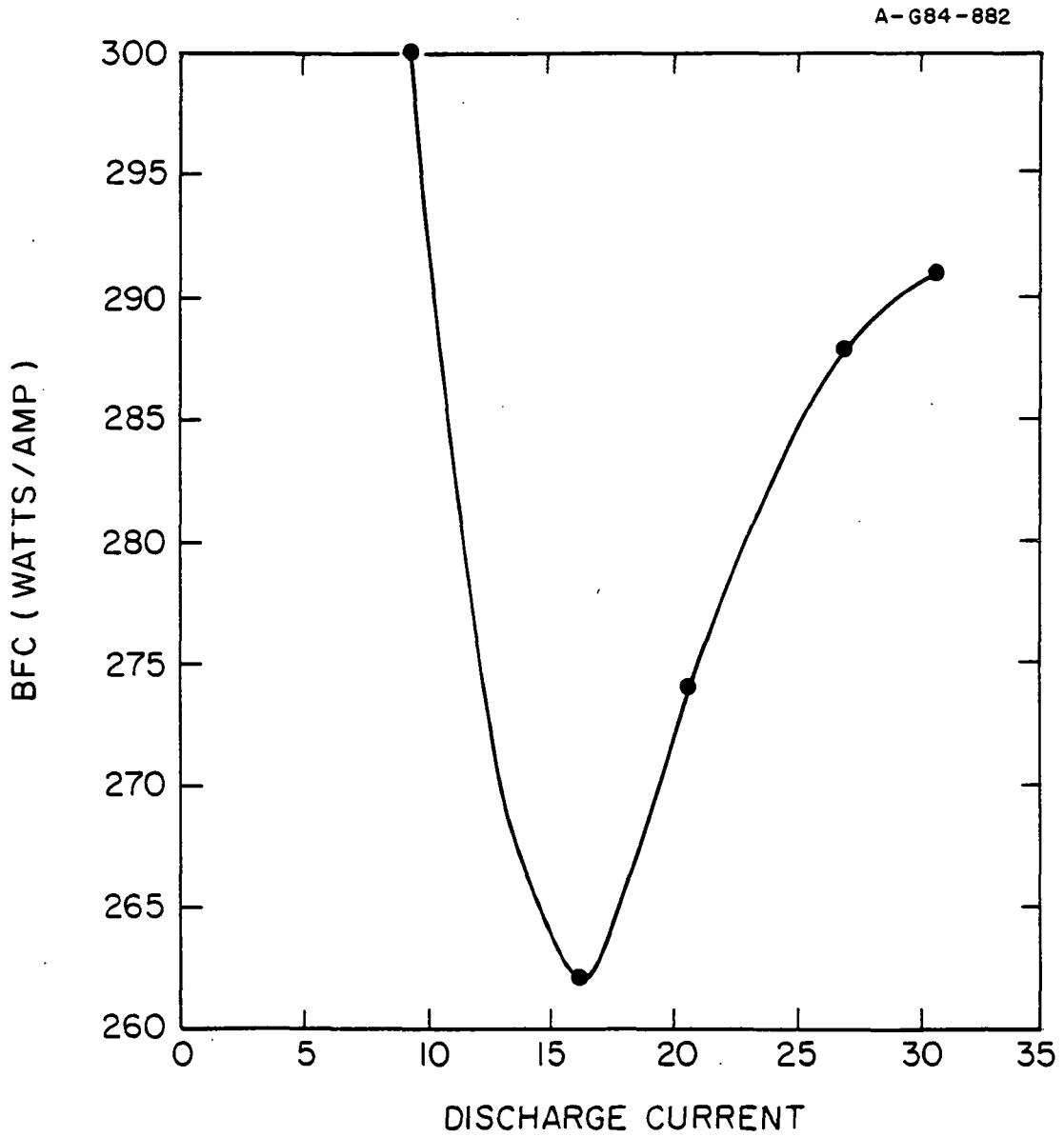


Figure 32. BCF curve for design 1.

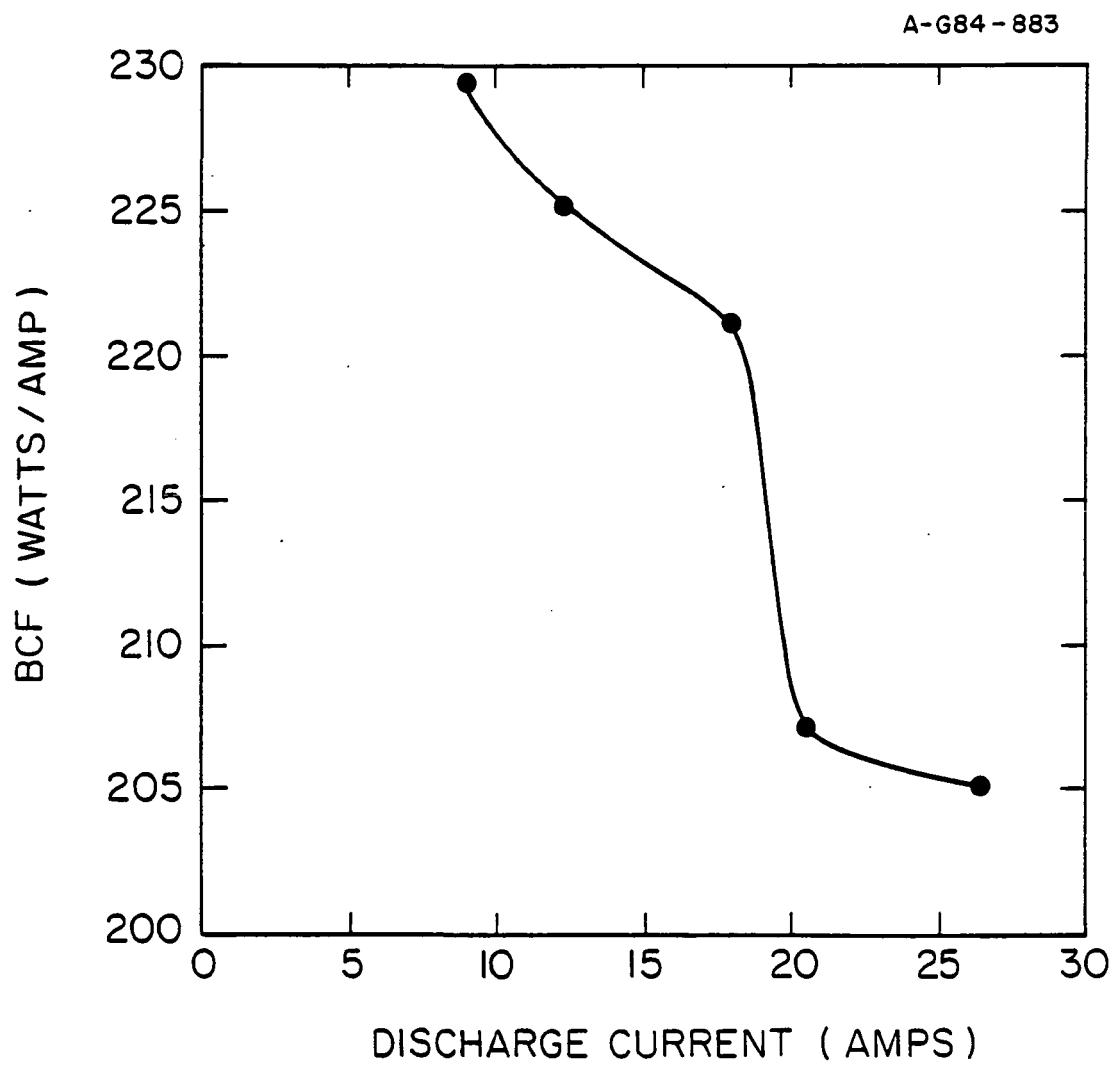


Figure 33. BCF curve for design 2.

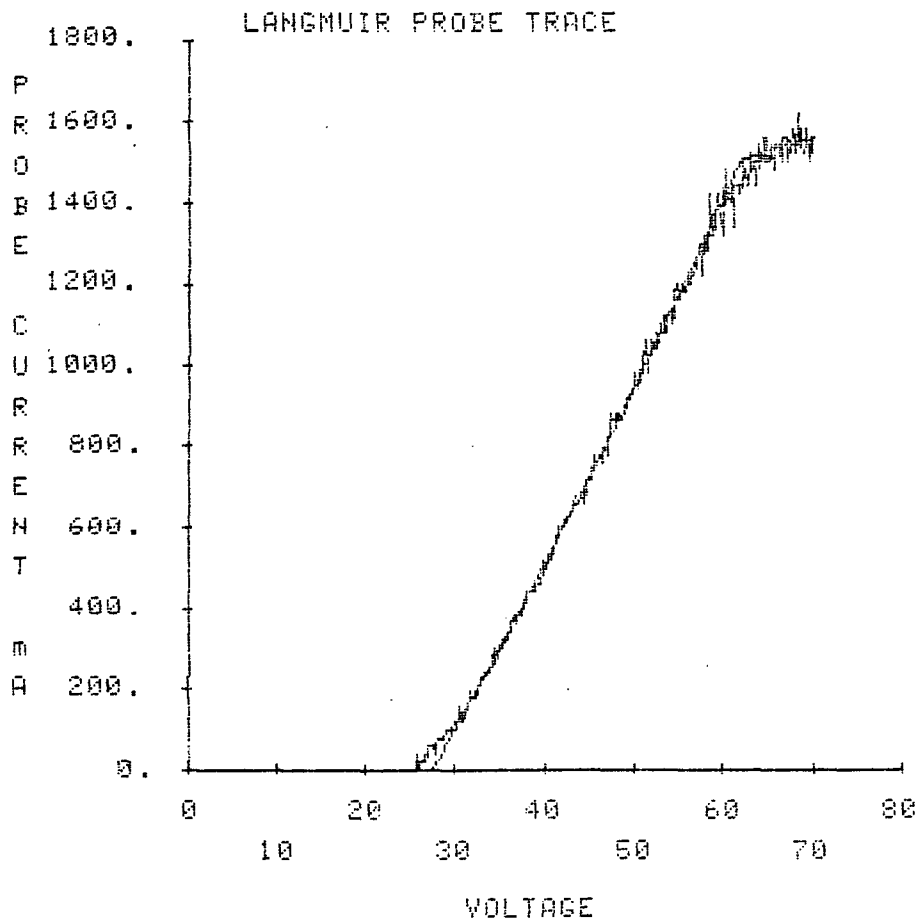


Figure 34. Langmuir trace ~ 1 cm from cathode orifice. Design 1.

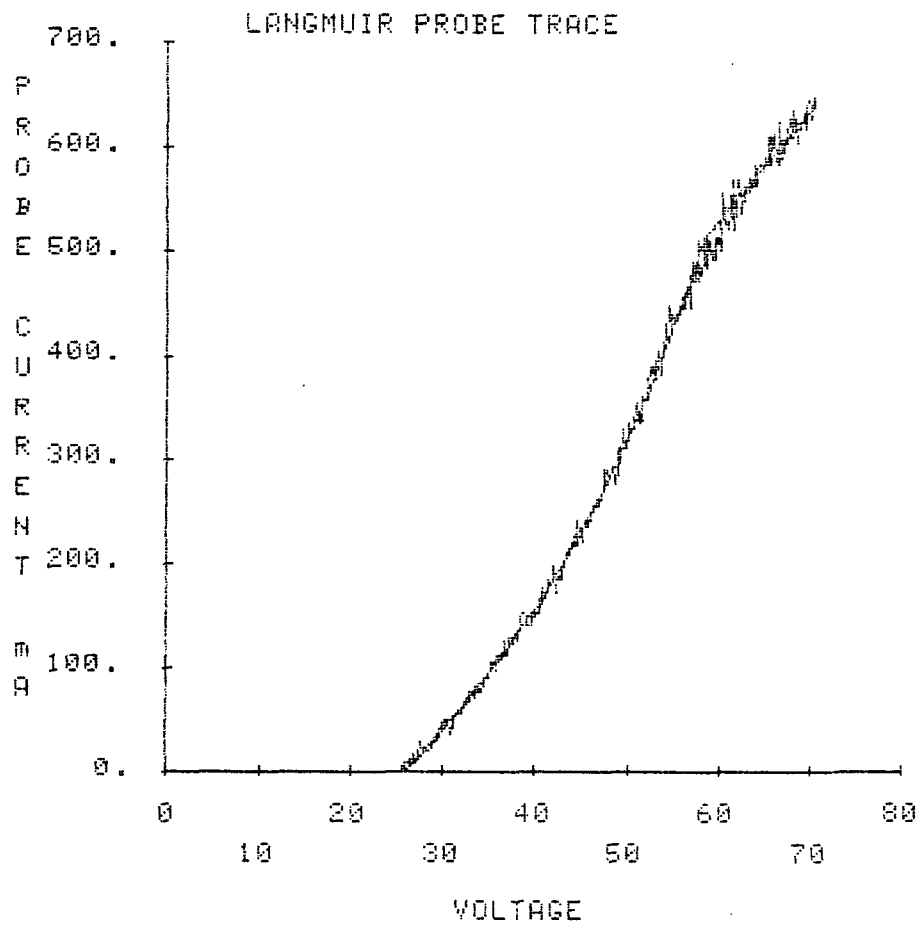


Figure 35. Langmuir trace ~ 2 cm from cathode orifice. Design 1.

ORIGINAL PAGE IS
OF POOR QUALITY

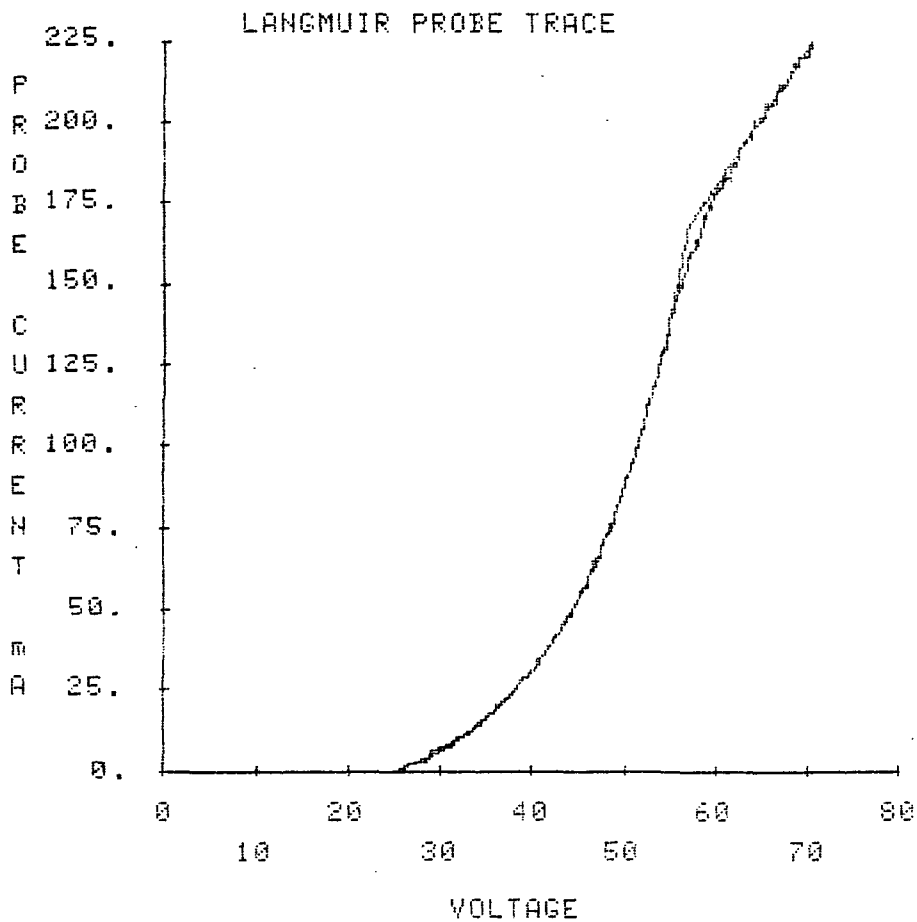


Figure 36. Langmuir trace ~ 4 cm from cathode orifice. Design 1.

ORIGINAL PAGE IS
OF POOR QUALITY

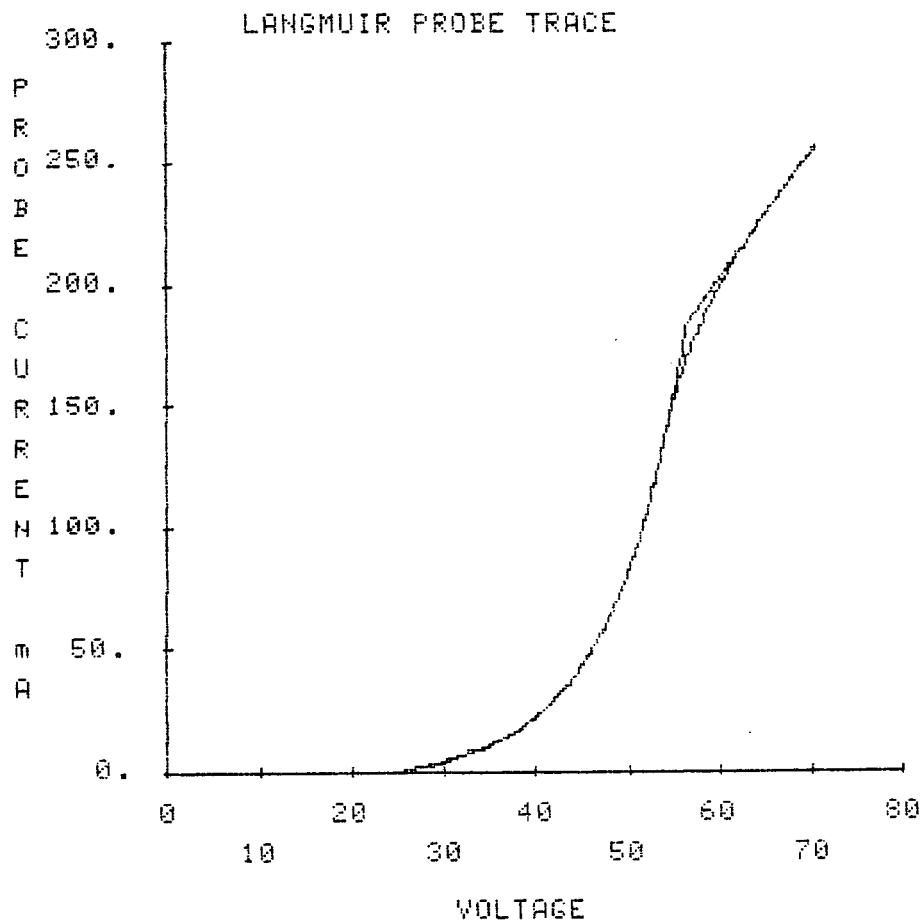


Figure 37. Langmuir trace ~ 6 cm from cathode orifice. Design 1.

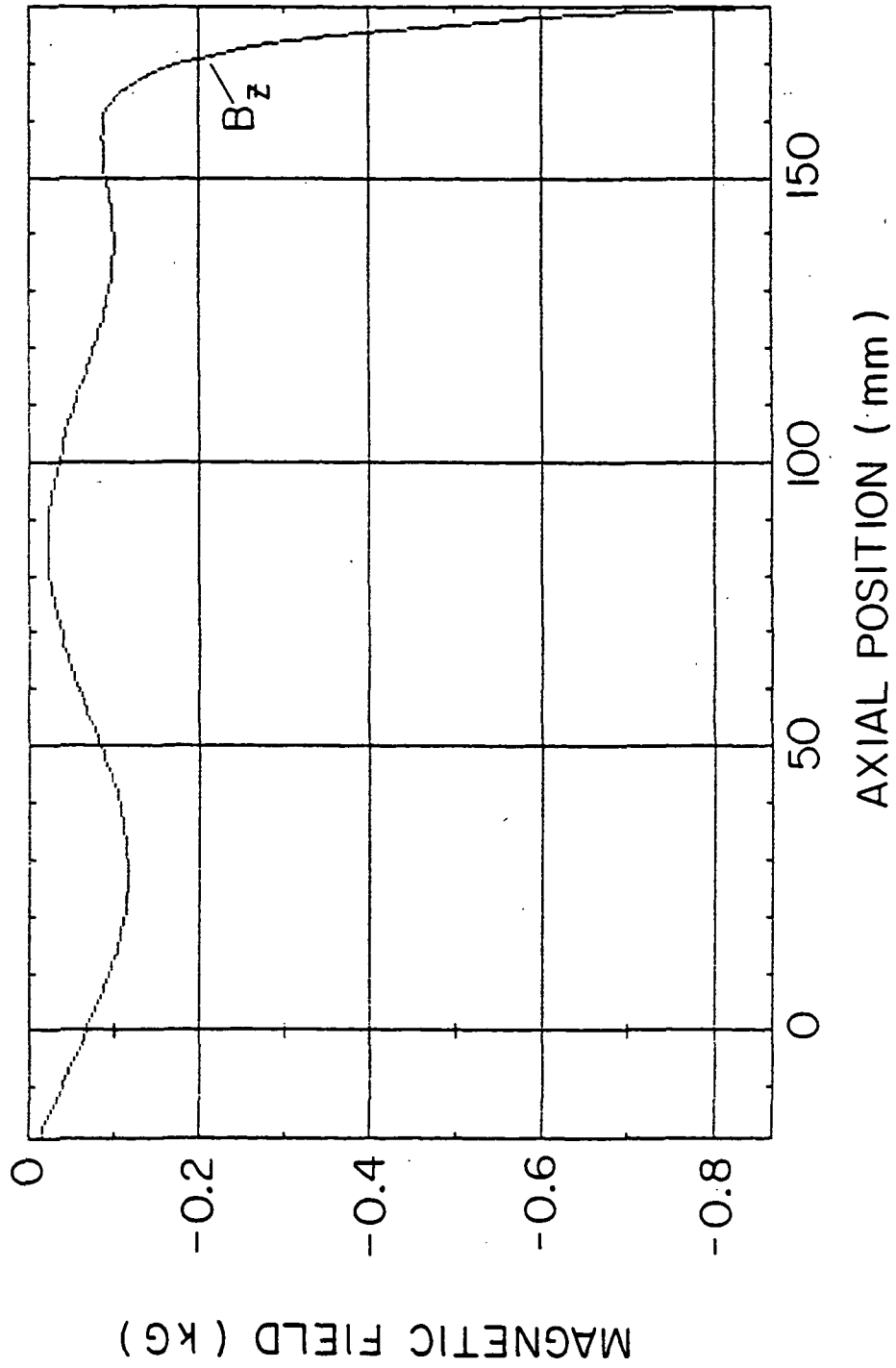


Figure 38. Axial component of magnetic field along the device axis in ring cusp design 2.

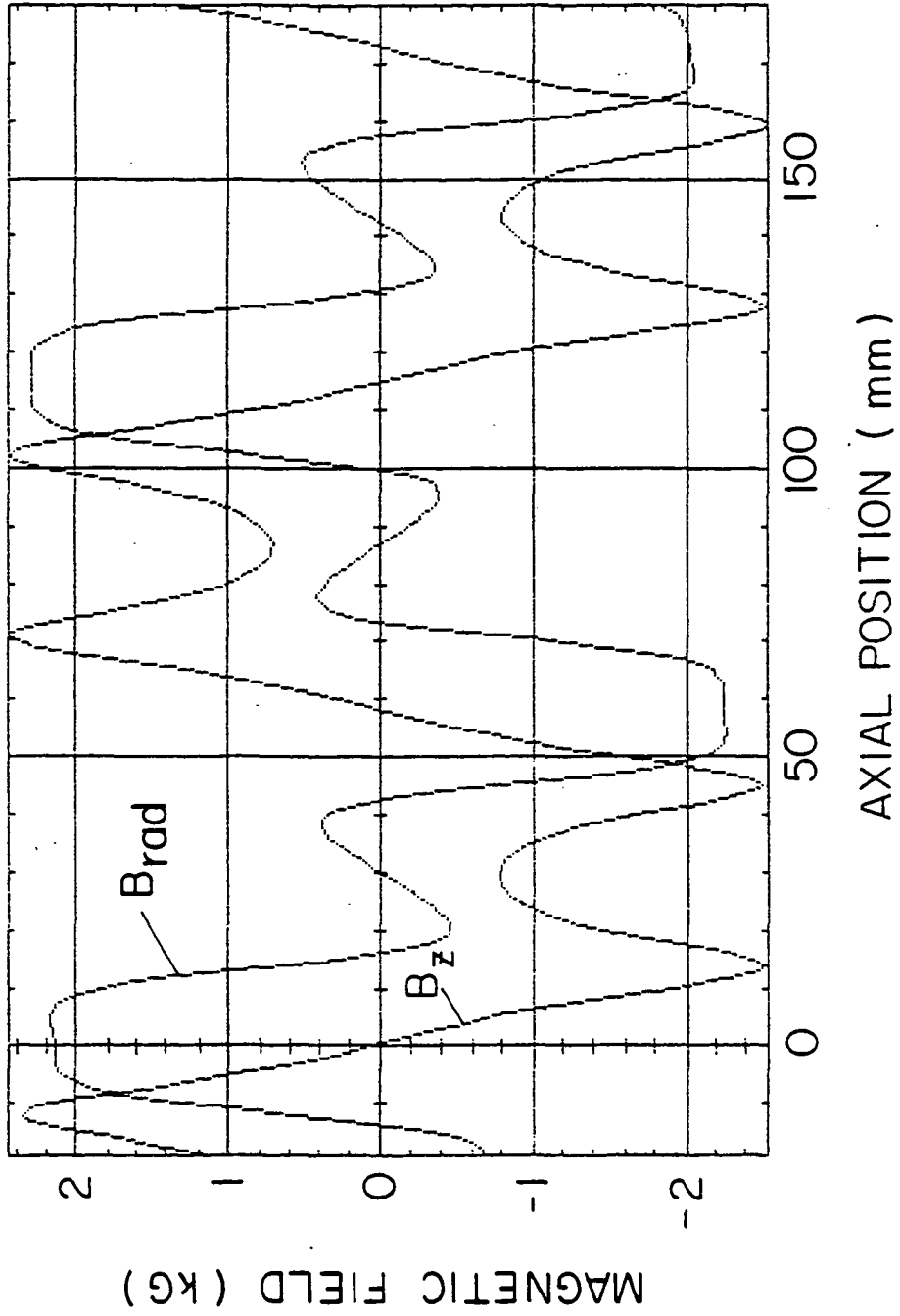


Figure 39. Magnetic field components along the poles faces in ring cusp design 2.

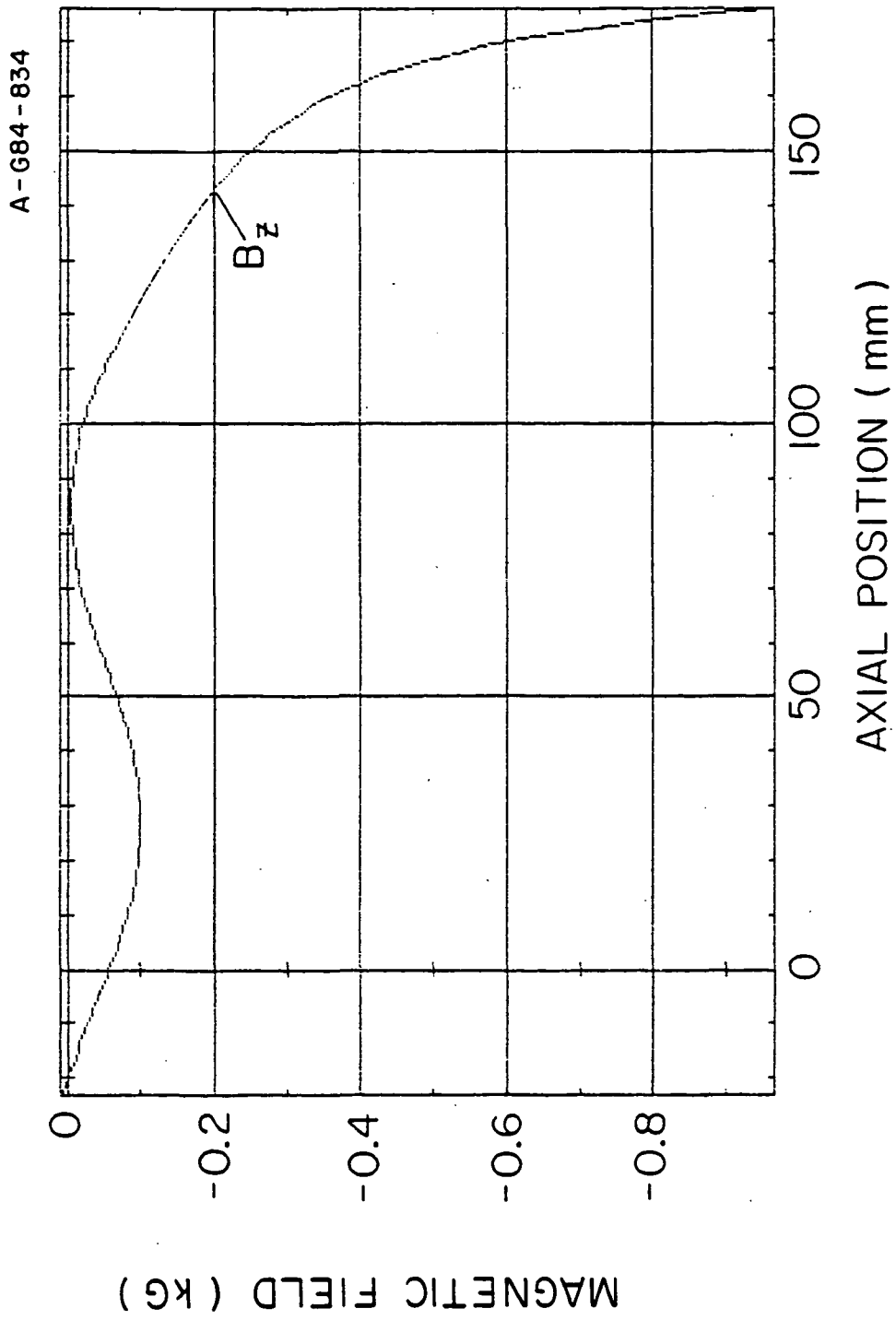


Figure 40. Axial component of magnetic field along the device axis in ring cusp design 1.

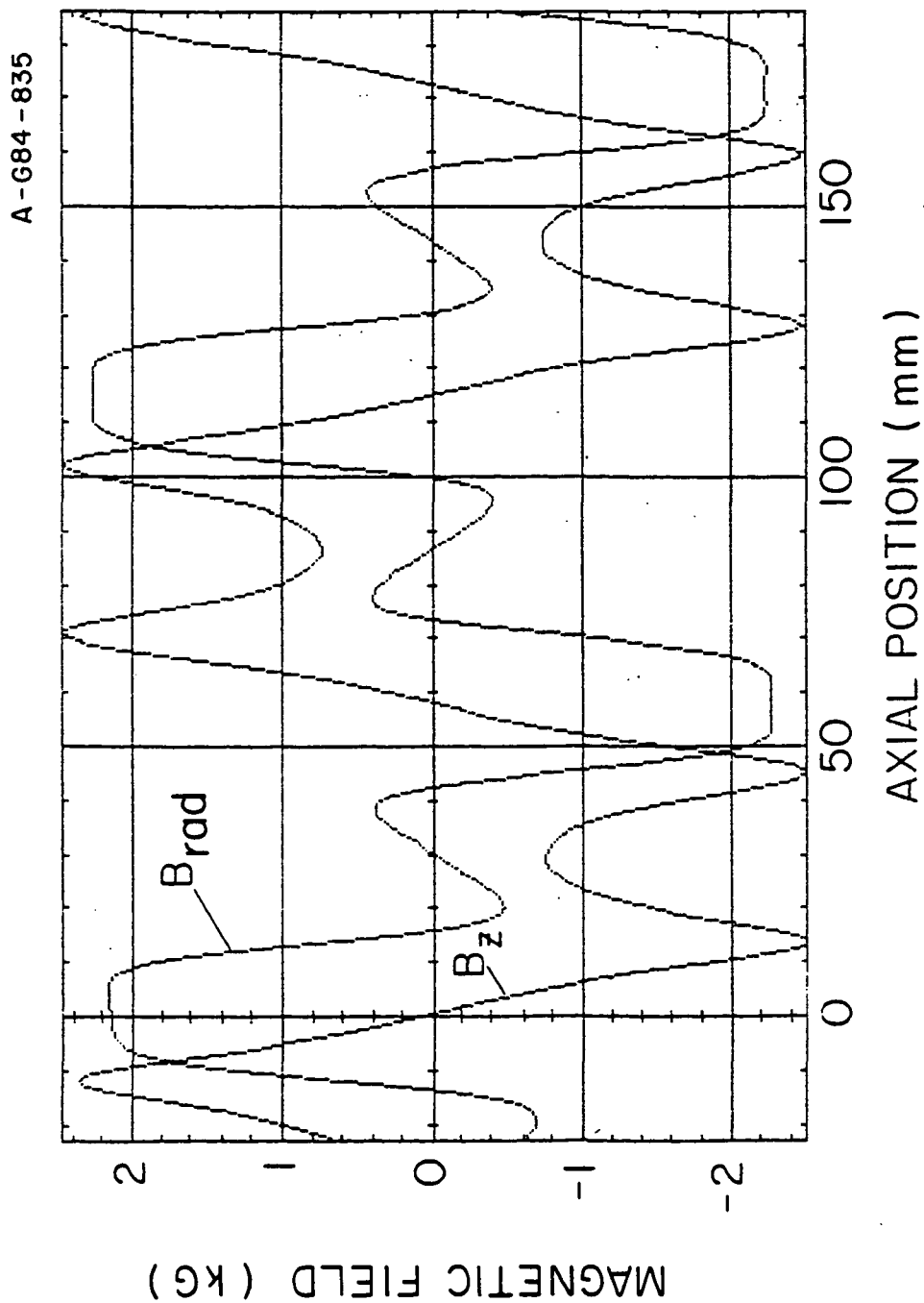


Figure 41. Magnetic field components across the pole faces in design 1.

ORIGINAL PAGE IS
OF POOR QUALITY

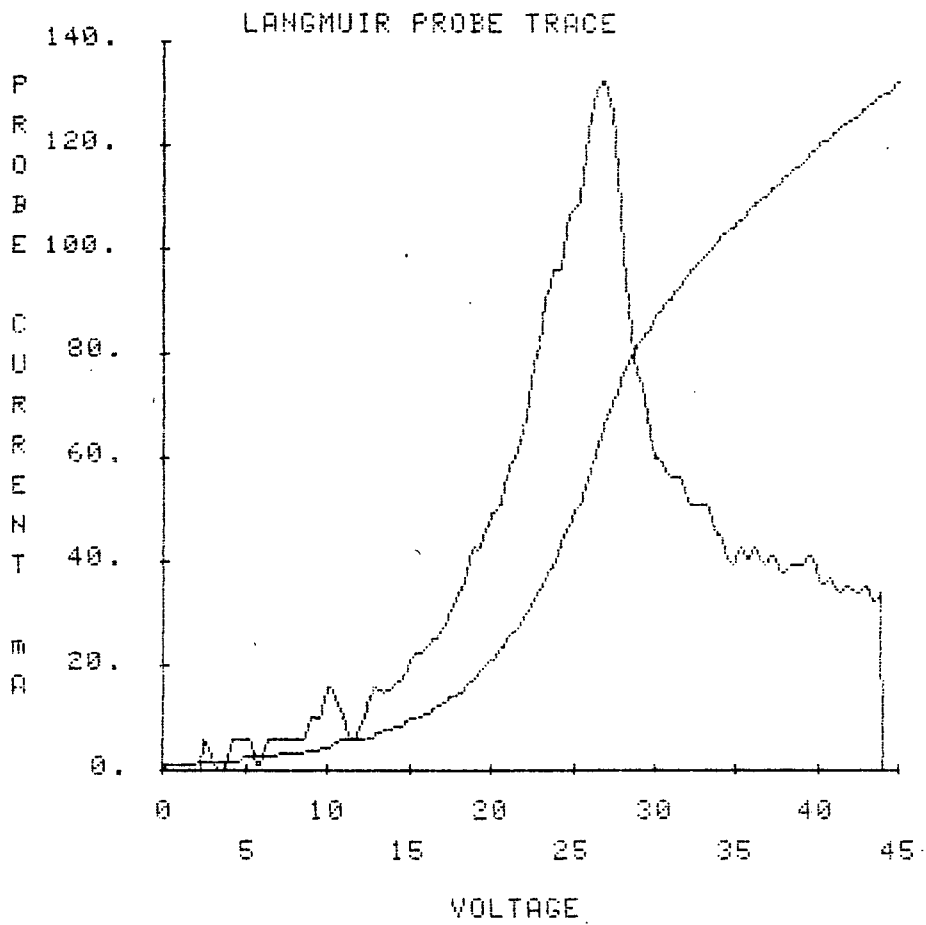


Figure 42. Langmuir trace and its derivative.

ORIGINAL PAGE IS
OF POOR QUALITY

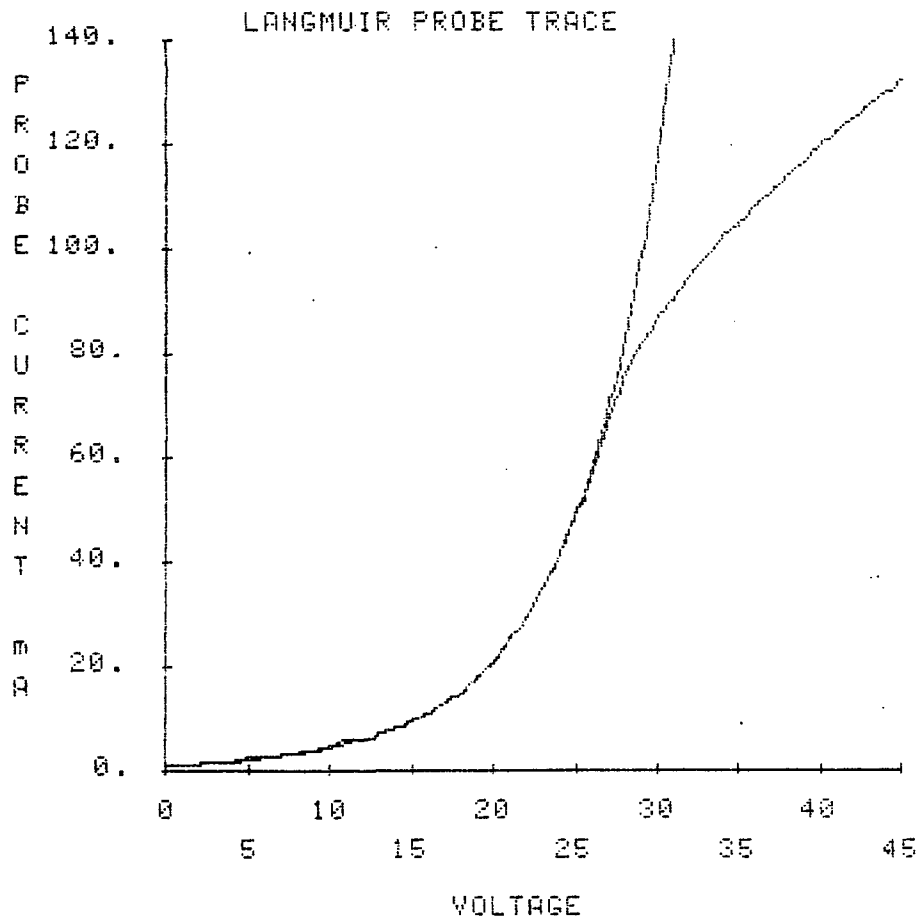


Figure 43. Curve fit below the plasma potential.

ORIGINAL PAGE IS
OF POOR QUALITY

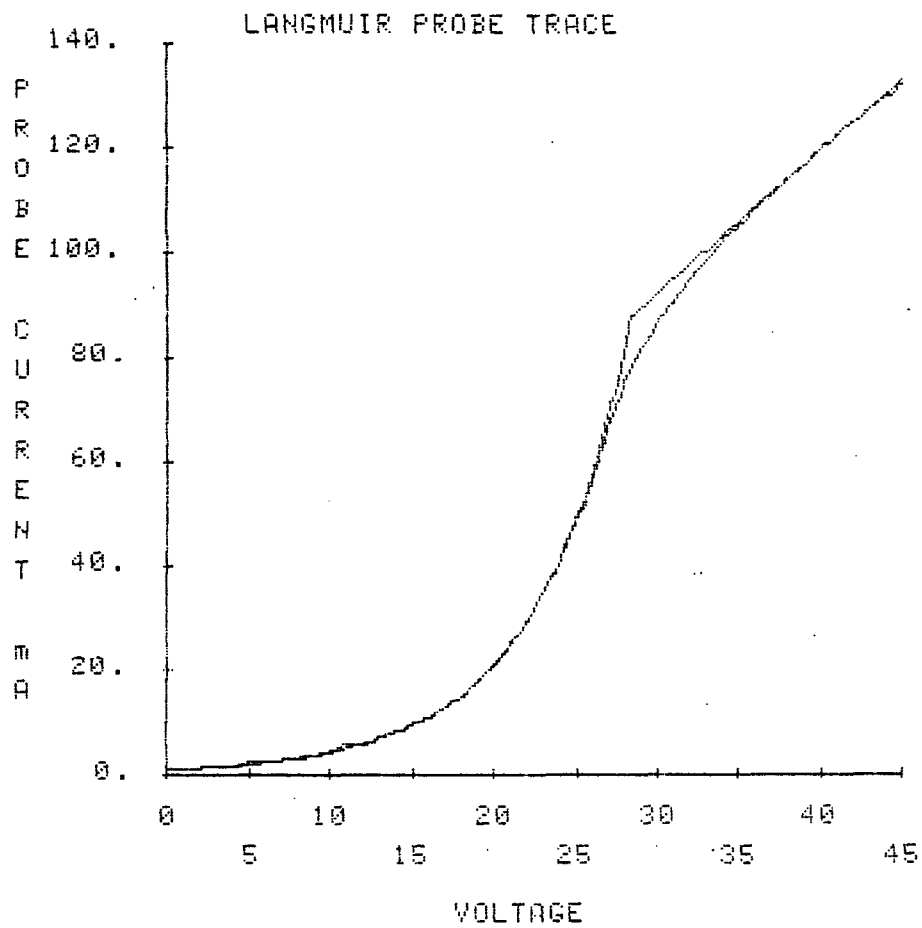


Figure 44. Curve fit above the plasma potential.